Extreme wind speed ramps - probabilistic characterization for turbine loads

Hannesdóttir, Ásta

Publication date:
2018

Document Version
Publisher's PDF, also known as Version of record

Extreme Wind Speed Ramps – Probabilistic Characterization for Turbine Loads

Department of Wind Energy PhD Report 2018

Ásta Hannesdóttir

DTU Wind Energy PhD-0087 (EN)
DOI number: 10.11581/dtu:00000043

November 2018

DTU Wind Energy
Department of Wind Energy

DTU Wind Energy
Department of Wind Energy

Ph.D. Thesis

Extreme wind speed ramps -

probabilistic characterization for turbine loads

Ásta Hannesdóttir

Risø campus, Roskilde, 2018

DTU

Technical University of Denmark
DTU Wind Energy
Department of Wind Energy

DTU Risø Campus
Frederiksborgvej 399 Building 125
4000 Roskilde, Denmark
Phone +45 12345678
RogerFederer@dtu.dk
www.vindenergi.dtu.dk

Thesis title:
Extreme wind speed ramps -
probabilistic characterization for turbine loads

PhD student:
Ásta Hannesdóttir
Department of Wind Energy
Technical University of Denmark
Frederiksborgvej 399, 4000 Roskilde, Denmark
astah@dtu.dk

Supervisors:
Mark Kelly
Department of Wind Energy
Technical University of Denmark
Frederiksborgvej 399, 4000 Roskilde, Denmark
mkel@dtu.dk

Jakob Mann
Department of Wind Energy
Technical University of Denmark
Frederiksborgvej 399, 4000 Roskilde, Denmark
jmsq@dtu.dk

Anand Natarajan
Department of Wind Energy
Technical University of Denmark
Frederiksborgvej 399, 4000 Roskilde, Denmark
anat@dtu.dk

Summary

The work presented in this thesis contains characterization of wind speed fluctuations of different scales. From small scale turbulence to large coherent fluctuations beyond turbulence. It is investigated how these fluctuations are relevant for wind turbines and in particular wind turbine design.

A rotational shaping filter is derived from a model describing the power spectrum of turbulent fluctuations observed from a rotating frame of reference. The rotational shaping filter is applied to wind speed measurements in frequency domain to see how rotational sampling influences gust statistics. The number of extreme gusts is roughly doubled, the gust duration is significantly reduced and amplitudes of gusts with duration below 5 s are amplified by the effect of rotational sampling.

The wind turbine safety standard of the International Electrotechnical Commission (IEC 61400-1 edition 3) specifies extreme external wind conditions, including an extreme turbulence model (ETM). The ETM is used here to select extreme events where the variance exceeds the ETM level. It is shown that the high variance of these events is not caused by extreme turbulence, but rather by ramp-like increases in wind speed. The events are simulated with constrained turbulence simulations that are further used for wind turbine response simulations with the aeroelastic software HAWC2. The loads from the event simulations are compared with the extreme turbulence load case and are on average lower for all considered load components.

A new method to characterize ramp-like wind speed fluctuations is presented. This method combines the continuous wavelet transform and the fitting of an idealized ramp function, which provides estimates of ramp amplitude and rise time. These, together with the corresponding direction change are used to statistically characterize ramp-like fluctuations at three different measurements sites. The estimated variables are compared to the extreme coherent gust with direction change (ECD) from the IEC standard where it is found that the observed rise time is generally longer, on average around 200 s.

These observations are used to define a coherent gust model with direction change. The gust model provides the joint description of the rise time, amplitude and directional changes with a 50-year return period. Within the framework of the coherent gust model, the return period of the ECD is found to be approximately 15,000 years. The coherent gust model is used to investigate the load implications of selected variables which are simulated in HAWC2. The load simulations are performed with and without a yaw controller and compared with the design load case of the ECD. The comparison shows that the differences between the investigated extreme loads of the ECD and the modeled gusts are 11% or less. The only exception is for the tower top yawing moment where maximum load for the modeled gust is 22% lower than the IEC gust.

Résumé

Denne afhandling indeholder en karakterisering af fluktuationer i vindhastighed på forskellige skalaer. Fra småskala turbulens til store kohærente fluktuationer. Det undersøges, hvordan disse fluktuationer er relevante for vindmøller og vindmølledesign.

Et filter udledes fra en model, der beskriver spektret for turbulente fluktuationer i et roterende referencesystem. Filteret anvendes til vindhastighedsmålinger i frekvensdomænet for at undersøge om det at måle i et roterende koordinatsystem vil påvirke statistikken af vindstød. Resultatet er, at antallet af ekstreme vindstød fordobles, varigheden reduceres markant, og amplituden af vindstød med varighed under 5 s forstærkes af effekten af at måle i et roterende koordinatsystem.

Den Internationale Elektrotekniske Kommissions vindmølle sikkerhedsstandard (IEC 61400-1 udgave 3) angiver ekstreme vindforhold, herunder en ekstrem turbulensmodel (ETM). ETM'en bruges her til at vælge ekstreme begivenheder, hvor variansen overstiger ETM-niveauet. Det påvises at den høje varians af disse hændelser ikke skyldes ekstrem turbulens, men snarere pludselige stigninger i vindhastigheden. Begivenhederne simuleres med tilpassede turbulenssimuleringer, som derefter anvendes til simulering af vindmøllelaster med den aeroelastiske software HAWC2. Lasterne fra simuleringerne sammenlignes med lasterne fra ekstrem turbulensmodellen, og er lavere for de betragtede lastkomponenter.

En ny metode til at karakterisere pludselige stigninger i vindhastigheden præsenteres. Denne metode kombinerer wavelet-transformationen med tilpasningen af en idealiseret rampefunktion, som giver estimater for amplituden og stigningstid. Sammen med den tilhørende vindretningsændring bruges disse til statistisk at beskrive kohærente vindstød ved tre forskellige målestationer. De estimerede variable sammenlignes med den ekstreme vindstødsmodel (ECD) fra IEC-standarden. Her konstateres det, at den observerede stigningstid generelt er længere for de observerede vindstød, i gennemsnit ca. 200 s.

Disse observationer bruges til at definere en kohærent vindstødsmodel med retningsændring. Modellen giver en samlet beskrivelse af stigningstid, amplitude og retningsændringer med en 50-årig returperiode. Inden for rammerne af den kohærente vindstødsmodel er returperioden for ECD beregnet til ca. 15.000 år. Den kohærente vindstødsmodel bruges til at undersøge konsekvenserne for lasterne af udvalgte variable, der simuleres i HAWC2. Belastningssimuleringerne udføres med og uden en yaw-controller og sammenlignes med ECD'ens design-laster. Sammenligningen viser, at forskellene generelt er små mellem de undersøgte ekstreme belastninger af ECD og de modellerede vindstød, typisk 11% eller mindre. Den eneste undtagelse er mølletårnets yaw moment, hvor maksimal belastningen for de modellerede vindstød er 22% lavere end dem forårsaget af de kohærente vindstød fra IEC.

Acknowledgements

I would like to show my gratitude to all the people who in different ways have helped and supported me during this PhD project.

First of all I would like to thank my supervisors Anand Natarajan, Jakob Mann and Mark Kelly. Anand, thank you for guiding the project in a practically oriented direction, and towards wind turbine technology early in the process. Thank you Jakob, for your patience and calming effect on a PhD student, and your important scientific advice. Mark thank you for always seeing the potential in my findings. Our collaboration has never been boring. I have learned so much from you not only in wind energy but also well outside the field, and have enjoyed our many conversations during this period.

Thanks to all my section colleagues and section leader Jake Badger.

I would like to thank my Phd office mates through the period: Julia Lange, Jianting Du, Bjarke Tobias Olsen and Marc Imberger. Thank you for your company and friendship.

Thanks to my awesome colleagues from LAC: Albert Urbán and David Verelst. I hope to continue our collaboration well into the future.

A special thanks to my family, my husband Andreas for all the endless love and positive support. Thank you to our children for being the sweetest kids in the world. And to my extended family in Denmark and family in Iceland, especially my parents that came to Denmark to show support during the last couple of months of my PhD study.

Risø campus, Roskilde, November 2, 2018

Ásta Hannesdóttir

Contents

CHAPTER 1

Introduction

Over the last decade, wind energy has gone through impressive development. The global annual wind energy capacity has grown from 115 GW in 2008 to 514 GW in 2017 (IRENA, 2018), which corresponds to an increase from 11% to 24% of the total annual renewable energy capacity during those years. This increased capacity is mainly due to improved wind turbine technology, allowing for taller turbines with access to higher wind speeds and larger rotors leading to increased energy yield. These improvements lead to greater capacity factors[1] for most wind resource sites.

Following the advancements in wind turbine design and increased global wind energy capacity, the levelized cost of energy (LCoE)[2] has decreased through the years. In the period from 2010 to 2017 the LCoE for onshore wind projects was reduced by 22% and for offshore wind projects the reduction is 13% (IRENA, 2017).

1.1 Wind turbine design

The aforementioned improvements, give rise to new challenges as cost and structural safety naturally still must be considered when designing a wind turbine. Larger wind turbines components demand new designs, that cannot just be scaled up from previous generations without technical improvements (Sieros et al., 2012). Wind turbines are made with a design lifetime typically specified as 20 years (Hansen, 2008). They should therefore be robust to survive the specified design lifetime, but at the same time not overly robust leading to unnecessary expenses. The challenge in wind turbine design (as with many other designs) is to reach a balance between cost and structural safety, by minimizing the cost of components and optimizing functionality while maintaining reliability and safety.

1.2 The IEC wind turbine safety standard

Wind turbine safety standards exist to ensure the design quality of wind turbines. The current main developer of wind turbine safety standards is the International Electrotechnical Commission (IEC) that since 2001 has taken the place of various national standards. The IEC (61400-1 edition 3, 2005) specifies design requirements which offer an expected reliability level for a wind turbine. It applies to all wind turbines, but is particularly relevant for large onshore wind turbines (Manwell et al., 2009).
In addition to normal operation conditions, the standard prescribes a number of extreme

[1] Capacity factor: the average power divided by rated power.
[2] LCoE: The sum of cost over lifetime divided by the sum of energy produced over life time.

external wind conditions that a wind turbine must be able to withstand during its design lifetime. These extreme conditions are described in a set of models used in different design load cases (DLC's) that are used to predict ultimate loading on wind turbines. The extreme events of the models are defined to have a return period of 50 years.
Standard wind turbine classes are defined in terms of wind conditions at a given site, divided into three extreme wind speed classes and three turbulence classes. Most of the DLC's take into consideration the wind speed class and/or the turbulence class and are further scaled with the rotor diameter of the considered wind turbine.

When following the IEC standard during the wind turbine design process, it is important that the different extreme models are realistic, reflecting the expected wind conditions and extreme events at the considered wind turbine site. However, one has to keep in mind that the standard wind turbine classes are made to cover most applications and represent many different sites. The classes do not describe external conditions at any specific site. Therefore the IEC standard offers an option of choosing site-specific values for the extreme models.

1.3 The extreme turbulence model

The IEC standard prescribes an extreme turbulence model (ETM), with the 10-minute standard deviation with a 50-year return period as function of 10-minute mean wind speed at hub height. The model is scaled with the annual average wind speed and the reference turbulence intensity. The DLC including the ETM is used for ultimate load predictions and is considered an important design driving load case, especially for the tower and blades (Bak et al., 2013).

The ETM is used to simulate wind turbine response to extreme stochastic fluctuations of atmospheric flow. Therefore the model is used in conjunction with a three-dimensional turbulence spectral model. The standard specifies two such models: the Mann uniform shear turbulence model (Mann, 1994) and the Kaimal spectral model (Kaimal et al., 1972) with an additional exponential coherence model.

A number of studies have investigated the ETM and the corresponding wind turbine response. E.g. in Fitzwater et al. (2003) and in Abdallah et al. (2016) the estimated turbulence levels with a 50-year return period are based directly on the IEC joint distributions of 10-minute mean wind speed and 10-minute standard deviation. In a similar way Saranyasoontorn and Manuel (2006) investigate wind turbine response to turbulence levels, though here with a 20-year return period.

In Sang Moon et al. (2014) and in Dimitrov et al. (2017), the 50-year return period of turbulence levels is estimated from measurements. In both studies the estimated levels exceed the ETM indicating that the ETM is non-conservative. This was also found in Hannesdóttir et al. (2018), where the estimated turbulence levels with a 50-year return period exceed the ETM for raw measurements and linearly detrended measurements, although not for high-pass filtered measurements.

1.4 The uniform gust models

The IEC standard contains various gust models that represent different kinds of extreme events. These DLC models are: Extreme operating gust (EOG), extreme direction change (EDC), extreme coherent gust with direction change (ECD) and extreme wind shear (EWS). These design load cases are all modeled with a time varying waveform that is uniform across the whole rotor (except the EWS that is uniform in the lateral direction only).

A wind gust may be defined in many different ways and the definition used often depends on the context. In wind energy related studies gusts are often defined in terms of a gust factor (or peak factor), where the wind velocity fluctuations are assumed stationary and normally distributed (e.g Cartwright and Longuet-Higgins, 1956; Frandsen et al., 2008). During the past fifteen years, a few studies have addressed the limited spatial extent of gusts within a stochastic framework, i.e. gusts in a stationary, homogeneous turbulent flow (Larsen et al., 2003; Bierbooms, 2005; Bos et al., 2014). This is a valid consideration, as we have seen an increase in size of wind turbine rotors during this period, and these stochastic fluctuations are not coherent across the rotor of a multi-megawatt wind turbine. In the previous mentioned studies, gust models with a limited spatial extent are defined as a potential replacement of the uniform EOG model of the IEC.

In the current work, the challenge of a realistic gust description for larger wind turbines is turned around. Instead of characterizing the spatial extent of an extreme gust as homogeneous stationary turbulent flow, we consider larger scales beyond turbulence. Here we find rare reoccurring events, where wind speed fluctuations are coherent ramp-like increases in wind speed, and the assumption of stationarity and homogeneity is no longer valid. Here the challenge is to recognize and characterize these large coherent gusts and compare them to the standard models.

There are many studies within the field of atmospheric science that investigate large coherent structures in turbulent flow (e.g. Mahrt, 1991; Belušić and Mahrt, 2012; Barthlott et al., 2007; Fesquet et al., 2009). The coherent structures may originate from a broad range of different meteorological weather phenomena and may be observed under different stability conditions.

- In a convective boundary layer coherent structures may be generated by surface buoyancy fluxes, latent heat release or cloud radiative effects, where they are observed as convective cells and rolls (Drobinski et al., 1998; Young et al., 2002).
- In a neutral boundary layer, coherent structures may be seen as shear driven streaks as shown by Foster et al. (2006) with large-eddy simulations.
- In a stable boundary layer, micro-fronts may be generated by e.g. gravity waves, Kelvin-Helmholtz instabilities, surface heterogeneity or pressure disturbances (Mahrt, 2010).

These coherent structures are seen in 10-minute wind statistics as high variance events and in high frequency measurements as ramp-like increase in wind speed often with a corresponding direction change. Therefore comparison of these events is made with the

ETM (Hannesdóttir et al., 2018) and the ECD (Hannesdóttir and Kelly, 2018).

1.4.1 Thesis outline

In this thesis we look at measurements of gusts, turbulence and large coherent fluctuations and address the following questions:

- How relevant are the observed fluctuations for wind turbines?
- Which design load cases are the most relevant for practical load considerations and design?

The following work is based on submitted papers, a paper draft and a single study where the main findings are written in a chapter. The thesis is organized as follows:

Chapter 2: Contains a study on the effect of rotational sampling and filtering on gust statistics. A rotational shaping filter is derived and applied to wind speed measurements in frequency domain.

Chapter 3: Includes a study on extreme wind speed fluctuations. The extreme fluctuations are observed as high variance events where the 10-minute standard deviation exceeds the ETM. The high variance events are simulated with a constrained turbulence simulation which are used for wind turbine load simulations. Relevant wind turbine component loads are compared with the ETM load case.

Chapter 4: Presents a method to detect and characterize large scale fluctuations that are observed as extreme wind speed ramps, or coherent gusts in measurements. The detected wind speed ramps are characterized and the estimated variables of rise time, amplitude and direction change are compared with the ECD design load case.

Chapter 5: In this study, a subset of the observed coherent gusts described in Chapter 4 is used for wind turbine load simulations. The observed gust parameters are modeled with the Nataf distribution model to obtain a three dimensional environmental surface with a 50-year return period. From the surface a few potentially critical points are selected for wind turbine load simulations.

Chapter 6: Summarizes the thesis in a conclusion and provides an outlook on how to further investigate atmospheric fluctuations relevant for wind turbine loads.

CHAPTER 2
Gusts in a rotating frame of reference

2.1 Introduction

Turbulent wind speed fluctuations encountered in a rotating frame of reference are different from those observed in a fixed reference frame. Certain periods of the rotationally sampled turbulence are seen to be more compressed in time, when compared with fixed-point turbulence. The spectrum of rotationally sampled wind speed fluctuations is distorted in certain frequency sub ranges. This distortion results in narrow areas of high turbulence energies in the frequency ranges corresponding to multiples of the rotational frequency of the reference frame.

The objective of this analysis is to find out how rotational sampling influences gust statistics. This will be achieved by defining a rotational shaping filter that can be applied to wind speed measurements in frequency domain. The shaping filter is derived from a rotational spectral model (Kristensen and Frandsen, 1982; Connell, 1982). The wind speed measurements are filtered with a band-pass filter and additionally the rotational shaping filter. Gust statistics are performed on both data sets and compared.

2.2 The effect of rotational sampling on wind speed fluctuations

Kristensen and Frandsen (1982) and Connell (1982) independently derived a model that describes the power spectrum of turbulent fluctuations observed from a rotating frame of reference. A detailed derivation of the model may be found in their papers and a comparison with spectra of rotationally sampled measurements. The spectral model is in good agreement with experimental findings.

The model is based on earlier work by Rosenbrock (1955) that derives the spacial autocovariance function of isotropic turbulent flow observed from a point on a wind turbine blade rotating at a constant speed. Kristensen and Frandsen (and Connell) included the von Kármán energy spectrum (Kárṁan, 1948) in Rosenbrock's spacial autocovariance function. The autocovariance is expressed as a function of $r = |\mathbf{r}|$, which is the separation distance between a point on the rotating wind turbine blade and a point in the flow lagged in time. The magnitude of $\mathbf{r}$ is given by

$$r = \sqrt{(-U\tau)^2 + [2a\sin(\omega_0\tau/2)]^2} \tag{2.1}$$

where τ is the time lag and U is the mean wind speed of the flow perpendicular to the rotation of radius a and angular velocity ω_0. If we only consider fluctuations in the direction of the mean wind speed u, the two point covariance may be defined as

$$R_{11} = R_L(r)\frac{U^2\tau^2}{r^2} + R_T(r)\left(1 - \frac{U^2\tau^2}{r^2}\right) \tag{2.2}$$

where R_L is the autcovariance function of the turbulence velocity components parallel to $\mathbf{r}$ and R_T is perpendicular to $\mathbf{r}$. The autocovariance functions R_L and R_T may be expressed using the isotropic von Kármán energy spectrum:

$$R_L = \frac{2\sigma^2}{\Gamma(1/3)}\left(\frac{r}{2L}\right)^{1/3} K_{1/3}\left(\frac{r}{L}\right) \tag{2.3}$$

and

$$R_T = \frac{2\sigma^2}{\Gamma(1/3)}\left(\frac{r}{2L}\right)^{1/3}\left[K_{1/3}\left(\frac{r}{L}\right) - \frac{r}{2L}K_{2/3}\left(\frac{r}{L}\right)\right] \tag{2.4}$$

where σ^2 is the variance of u-component wind speed, Γ is the gamma function, L is the integral length scale of the the turbulent fluctuations, and K_m is the modified Bessel function of the second kind, of order m. By inserting equations 2.3 and 2.4 into equation 2.2 and normalizing with σ^2 we find the non-dimensional autocorrelation function:

$$\begin{aligned}\rho(s) = \frac{2}{\Gamma(1/3)}(\alpha^2\sin^2 s + \beta^2 s^2)^{1/6}\Big[&K_{1/3}(2(\alpha^2\sin^2 s + \beta^2 s^2)^{1/2}) \\ &- \left(\frac{\alpha^2\sin^2 s}{(\alpha^2\sin^2 s + \beta^2 s^2)^{1/2}}\right) K_{2/3}(2(\alpha^2\sin^2 s + \beta^2 s^2)^{1/2}\Big]\end{aligned} \tag{2.5}$$

where s, α and β are non-dimensional parameters defined as

$$s = \omega_0\tau/2 \tag{2.6}$$

$$\alpha = a/L \tag{2.7}$$

$$\beta = U/(L\omega_0). \tag{2.8}$$

The autocorrelation function $\rho(s)$ may be seen in Figure 2.1 compared with the autocorrelation function of stationary von Kármán turbulence. It may be seen that the rotational $\rho(s)$ has a steeper decreases than the fixed $\rho(s)$ for $s < \pi/2$. In the interval $\pi/2 < s < \pi$, the rotational $\rho(s)$ increases to reach the same value as the fixed $\rho(s)$ at $s = \pi$, which is when τ equals the time of one revolution.

The normalized spectral density of the rotationally sampled turbulence may be found by applying the Fourier transform to the autocorrelation function in equation 2.5:

$$\Psi(\Omega) = \frac{1}{2\pi}\int_{-\infty}^{\infty}\rho(s)\mathrm{e}^{-i\Omega s}ds \tag{2.9}$$

where $\Omega = 2\omega/\omega_0$ is a dimensionless frequency.

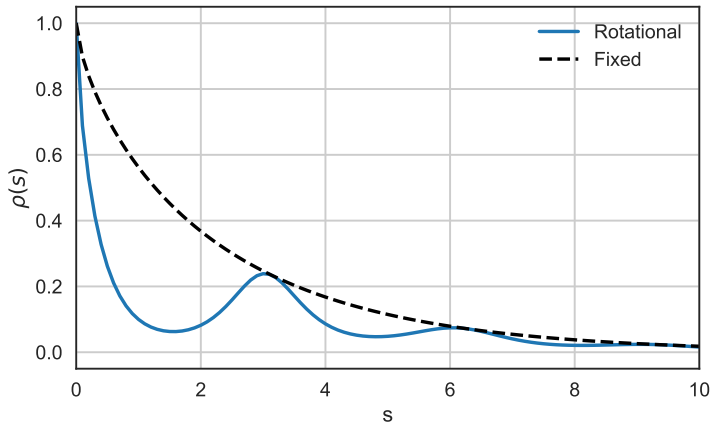

Figure 2.1: The autocorrelation function of rotationally sampled turbulence (blue) and the fixed point von Kármán turbulence (dashed black), shown as function of non-dimensional time lag s. Here $\beta = 0.17$ for both functions, $\alpha = 0.63$ (blue) and $\alpha = 0$ (dashed black).

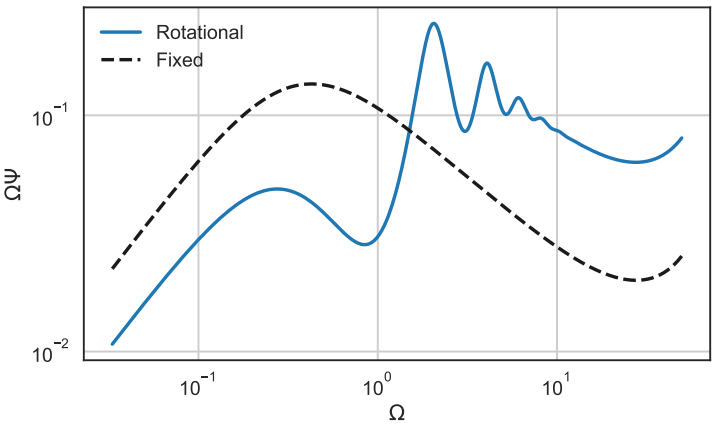

Figure 2.2: The normalized rotationally sampled power spectrum (blue) and the fixed point von Kármán spectrum (dashed black), shown as function of normalized frequency Ω, with $\beta = 0.17$ and $\alpha = 0.63$ (blue) and $\alpha = 0$ (dashed black).

Figure 2.2 shows the discrete Fourier transform of the $\rho(s)$ functions shown in Figure 2.1. We see how the energy gets transferred from low to high frequencies by the rotation and how the high energy is concentrated in narrow bands of frequencies matching multiples of the rotational frequency. We also see the effect of spectral aliasing at the high frequencies, where the spectrum turns upward, deviating from the -2/3 power law (Kristensen and Frandsen, 1982).

2.3 The rotational shaping filter

A rotational shaping filter H_{shape} is defined in frequency space by taking the rotationally sampled spectra in equation (2.9) and dividing by the fixed point spectra:

$$H^2_{\text{shape}}(f) = \frac{\Psi_{\text{rot}}(\Omega)}{\Psi_{\text{fixed}}(\Omega)} \tag{2.10}$$

The spectrum is a function of the normalized frequency $\Omega = \omega/(2\omega_0)$ and the shaping filter is a function of the corresponding frequency $f = \Omega\omega_0/\pi$. The fixed-point spectra in the denominator of equation 2.10 is easily obtained by setting the radius a to zero in equation 2.5 before performing the Fourier transform. In order to apply the effect of rotational sampling, the Fourier transformed wind speed signal is multiplied by the shaping filter:

$$\hat{\text{u}}_{\text{rot}} = H_{\text{shape}}(f)\hat{\text{u}}_{\text{fixed}} \tag{2.11}$$

where $\hat{\text{u}}$ denotes a wind speed signal in frequency domain. The multiplied signal $\hat{\text{u}}_{\text{rot}}$ may be transformed back to time domain by the inverse Fourier transform. This way wind speed signals are manipulated to resemble measurements that are sampled in a rotating frame of reference.

A rotational sampling shaping filter has previously been derived (Burlibaşa and Ceangă, 2013), by combining a couple of empirical transfer functions, three resonant filters and a correction filter which need tuning with an optimization procedure. This filter provides the same effect as our current filter in equation 2.10. However the filter in equation 2.10 is derived through a much simpler, physical approach, which offers a far easier implementation.

2.4 Data filtering and filter parameters

Wind speed measurements from the coastal site Høvsøre are used for filtering and to perform gust statistics. Høvsøre is a test center for wind turbines located in western Jutland. The data consist of 10 Hz cup anemometer and wind wane measurements at 100 m. The cups are mounted on a meteorological mast at southward facing booms. Measurements where the wind is from north are excluded from the analysis. This is done because of flow distortion of the mast itself and the presence of four wind turbines on the north side of the mast, resulting in the mast being in the wake of the turbines. The data spans a period from February 2004 to January 2014. More detail on the measurements and the Høvsøre site may be found at Peña et al. (2016).

The data set is filtered in two different ways:

1. Band-pass filtering with a second order Butterworth filter.
2. Applying the rotational shaping filter $H_{\text{shape}}(f)$.

The effect of the rotational sampling depends on the rotational speed (angular velocity), the radius of the rotation and the length scale of the von Kárman spectrum. As the objective of this analysis is to investigate the influence of the rotation of wind turbine blades on gust statistics, a specific wind turbine is chosen, the NREL 5 MW reference wind turbine Jonkman et al. (2009).

The rotational autocorrelation function equation 2.5 is calculated for each 10 minute sample of wind speed measurements and the non dimensional variables s,α and β are estimated from the 10-minute mean wind speed and three parameters L, a and ω_0. The length scale L is set to 70 m, which is estimated from measurements at 100 m in Høvsøre (Dimitrov et al., 2017). The radius a is set to 70% of the radius of the NREL 5 MW, $a = 44.1$ m. At this radius we can expect approximately 2D aerodynamics of the corresponding blade segment and therefore the highest impact of the u-component of the wind speed fluctuations. The rotational frequency $\omega_0 = 2\pi \cdot 1P$ is estimated from the rated rotor's rotational frequency of the NREL 5 MW, $1P = 0.2$ Hz.

Filter parameters	
Radius, a	$0.7 \cdot 63$ m
Rotational frequency, $1P$	0.20 Hz
Length scale, L	70 m
Butterworth order, n	2
Low cut-off frequency, f_{c1}	$1P/10 = 0.02$ Hz
High cut-off frequency, f_{c2}	$10 \cdot 1P = 2$ Hz

Table 2.1: Parameters for the filtering.

The band-pass filtering is performed using a second-order Butterworth filter (Butterworth, 1930), by multiplying a high-pass filter with a low-pass filter. The magnitude of the frequency response is given by

$$G(f) = \frac{1}{\sqrt{1 + (f/f_{c1})^{2n}}} \cdot \frac{1}{\sqrt{1 + (f_{c2}/f)^{2n}}} \tag{2.12}$$

where f_{c1} is the higher cut-off frequency (for the low pass filter), f_{c2} is the lower cut-off frequency (for the high-pass filter) and n is the filter order. The band-pass filtering is performed with cut-off frequencies $f_c = 1P/10$ Hz for the high-pass and $f_c = 1P \cdot 10$ Hz for the low-pass. This is done in order to eliminate large scale fluctuations and the smallest turbulent fluctuations and peaks from the measurements. The low pass filtering of the measurements is an important step of the data analysis, as the rotational spectral model is based the assumption that the turbulence is stationary and homogeneous.

In Figure 2.3 we see the gain of the Butterworth band-pass filter and the rotational shaping filter with the chosen filter parameters found in Table 2.1. The same parameter values for L, a and ω_0 are also used for the autocorrelation function in Figure 2.1 and the spectra in Figure 2.2.

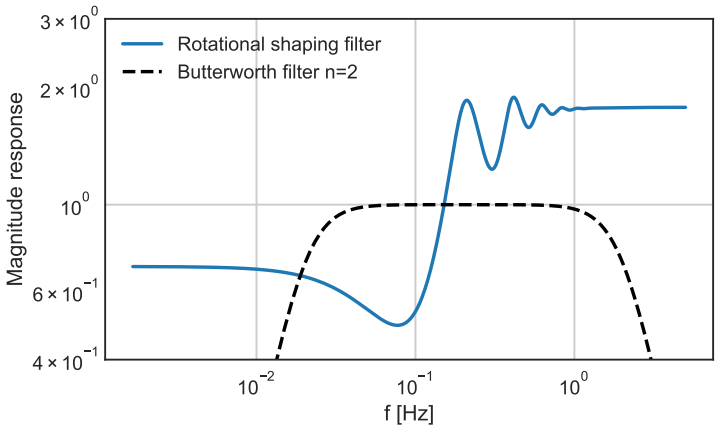

Figure 2.3: The blue line shows the gain of the rotational shaping filter with $\beta = 0.17$ and $\alpha = 0.63$. The black dashed line shows the second order Butterworth filter with f_{c1} =0.02 Hz and $f_{c2} = 2$ Hz.

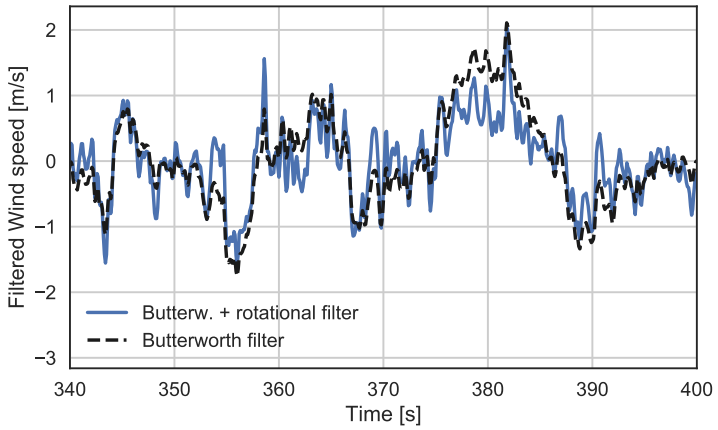

Figure 2.4: Wind speed measurements filtered with a second order Butterworth filter (dashed black) and additionally filtered with the rotational shaping filter (blue).

Figure 2.4 shows an example of a wind speed signal filtered with the Butterworth filter and filtered with both the rotational shaping filter and the Butterworth filter.

2.5 Gust detection and characterization

Only measurements where the 10-minute mean wind speed exceeds 10 m/s are selected for the analysis. This criteria is made for two reasons: First, we can assume a constant rotational speed for the filter parameter ω_0, as the rotational speed of the wind turbine

reaches 95% of the rated rotational speed at 10 m/s. Second, in this wind speed range we expect to find the most extreme gusts. An additional selection criteria is made on the 10-minute standard deviation, where only the highest 50% of the wind speed dependent standard deviations are selected.

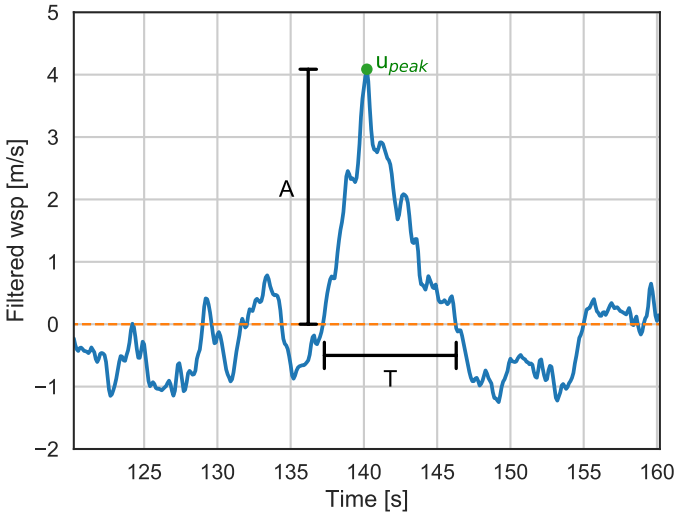

Figure 2.5: Gust characteristics used in the present analysis. A denotes gust amplitude and T denotes gust duration.

The highest peak of each 10-minute wind speed signal is identified (u_{peak}) and only peaks exceeding four times the 10-minute standard deviation are selected for gust characterization, $u_{\text{peak}} > 4 \cdot \sigma_u$.

A gust may be characterized with many different parameters, e.g. velocity increments and constant separation times (Bergström, 1987; Boettcher et al., 2003), extreme values normalized with the standard deviation (Beljaars, 1987; Kristensen et al., 1991) 'gust factor' (Frandsen et al., 2008; Suomi et al., 2013), rise time and velocity jump (Bierbooms, 2005). For the present study, the gusts are characterized by two of the most basic parameters: amplitude and duration (Doran and Powell, 1982; Branlard, 2009).

The amplitude A is defined as the distance from the mean wind speed to the wind speed peak value, and the duration T is defined as the time interval where the fluctuating wind speed is above the mean wind speed around the time of the peak (see Figure 2.5).

2.6 Gust statistics and discussion

Figure 2.6 shows the detected gust amplitudes (A_{filt}) and duration (T_{filt}) as function of mean wind speed for the band-pass filtered measurements. The black line shows the linear regression with coefficients shown in Table 2.2.

In Figure 2.7 we see the gust characteristics A_{rot} and T_{rot} as function of 10-minute mean wind speed and the linear regression estimates indicated with black lines. The

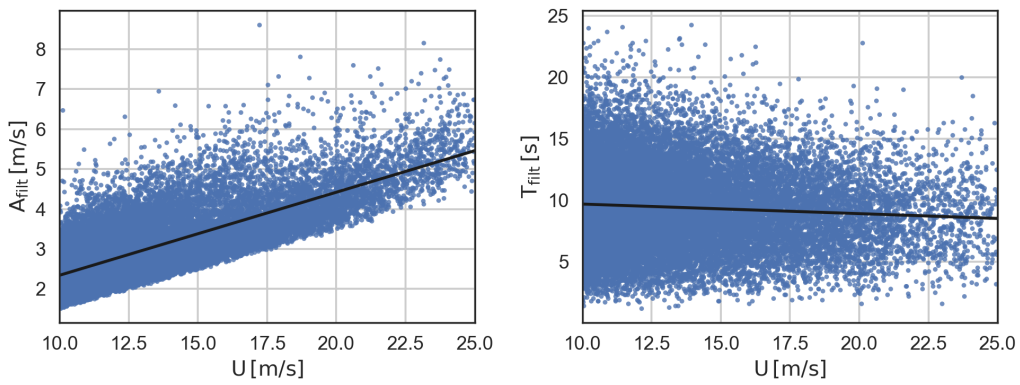

Figure 2.6: Gust amplitudes (left panel) and duration (right panel) as function of 10-minute mean wind speed from filtered measurements with a second order Butterworth filter. The black lines show the linear regression.

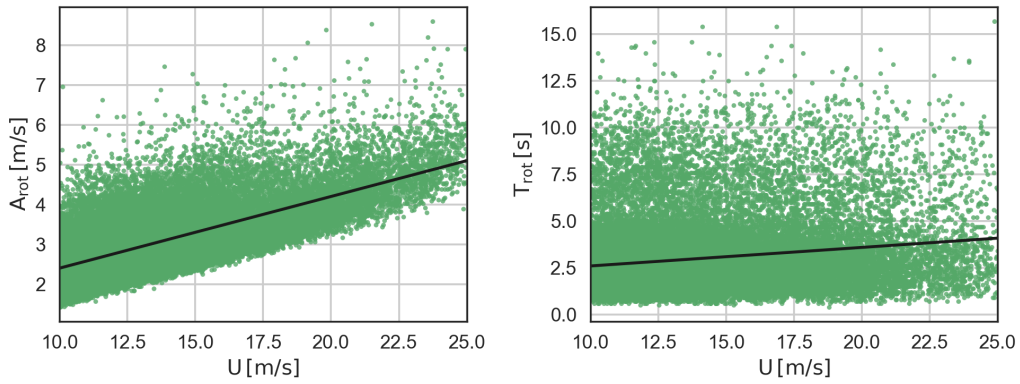

Figure 2.7: Notation same as Figure 2.6, but measurements are additionally filtered with a rotational shaping filter.

measurements are filtered with the rotational shaping filter as well as a second order Butterworth filter. The linear regression parameters may be found in Table 2.2. We see that the gust amplitudes show a clear wind speed dependence for both filtered data sets. Especially the lower boundary of the amplitudes is very clear, due to the selection criteria on the wind speed dependent 10-minute standard deviation and the threshold on the peaks ($4 \cdot \sigma_u$). The wind speed dependence on the gust duration is low, with slopes of -0.078 and 0.099 respectively for the Butterworth-filtered and rotationally filtered data.

The gust amplitudes are shown as function of duration for both filtered data sets in Figure 2.8. While the amplitudes are of similar magnitude for both data sets, it is seen that the gust duration is significantly reduced by effect of rotational sampling. The average duration of the rotationally filtered gusts is 2.95 s, compared with 9.40 s for the Butterworth filtered gusts (see Table 2.3). The correlation is low, with calculated

Data	Slope	Intercept	Standard error
U and A_{filt}	0.21	0.26	0.0012
U and T_{filt}	-0.078	10.47	0.0067
U and A_{rot}	0.18	0.61	0.00094
U and T_{rot}	0.099	1.60	0.0027

Table 2.2: Linear regression coefficients.

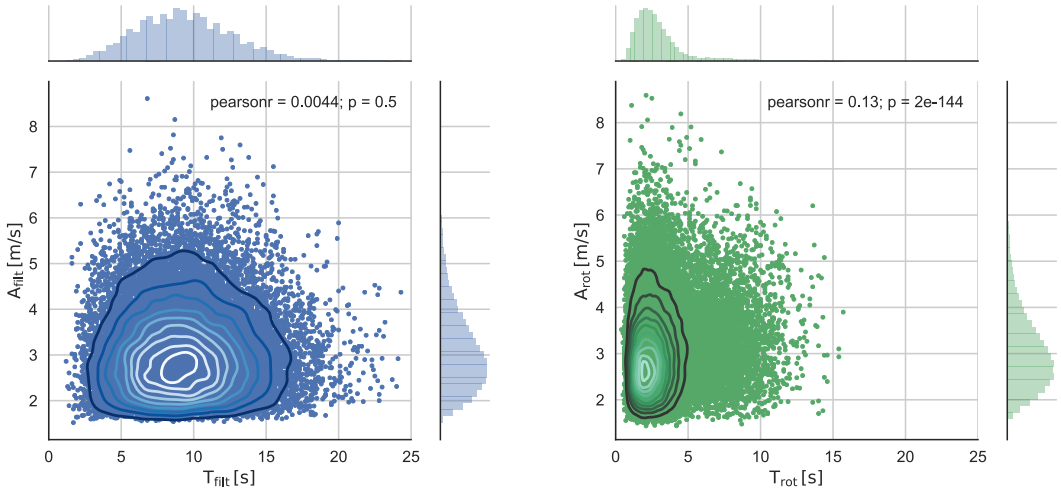

Figure 2.8: Gust amplitude as function of duration estimated from filtered measurements with a second order Butterworth filter (left panel) and additionally a rotational shaping filter (right panel). The contours show kernel density estimates of the joint distribution.

coefficients of 0.0044 and 0.13 respectively (Figure 2.8). The contours show the kernel density estimates of 10 isocontours of probability levels using a Gaussian basis function.

Filtered data set	$\langle$A$\rangle$ [m/s]	$\langle$T$\rangle$ [s]	Nr.of gusts
Butterworth	3.10	9.40	22702
Rot. + Butterw.	3.05	2.95	41164

Table 2.3: Gust statistics for each filtered data set.

The rotational sampling increases the number of detected gusts by a factor of 1.8 (see Table 2.3), although the same selection criteria is used on both data sets.

To investigate how the gust amplitudes change by the rotation, we look at the filtered data set. The change in amplitudes is defined as

$$\Delta A = A_{\text{rot}} - A_{\text{filt}} \tag{2.13}$$

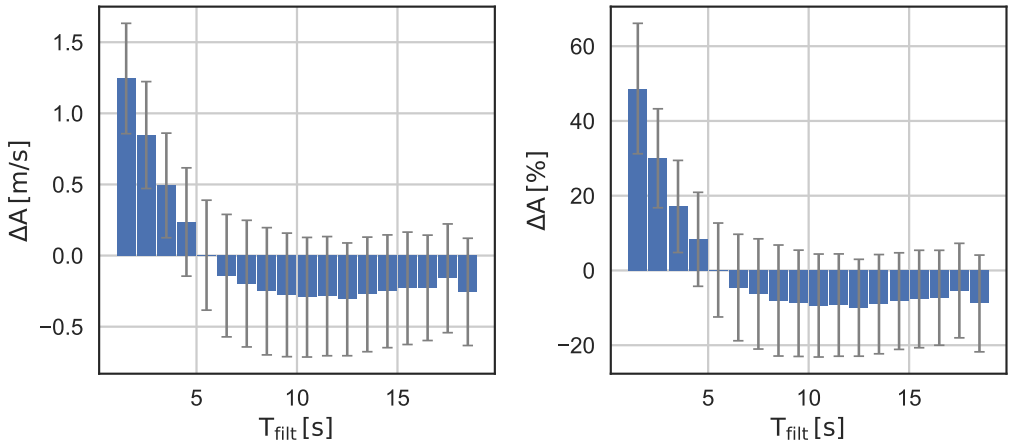

Figure 2.9: Change of gust amplitudes per duration due to the effect of rotational sampling. The error bars show the standard deviation of each bin.

The amplitude change is found for each gust at the exact location of u_{peak} in the filtered data set. Figure 2.9 show the amplitude change ΔA, binned by T_{filt} with bin width of 1 s. The absolute amplitude change is shown as in equation 2.13 (left panel) and relative in percentage, where ΔA is divided by A_{filt}. The error bars show the standard deviation of ΔA for each T_{filt} bin. It may be seen that the amplitude change is on average the largest for the short duration gusts. The gust amplitudes increase on average by the effect of rotational sampling for gust duration below 5 s. Gust of duration 6 s or more are reduced by the effect of rotational sampling. The average gust amplitudes per duration bin are nearly constant (≈ 3 m/s), hence the absolute and relative gust amplitude change are similar.

We see that when the shaping filter is applied to a wind speed signal signal (see Figure 2.3), the frequencies close to- or higher than the rotational frequency of the NREL 5 MW wind turbine rotor get amplified. Especially frequencies matching the 1P and 2P frequencies. This amplification of the high frequencies has a significant impact on the gust statistics of the data set filtered with the rotational shaping filter. In general the amplified frequencies add more peaks to the wind speed signal, with the effect of higher number of detected extreme gusts and significant reduction in gust duration.

We see that the gusts with the shortest duration $1\,s < T_{\text{filt}} \leq 2\,s$ are the ones that are amplified most by the effect of rotational sampling, with relative ΔA up to 96%. As there is a rough proportionality between time- and length scales of atmospheric flow, we can not expect the smallest scale turbulent gusts to have a significant impact on extreme loading of a 5 MW wind turbine. These small scale gusts are likely to be 'filtered out' by the lateral spatial averaging of the rotor, as suggested by e.g. Frandsen et al. (2008) and Berg et al. (2016).

The wind speed measurements used herein are performed in a fixed frame of reference. In the current analysis, the effect of rotational sampling on gust statistics is a combination of measurements and theory. Therefore the estimated effect should mainly be interpreted within this filtered context.

2.7 Conclusion

A simple rotational shaping filter is defined from the spectral model of Kristensen and Frandsen (1982).

The filter is used in combination with measurements to estimate the effect of rotational sampling on gust statistics to be compared with gust statistics in a fixed frame of reference. The effect on gust statistics may be summarized:

- The number of detected extreme gusts is roughly doubled by the effect of rotational sampling.
- The gust duration of rotationally sampled gusts is decreased significantly.
- The amplitudes of gusts with short duration, below 5 s are increased by the effect of rotational sampling, while the gusts with duration above 5 s are lowered.

We observe that the gusts with the shortest duration get amplified the most by the effect of the rotational sampling. As those gusts are likely to be 'filtered' out by the rotor because of the limited spatial extension of fast fluctuations, they are not likely to cause extreme loading on a wind turbine. It may be more appropriate to consider the amplification of short duration gusts in the context of fatigue loading.

The band-pass filtering of the measurements is done to ensure the assumption of stationarity and homogeneity that the spectral model is based on. However, in order to investigate fluctuations that potentially cause extreme loading, it might be necessary not to apply filtering of any kind.

CHAPTER 3
Extreme wind fluctuations

During the period of this PhD project, co-supervisor Jakob Mann was contacted by a wind turbine manufacturer that was experiencing difficulties with specific wind turbine load simulations. They were using measured values of turbulence intensity (10-minute data) from the measurement site Høvsøre. The data was from a ten year period and there was a number of extreme turbulence intensity events that the wind turbine manufacturer used for turbulence simulations. The turbulence intensity of the simulations was matched with the observed extreme turbulence intensity values and used for wind turbine load simulations, that resulted in unrealistically high loads. When investigating high frequency measurements of these events, it was revealed that it was not stationary homogeneous turbulence, but rather ramp-like increases in wind speed.
In the following study these observed extreme events are simulated with a constrained turbulence simulation, and we then investigate the impact on wind turbine loads.
This paper has been through a review process and this is the reviewed version.

Extreme wind fluctuations: joint statistics, extreme turbulence, and impact on wind turbine loads

Ásta Hannesdóttir, Mark Kelly, and Nikolay Dimitrov

DTU Wind Energy Dept., Technical University of Denmark, Roskilde, Denmark

Correspondence to: Ásta Hannesdóttir (astah@dtu.dk)

Abstract. For measurements taken over a decade at the coastal Danish site Høvsøre, we find the variance associated with wind speed events from the offshore direction to exceed the prescribed extreme turbulence model (ETM) of the IEC 61400-1 Ed.3 standard for wind turbine safety. The variance of wind velocity fluctuations manifested during these events is not due to extreme turbulence; rather, it is primarily caused by ramp-like increases in wind speed associated with larger-scale meteorological processes. The measurements are both linearly detrended and high-pass filtered in order to investigate how these events—and such commonly-used filtering—affect the estimated 50-year return period of turbulence levels. High-pass filtering the measurements with a cut-off frequency of 1/300 Hz reduces the 50-year turbulence levels below that of IEC ETM class C, where as linear detrending does not. This is seen as the high-pass filtering more effectively removes variance associated with the ramp-like events. The impact of the observed events on a wind turbine are investigated using aeroelastic simulations, that are driven by constrained turbulence simulation fields. Relevant wind turbine component loads from the simulations are compared with the extreme turbulence load case prescribed by the IEC standard. The loads from the event simulations are on average lower for all considered load components, with one exception: Ramp-like events at wind speeds between 8-16 m/s where the wind speed rises to exceed rated wind speed can lead to high thrust on the rotor, resulting in extreme tower base fore-aft loads that exceed the extreme turbulence load case of the IEC standard.

1 Introduction

The IEC design standard for wind turbine safety (61400-1 edition 3, IEC, 2005) outlines requirements that, when followed, offer a specific reliability level which can be expected for a wind turbine. The standard prescribes various operational wind turbine load regimes and extreme wind conditions that the wind turbine must be able to withstand during its operational lifetime. So-called design-load cases (DLC's) are described, following these prescribed regimes and conditions. One of the IEC prescriptions is an extreme turbulence model (ETM), which gives the ten-minute standard deviation of wind speed, with a 50-year return period, as a function of ten-minute mean wind speed at hub height. The ETM takes into account the long-term mean wind speed at hub height and is scaled accordingly through the wind speed parameters of the IEC wind turbine classes. The model is prescribed in a design load case (DLC 1.3) for ultimate load calculations on wind turbine components; this DLC is considered to be important in wind turbine design, particularly for the tower and blades (Bak et al., 2013). For the standard to be effective, it must reflect the expected atmospheric conditions and the extreme events that a wind turbine may be exposed to. Likewise, it is important that DLC 1.3 is representative of observed extreme turbulence conditions.

The IEC standard recommends the uniform-shear spectral turbulence model of Mann (1994, 1998) for generation of three-dimensional turbulent flow, to serve as input to turbine load calculations. Gaussian turbulent velocity component fluctuations are synthesized via the 'Mann-model' spectra, and assumed to be stationary and homogeneous (unless the model is modified, as in de Mare and Mann, 2016). The model requires three input parameters, which have values prescribed by the standard. In Dimitrov et al. (2017) it is shown that the parameters of normal turbulence and extreme turbulence differ, and how these differences influence wind turbine loads. There it is also shown how numerous 10-minute turbulence measurements from the homogeneous

land (eastern) sectors exceed the ETM model at the Danish Test Centre for Large Wind Turbines at Høvsøre, indicating that the ETM model is not necessarily conservative.

A further investigation of 10-minute turbulence measurements exceeding the ETM level is needed to identify what kind of flow causes these extreme events and how they influence the estimated turbulence level at a given site. Fluctuations associated with mesoscale meteorological motion can have periods in the range of a minute up to hours (Vincent, 2010). In the shorter end of this range the fluctuations are the main contribution to the 10-minute variance estimate (turbulence level). Short-time mesoscale fluctuations have been reported in connection with e.g. open cellular convection (Vincent et al., 2012), convective rolls (Foster, 2005) and streaks (Foster et al., 2006). The fluctuations are seen in measurements as coherent structures with a ramp-like increase in wind speed (Fesquet et al., 2009). These studies have been made with respect to identification, modelling, forecasting and wind power generation, but they do not consider the impact on wind turbine loads.

In this paper we aim to find and examine events where the 10-minute variance exceeds the ETM level. However here we consider them as non-turbulent events, as they are caused by ramp-like increase in wind speed associated with larger-scale meteorological processes, which may be observed offshore or high above the surface layer. We use measurements from the measurement site Høvsøre, focusing on the western (offshore) sectors. We demonstrate how these events influence the estimate of 10-minute turbulence levels with a 50-year return period. This is done for the raw-, linearly detrended-, and high-pass filtered measurements. The observed events are simulated by incorporating measured time series using a constrained simulation approach, in order to get a realistic representation of the flow involved. The generated wind field realizations are fed to an aero-elastic model (Larsen and Hansen, 2015) of the DTU 10MW reference wind turbine (Bak et al., 2013), to investigate how they affect wind turbine loads. Finally, the load simulations with the observed events are compared to simulations corresponding to DLC 1.3 from the IEC 61400-1 standard.

2 Site and measurements

The data analysis and load simulations are based on measurements from the Høvsøre Test Centre for Large Wind Turbines in western Denmark. Located over flat terrain 1.7 km east of the coastline, the site offers low-turbulence, near-coastal wind conditions. The site consists of five wind turbines arranged in a single row along the north-south direction, and multiple measurement masts.

The primary data source used in this paper is a light mast[1] placed between two of the wind turbines. This mast has cup anemometers and wind vanes at 60 m, 100 m and 160 m heights installed on southward pointing booms. The measurements span a 10-year period, from November 2004 to December 2014 and the recording frequency is 10 Hz. The light-mast data is compared with data from the main Høvsøre meteorological mast, which is located south of all wind turbines and approximately 400 m south of the light mast, as may be seen in Figure 1. More details on the site, instrumentation and observations may also be found in Peña Diaz et al. (2016).

We consider measurements only from the western sector, with 10-minute mean wind direction between 225° and 315°. This range of wind directions is chosen for two reasons: (i) to avoid measurements from the wakes of the wind turbines and flow distortion from the mast; (ii) data from this sector corresponds to coastal and offshore conditions.

2.1 Selection criteria of extreme events

For the selection of the extreme variance events the 10-minute standard deviation of the wind speed measurements is compared to the extreme turbulence model in the IEC 61400-1 standard (IEC, 2005), where the horizontal turbulence standard deviation is given by

$$\sigma_1 = c \cdot I_{\text{ref}} \left[0.072 \left(\frac{V_{\text{ave}}}{c} + 3 \right) \left(\frac{V_{\text{hub}}}{c} - 4 \right) + 10 \right]. \qquad (1)$$

Here c is a constant of 2 m/s, I_{ref} is the reference turbulence intensity at 15 m/s, V_{ave} is the annual average wind speed at hub height, and V_{hub} is the 10-minute mean wind speed at hub height; the variable of which σ_1 is a linear function of. For the 'offshore' westerly directions considered at Høvsøre the long-term (10-year) mean of 10-minute average wind speeds at 100 m height is U=10.4 m/s, which corresponds well to class I turbines within the IEC 61400-1 framework with V_{ave}=10 m/s.

The IEC standard has three turbulence categories: A, B and C, with A being the highest reference turbulence intensity, and C the lowest. The corresponding reference TI for each class may be seen in Table 1. At Høvsøre, the (decade-long) average TI corresponding to the IEC reference wind speed, i.e. 10-minute mean wind speeds of $U = 15 \pm 0.5$ m/s, is below 0.12. This indicates that the reference turbulence class C and I_{ref} of 0.12 will equal or exceed in severity the actual conditions at the site. However, for the selection of events to analyze, a criterion corresponding to the IEC ETM model with turbulence class B is used. This is done in order to limit the selection to a representative subset of the most extreme events, while also limiting computational demands. The selected events can be seen in Figure 2 as blue dots that fall above the blue curve, i.e. these are events that have a high horizontal wind speed variance. The events are selected from measurements at 100 m height.

Figure 3 shows the horizontal wind speed at 100 m from the light mast and meteorological mast during six of the selected events. The events typically include a sudden rise in

[1] The light mast has aircraft warning lights on the top.

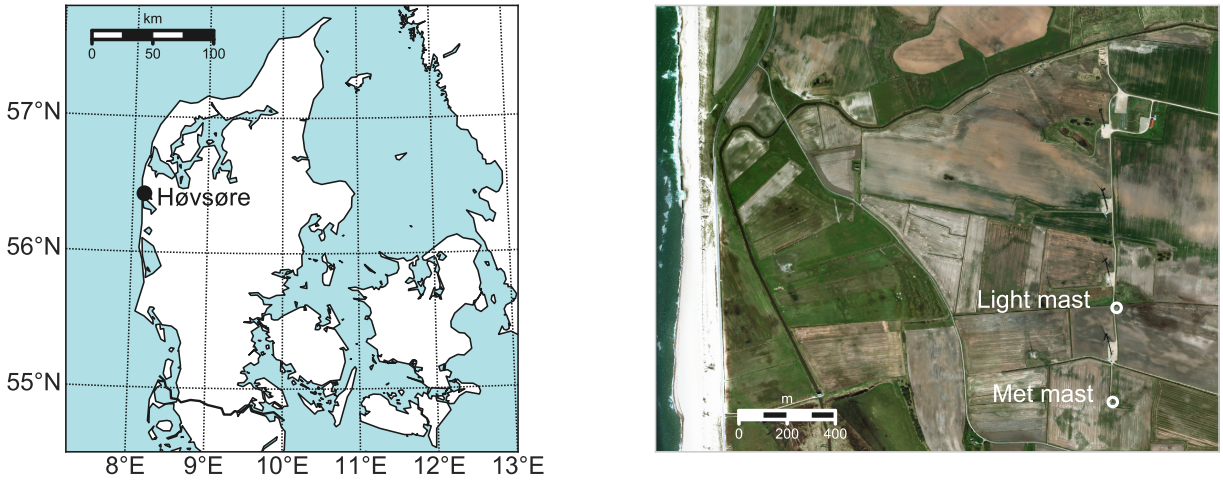

Figure 1. *Left:* Map of Denmark showing the location of Høvsøre. *Right:* Overview of the Høvsøre test center showing the position of the met mast and the light mast with white circles.

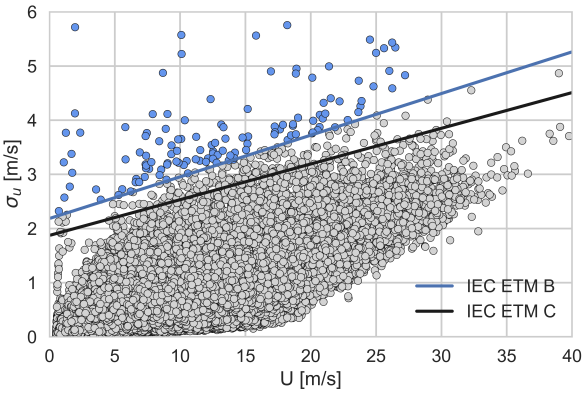

Figure 2. The dots correspond to 10-minute standard deviation of the wind speed as a function of U at 100 m height over a 10-year period. The black and blue curves show the IEC extreme turbulence model, class C and class B respectively. The selected events (blue dots) are σ_u values exceeding the extreme turbulence model class B.

Turbulence class	I_{ref}
A	0.16
B	0.14
C	0.12

Table 1. The IEC turbulence classes and associated turbulence intensities.

wind speed, which gives the main contribution to the high variance. Notice the sudden wind speed increase occurs approximately simultaneously at the two masts although they are ∼400 m apart (for mean wind direction roughly perpendicular to the line connecting the masts), indicating that the events are due to large coherent structures—rather than extreme stationary turbulence.

3 Data processing

The data set used for the data analysis and simulation is the 10 Hz measurements from cup anemometers and wind vanes on the light mast in Høvsøre.

3.1 Estimation of 50-year joint extremes of turbulence and wind speed: IFORM analysis

The measurements shown earlier in Figures 2 and 3 are raw (not processed or filtered), though it is common procedure to detrend data before estimating turbulence or associated return periods for a given turbulence level. Not all the extreme variance events are expected to be influenced by linear detrending, nor is such detrending necessarily appropriate for non-turbulent events; note e.g. the event shown in Figure 3c. Therefore we want to compare the 50-year return period of turbulence with the data, detrended in two different ways: linear detrending and high-pass filtering. Detrending is performed by making a linear least-squares fit to the raw 10-minute wind speed time series, with the linear component subsequently subtracted from the raw data.

The high-pass filtering is performed with a second-order Butterworth filter (Butterworth, 1930), where the magnitude of the frequency response function (the gain) is given by

$$G(f) = \frac{1}{\sqrt{1+(f_c/f)^4}} \quad (2)$$

where f_c is the 'cut-off' frequency. We perform the filtering using a cut-off frequency of 0.0017 Hz (1/600 Hz) and

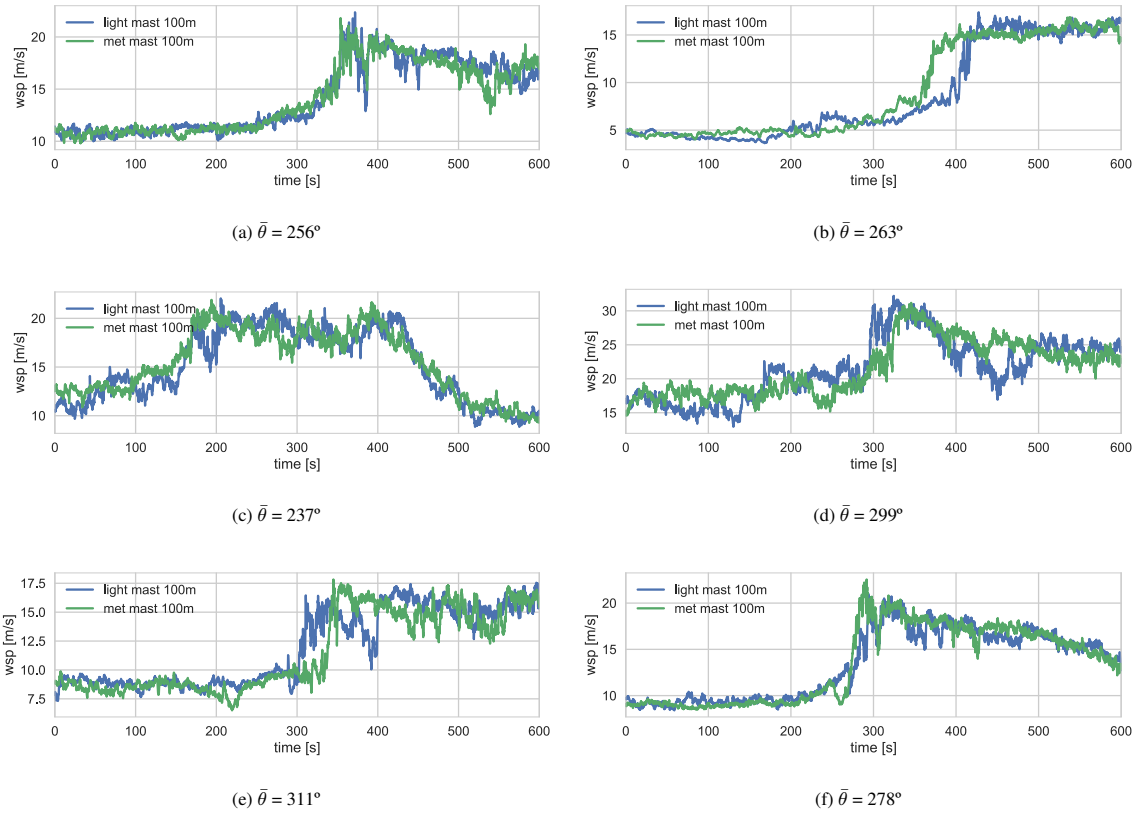

(a) $\bar{\theta} = 256°$ (b) $\bar{\theta} = 263°$

(c) $\bar{\theta} = 237°$ (d) $\bar{\theta} = 299°$

(e) $\bar{\theta} = 311°$ (f) $\bar{\theta} = 278°$

Figure 3. Comparison of horizontal wind speed measurements at the meteorological mast (green curve) and the light mast (blue curve). The measurement height is 100 m at both masts, which are separated by $\approx$ 400 m. The 10-minute averaged wind direction $\bar{\theta}$ is from the light mast.

also with a higher cut-off frequency of 0.0033 Hz (1/300 Hz). The higher cut-off frequency chosen for the high-pass filtering corresponds to fluctuations with periods of 300 s (half of the sample period of the measurements). This choice of cut-off frequency ensures removal of trends in the range 2.5–10 minutes (low-frequency transients), and is considered conservative enough to still include fluctuations associated with turbulent eddies.[2]

Here we use the inverse first-order reliability method (IFORM) to estimate the 50-year return period contour corresponding to the joint description of turbulence (σ_u) and 10-minute mean wind speed (U). This method was developed by Winterstein et al. (1993) and provides a practical way to evaluate joint extreme environmental conditions at a site. The IFORM method is widely used in wind energy to predict extreme environmental conditions or long-term loading on wind turbines, for ultimate strength analysis. More information on this method may be found in e.g. Fitzwater et al. (2003); Saranyasoontorn and Manuel (2006); Moon et al. (2014).

The first step in the IFORM analysis is to find the joint probability distribution $f(U, \sigma_u)$. According to the IEC standard the 10-minute mean wind speed is assumed to follow a Weibull distribution [3], and the 'strength' (standard deviation) of turbulent stream-wise velocity component fluctuations (σ_u) is assumed to be log-normally distributed conditional on wind speed. In the standard, the mean of σ_u is expressed as a function of U,

$$\mu_{\sigma_u} = I_{\text{ref}}(0.75U + 3.8\,\text{m/s}), \tag{3}$$

and the standard deviation of σ_u is defined as

$$\sigma_{\sigma_u} = 1.4 I_{\text{ref}}. \tag{4}$$

In Figure 4, μ_{σ_u} and σ_{σ_u} are shown as functions of 10-minute mean wind speed, from Høvsøre unprocessed measurements at 100 m (grey dots) and the expressions from the

[2] Fluctuations with a period of 300 s at 4 m/s–25 m/s (the operational wind speed range of a typical wind turbine) correspond to length scales of 1200 m–7500 m. Length scales in this range are significantly larger than turbulent length scales that have been estimated at the Høvsøre site (e.g. Sathe et al., 2013; Dimitrov et al., 2017; Kelly, 2018)

[3] Here we use a 3-parameter Weibull distribution. This is done because after filtering out measurements with errors and missing periods, the lowest mean wind speed is 2.2 m/s. One could also use a weighted 2-parameter Weibull distribution fit with increased weights in the tail to obtain the same result.

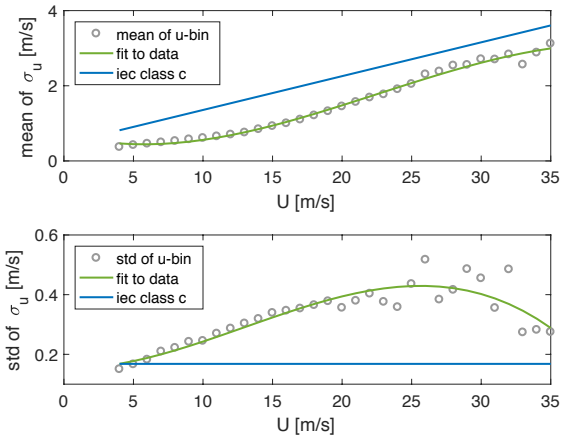

Figure 4. The mean and standard deviation of σ_u as function of wind speed at 100 m, for raw data (not de-trended or filtered). The blue curves show the the IEC expressions, the grey dots show the measured values and the green curves show a polynomial fit to the measurements.

IEC standard (blue lines) with $I_{\text{ref}} = 0.12$. The green lines show a third- and a second order polynomial fit to the binned measurements of μ_{σ_u} and σ_{σ_u} respectively (bins of 1 m/s). The IEC expression for μ_{σ_u} is higher than that from the measurements, but has a similar slope for mean wind speeds above 15 m/s. The difference is larger between the data and IEC expression for σ_{σ_u}, where the assumption of no mean wind speed dependency does not fit well to the data.

The next step in the IFORM analysis is to obtain a utility "reliability index" β which translates the desired return period T_r (here 50-years) into a normalized measure corresponding to number of standard deviations of a standard Gaussian distribution:

$$\beta = \Phi^{-1}\left(1 - \frac{T_t}{T_r}\right) = \Phi^{-1}\left(1 - \frac{1}{5n_m}\right) \tag{5}$$

Here Φ^{-1} is the inverse Gaussian cumulative distribution function (cdf), T_t is the duration of a turbulence measurement (here 10 minutes) and n_m is the number of 10-minute measurements corresponding to a 10-year period (which equals the time span of the data). Thus the reliability index equals the radius of a circular contour in standard Gaussian space, so that

$$\beta = \sqrt{u_1^2 + u_2^2}, \tag{6}$$

where the standard normal variables u_1 and u_2 are derived from physical variables using an iso-probabilistic transformation, which takes correlations into account. We invoke the Rosenblatt transformation (Rosenblatt, 1952), which relies on the fact that a multivariate distribution may be expressed as a product of conditional distributions: $F(x_1, x_2) = F(x_1)F(x_2|x_1)$. In this analysis, only two variables are considered, and the transformation may be performed in the following way:

$$U = F_U^{-1}\Big(\Phi(u_1)\Big) \quad , \quad \sigma_u = F_{\sigma_u|U}^{-1}\Big(\Phi(u_2)\Big) \tag{7}$$

where F_U is the three-parameter Weibull cdf and $F_{\sigma_u|U}$ is the conditional log-normal cdf.

Figure 5 shows the joint distribution of mean wind speed and turbulence, with contours corresponding to the 50-year return period. The contours are calculated based on the measurements (green curves), and the IEC expressions (blue curves) of μ_{σ_u} and σ_{σ_u} respectively. The parameters of the marginal distribution of the 10-minute mean wind speed data were found with maximum likelihood estimation of the three-parameter Weibull distribution (scale parameter: 9.75 m/s, shape parameter: 2.02, location parameter: 2.20). The parameters for the conditional log-normal distribution were estimated with the first and second moments, conditional on mean wind speed: μ_{σ_u} and σ_{σ_u}, both with the IEC expressions in Eqs. 3 and 4 and the third- and second-order polynomial fit to the binned data. It is seen when comparing Figures 5a to 5d that the variance of σ_u is significantly reduced by the high-pass filtering. The 50-year return period contour estimated with the linearly detrended data (Figure 5b) exceeds the one estimated with IEC turbulence class C in the whole operational wind speed range. This is because the linear detrending does not affect events like the one seen in Figure 3c, and these events influence the estimate of the contour. Figure 5c shows the high-pass filtered measurements with a cut-off frequency of 1/600 Hz, and here it is seen how the estimated 50-year return period contour exceeds the IEC turbulence class C contour for wind speeds between 6 m/s and 22 m/s. In Figure 5d, it is seen how the high-pass filtering with cut-off frequency of 1/300 Hz reduces the variance estimates to the extent that the 50-year contour obtained in this way gives turbulence levels lower than ETM IEC class C. These observed changes in turbulence levels indicate that the extreme variance events are not necessarily associated with linear trends. Some events are associated with wind speed fluctuations in a frequency range that may have a substantial impact on wind turbine loads. Therefore we investigate this impact, with constrained turbulence simulations incorporating the raw measurements that have not been detrended in any way.

3.2 Time series for simulation

The peak and the corresponding location of each event is identified in the following way: A moving average is subtracted from the wind speed signal and the maximum value of the differences identified:

$$u_{\text{peak}} = \max(u - \bar{u}_{60s}) \tag{8}$$

where u is the horizontal wind speed signal and $\bar{u}_{60s}$ is the moving average over 60 s. The peaks are not necessarily the

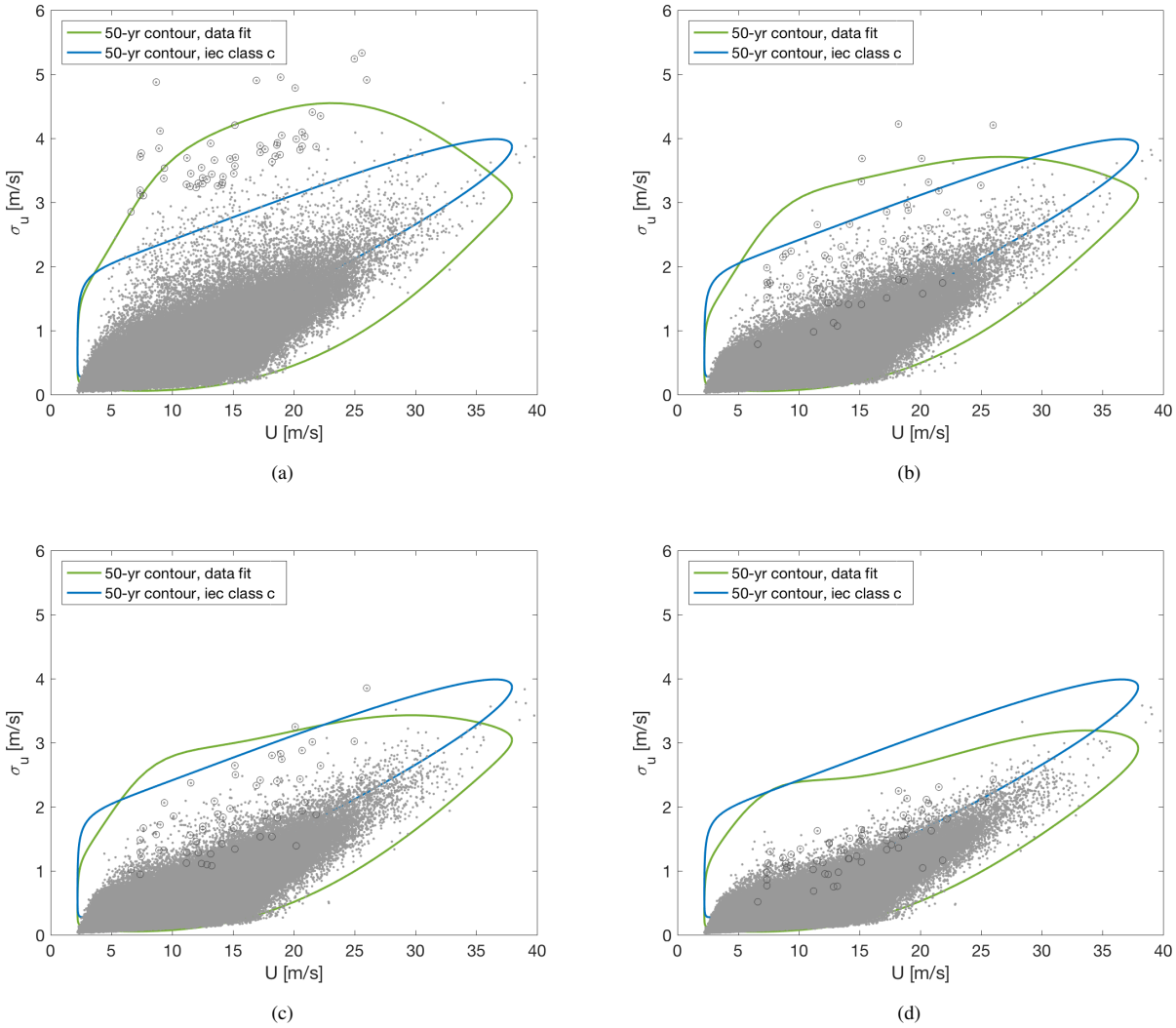

Figure 5. The 50-year return period contours based on the measurements (green curves) and the IEC expressions (blue curves). The grey dots show the measurements. a) Raw measurements. b) Linearly detrended measurements. c) High-pass filtered measurements with a cut-off frequency: 1/600 Hz. d) High-pass filtered measurements with a cut-off frequency: 1/300 Hz. The dark grey circles indicate the extreme variance events.

highest value of the signal, but rather the highest value within a sharp wind speed increase.

Applying the selection criteria described in section 2.1 results in 99 identified events. Of these, 30 events are discarded as they include periods of missing measurements. A lower threshold of 4 m/s is put on u_{peak} to exclude events mostly consisting of a linear trend or relatively insignificant peaks. Finally, events where the corresponding directional data fluctuated below 180º are discarded, i.e. temporary directional data from South, to exclude measurements from the wake of the nearby wind turbine. A remaining 44 events are chosen for load simulations. The measured time series including the extreme events are used to generate constrained turbulence simulations (explained in more detail in Section 4.4) of 600 s duration. The time series period is selected such that the sharp wind increase, or ramp, occurs approximately in the middle of the time series, i.e., approximately 300 s before and after the peak.

4 Load simulation environment

4.1 HAWC2 and the DTU 10 MW

Wind turbine response in the time domain is calculated with HAWC2 (Horizontal Axis Wind turbine simulation Code 2nd generation, Larsen and Hansen, 2015). HAWC2 is based on a multibody formulation for the structural part, where each body consists of Timoshenko beam elements. All the main components of a wind turbine are represented by these independent bodies and connected with different kinds of al-

gebraic constraints. The aerodynamic forces are accounted for with blade element momentum theory (see e.g. Hansen, 2013) with additional correction models: a tip correction model, a skewed inflow correction, and a dynamic inflow correction. HAWC2 additionally includes models that account for dynamic stall, wind shear effects on induction, tower-induced drag, and tower shadow.

All the load simulations are performed using the DTU 10 MW reference wind turbine (RWT), which is a virtual wind turbine model based on state-of-the-art wind turbine design methodology. The main characteristics of the RWT may be seen in Table 2 and a more detailed description may be found in Bak et al. (2013). The controller used for the RWT is the Basic DTU Wind Energy controller (Hansen and Henriksen, 2013).

DTU 10 MW RWT	
Rotor diameter	178.3 m
Cut-in wind speed	4 m/s
Rated wind speed	11.4 m/s
Cut-out wind speed	25 m/s
Cut-in rotor speed	6 rpm
Rated rotor speed	9.6 rpm
Hub height	119 m

Table 2. The main characteristics of the reference wind turbine.

4.2 Turbulence simulations in HAWC2

The Mann spectral turbulence model (Mann, 1994, 1998) is fully integrated into HAWC2, where a turbulence 'box' may be generated for every wind turbine response simulation. The turbulence box is a three dimensional grid that contains a wind velocity vector at each grid point. The turbulence boxes in this study all have $8192 \times 32 \times 32$ grid points, in the x-, y-, and z-directions, respectively. The y-z plane is parallel with the rotor, and the distance between the grid points is typically defined so that the domain extent in the y- and z-directions becomes a few percent larger than the rotor diameter. The length of the x-axis (L_x) is proportional to the mean wind speed at hub height, $L_x = U \cdot T$, where T is the simulation time. The turbulence box is transported with the average wind speed at hub height through the wind turbine rotor.

The Mann model is based on an isotropic von Kármán turbulence spectral tensor, which is distorted by vertical shear caused by surface friction. Assumptions of constant shear and neutral atmospheric conditions in the rapid-distortion limit are used to linearize the Navier-Stokes equations, which may then be solved as simple linear differential equations. The solution results in a spectral tensor that may be used in a Fourier simulation, to generate a random field with anisotropic turbulent flow. The Mann model contains three parameters:

- Γ is an anisotropy parameter, that when positive, $\sigma_u^2 > \sigma_v^2 > \sigma_w^2$, which are the variances of the u-, v- and w-components of the wind speed, respectively. When $\Gamma = 0$, the generated turbulence is isotropic, $\sigma_u^2 = \sigma_v^2 = \sigma_w^2$.
- $\alpha\varepsilon^{2/3}$ is the product of the Kolmogorov spectral constant and the rate of turbulent kinetic energy dissipation to the power of 2/3. The Fourier amplitudes from the spectral tensor model are proportional to $\alpha\varepsilon^{2/3}$, hence increasing $\alpha\varepsilon^{2/3}$ gives a proportional increase in the simulated turbulent variances, but no change in the shape of the spectrum.
- L is the length scale which is representative of the eddy size that contains the most energy.

The IEC-recommended values of the parameters are: $\Gamma = 3.9$, L =29.4 m (for hub heights above 60 m), and that $\alpha\varepsilon^{2/3}$ is set to a positive value, to be scaled with σ_u^2. It has been shown in numerous studies that these parameters can change significantly, e.g. with turbulence level (Dimitrov et al., 2017; Kelly, 2018), atmospheric stability (Sathe et al., 2013; Chougule et al., 2017) and site conditions (Kelly, 2018; Chougule et al., 2015). As we do not want to investigate the effect of changing these parameters, all turbulence realizations are chosen to have the same parameters. In the present study, the anisotropy parameter is chosen according to the IEC standard, $\Gamma = 3.9$. The turbulence length scale is chosen differently, because the DTU 10 MW RWT is a relatively large wind turbine, and the turbulence length scale is expected to be of the same order of magnitude as the hub height (Kristensen and Frandsen, 1982). Here the length scale is estimated via

$$L = \frac{\sigma_u}{dU/dz} \tag{9}$$

as derived by Kelly (2018). The final 200 s of simulation data, i.e. after the wind-speed ramps, are used to estimate the length scale of turbulence and thus exclude the large coherent structure. Here σ_u from 100 m height is used, along with dU/dz estimated between $z = 160$ m and $z = 60$ m. Using (9) the length scale is found on average to be $\langle L \rangle \approx 120$ m over all events analyzed. The value chosen is therefore $L = 120$ m.

4.3 Design load case 1.3

The DLC is simulated based on the setup described in Hansen et al. (2015), where mean wind speeds at hub height of 4–26 m/s in steps (bins) of 2 m/s are used, and each simulation has a duration of 600 s[4]. The Mann turbulence model is used to generate Gaussian turbulence boxes, with six different synthesized turbulence seeds per mean wind speed. The simulation time of the turbulence boxes is defined to be 700 s,

[4]In contrast with Hansen et al. (2015), here the simulations are performed without yaw misalignment.

where the first 100 s are used for initialization of the wind turbine response simulation, and are disregarded for the load analysis.

In the current study we generate Gaussian turbulence fields only, even though it is known that atmospheric turbulent fields can exhibit non-Gaussian character. However, for the purpose of wind turbine response, the difference between Gaussian and non-Gaussian turbulence as input has been shown to generally give insignificant difference for turbine loads (Berg et al., 2016).

4.4 Constrained turbulence simulations

The aim here is to generate turbulence simulations resembling the measured wind field of the extreme variance events. This is done by constraining the synthesized turbulence fields. The constraining procedure involves modifying the time series to represent the most likely realization of a random Gaussian field which would satisfy the constraints, using an algorithm described in Hoffman and Ribak (1991) and demonstrated with applications to wind energy in Nielsen et al. (2004) and Dimitrov and Natarajan (2017). For the constraining procedure we define three different random Gaussian fields as a function of location, $\mathbf{r} = \{x, y, z\}$:

1. the constrained field, $f(\mathbf{r})$, which is the generated field of the procedure, modified to resemble the measurements;
2. the source field, $\tilde{f}(\mathbf{r})$, which here is a random realization of the Mann turbulence model;
3. the residual field, which is the difference between the constrained field and the source field, $g(\mathbf{r}) = f(\mathbf{r}) - \tilde{f}(\mathbf{r})$.

The constraints are a set of M values at given locations, $C = \{c_1(\mathbf{r}_1), c_2(\mathbf{r}_2), ..., c_M(\mathbf{r}_M)\}$, which the constrained field is subject to, and is defined to have the required values at the given locations, $f(\mathbf{r}_i) = c_i$. At the constraint points, the residual field is given by $g(\mathbf{r}_i) = c_i - \tilde{f}(\mathbf{r}_i)$, and for all other locations the values are conditional on the constraints in C. The conditional probability distribution of the residual field is denoted by the multivariate Gaussian distribution function:

$$\phi(g(\mathbf{r})|C) = \frac{\phi(g(\mathbf{r}), C)}{\phi(C)} \tag{10}$$

The conditional probability function of the field may be described as a shifted Gaussian around the ensemble average of $g(\mathbf{r})|C$,

$$\langle g(\mathbf{r})|C\rangle = R_i(\mathbf{r}) R_{ij}^{-1} (C - \tilde{f}[\mathbf{r} = \mathbf{r}(c_i)]) \tag{11}$$

where $\langle ...\rangle$ is the ensemble average, $R_i(\mathbf{r}) = \langle f(\mathbf{r}) C_i\rangle$ are the cross-correlation terms between the field and the constraints, $R_{ij} = \langle C_i C_j\rangle$ is the correlation between the constraints, and $\tilde{f}[\mathbf{r} = \mathbf{r}(c_i)]$ are the values of the source field at the constraints' locations.

A realization of the constrained field is generated by adding the conditional ensemble mean of the residual field to the source field

$$f(\mathbf{r}) = \tilde{f}(\mathbf{r}) + \langle g(\mathbf{r})|C\rangle \tag{12}$$

Here the constraints consist of the u- and v-components of the wind velocity measurements from the light mast. The constraints are applied at three different heights : 79 m, 119 m (hub height) and 179 m, i.e. shifted up 19 m so the measurements at 100 m represent hub height wind speed. The constraints are also applied at three different widths (along the y-axis): 89.6 m (the middle of the turbulence box) $\pm$70 m. This is done to ensure the coherent structure of the observed flow in the simulations. Every third measurement is applied at each width along the y-axis, giving applied constraints at each y-location with a 3.33 Hz frequency.

In Figure 6 two turbulence boxes with different random seeds are seen. The u-component of the turbulent field is shown with a color scale on slices along the time axis. The upper plots show the unconstrained turbulence boxes, and the lower plots show the same turbulence boxes with constraints corresponding to measurements from two different extreme variance events. Figure 7 shows two examples of the u-velocity time series at hub height with and without applied constraints, for the same turbulence seeds as shown in Figure 6.

For the purpose of load simulations, six different constrained turbulence seeds are generated from each extreme variance event time series. Although applying the constraints makes the turbulence boxes similar in general, there are differences in the parts of the boxes which are far from the constraint locations. As a result, there will be a seed-to-seed variation in loads simulated with constrained turbulence boxes, albeit much smaller than what is seen in the unconstrained case.

5 Load simulation results

In this section we compare the design load levels of the two simulation sets: DLC 1.3 and the constrained simulations with the extreme variance. DLC 1.3 consists of 72 simulations (6 seeds per 12 wind speed bins) and the constrained simulations consist of 264 simulations (6 seeds per 44 extreme variance event).

5.1 Extreme loads

In Figure 8 the standard deviation of the simulated hub height u-component wind speed is shown as function of the mean hub height u-component wind speed. Each dot shows the standard deviation averaged over six turbulence seeds. As the variance is scaled to match the target both for DLC 1.3 and the constrained simulations, the scatter of the mean standard deviation over the six different seeds is small. The standard

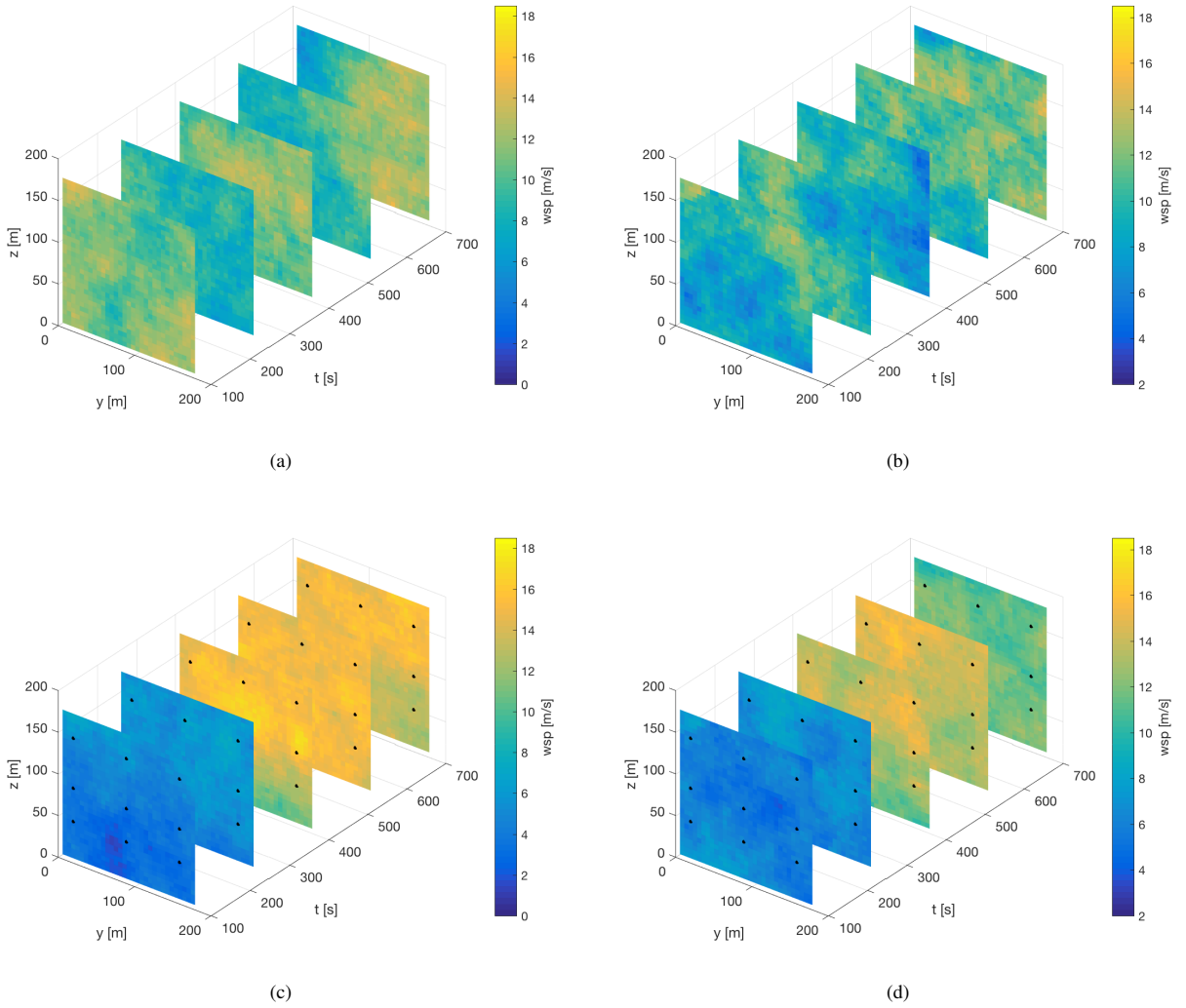

Figure 6. Comparison between u-velocity components from unconstrained turbulence simulations, and from turbulence simulations with velocity jumps included using constrained simulation. a) Seed 1003 without constraints. b) Seed 1005 without constraints. c) Seed 1003 with constraints. d) Seed 1005 with constraints. Constraint locations are shown with black dots.

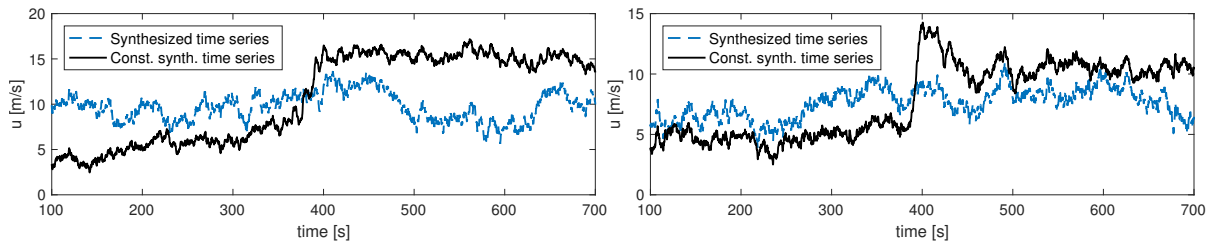

Figure 7. Comparison of unconstrained and constrained stream-wise (u-) velocity component in the middle of the turbulence box,y=89.6 m, z=119 m. *Left:* Seed 1003. *Right:* Seed 1005.

error of the mean standard deviation is in the range of 0.008 - 0.013 m/s, and the standard error of the mean hub-height u-component wind speed is equal to, or less than 0.015 m/s. The standard deviation from the constrained turbulence simulations (blue dots) is higher than that of DLC 1.3 with one exception. For this case, some variance was lost as a consequence of changing the time interval selection to span ± 300 s around the wind speed peak, and data with a negative trend was cut off.

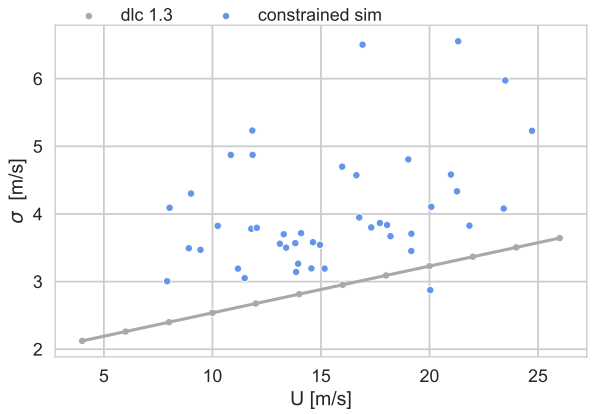

Figure 8. The mean standard deviation of the u-component of the simulated wind speed at hub height as function of mean wind speed at hub height. DLC 1.3 (grey dots) and constrained simulations with extreme variance events (blue dots).

In Figure 9 the characteristic extreme loads from DLC 1.3 and the constrained simulations are compared. The maximum/minimum load values of each 10-minute HAWC2 simulation are binned according to wind speed with a bin width of 2 m/s and then averaged. For the comparison we omit the wind speed bin at 26 m/s, as there are no observed events within that wind speed bin. The error bars show the standard deviation of the extreme loads of each wind speed bin. Both maxima and minima are shown for the tower-top moments, but for all other load components only the maximum moments are shown. It should be noted that the in-plane blade root flap moment maxima are negative, due to the orientation of the blade coordinate system of the wind turbine model in HAWC2.

The two top panels show the extremes of the tower top tilt and yaw moments, respectively. In the whole wind speed range the mean extreme moments for DLC 1.3 are between 6400 - 21000 kNm larger than for the constrained simulations.

The left middle panel shows the mean extreme tower base fore-aft moments. The overall highest mean extreme moment is from the DLC 1.3 simulation set, however for the constrained turbulence simulations the loads are higher for wind speed bins at 8 m/s and between 14-20 m/s. The largest difference is seen for wind speed bin 16 m/s where the mean extreme moment from the constrained simulation is 50200 kNm larger than from the DLC 1.3.

The right middle panel shows the mean extreme tower base side-side moments. In the whole wind speed range the mean extreme moments for the DLC 1.3 are between 6000 - 22500 kNm larger than for the constrained simulations.

The two bottom panels show the blade root- flap and and edge moments respectively. In the whole wind speed range the mean extreme moments for the DLC 1.3 are between 800 - 6200 kNm larger than for the constrained simulations, with the exception of wind speed bin 16 m/s, where the mean extreme moments from the constrained simulations are respectively 3000 kNM and 400 kNm higher than the DLC 1.3.

The extreme tower top tilt-, yaw- and tower base side-side moments show a general increase with wind speed. The extreme blade root flap- and tower base fore-aft moments peak around rated wind speed. For the extreme blade root edge moment it is seen that the loads peak around rated wind speed for both simulation sets, but the main difference is that after 16 m/s the DLC 1.3 loads and the scatter increases with wind speed.

Table 3 lists the overall characteristic loads from each simulation set (the extremes seen in Figure 9), together with their ratio. The difference between the overall extremes from the two simulation sets is largest for the tower-top yaw moment, where the extremes are lower from the constrained simulations. The overall extremes are of similar magnitude for the tower base fore-aft moment and the blade root flap-wise moment.

5.2 Time series of turbine loads

In the following, examples of 10-minute time series from DLC 1.3 and constrained simulation sets are shown side by side, for comparison and demonstration of the differences in the wind turbine response to different types of wind regime. A comparison is made for the tower-base fore-aft moment, where the characteristic extreme loads from the different simulation sets are of similar magnitude. We also consider and compare the tower top tilt- and yaw-moments, which give the largest differences between the two simulation sets.

First, we compare two time series giving some of the highest extreme tower base fore-aft moments from each simulation set. For DLC 1.3 in Figure 10 the mean u-component hub-height wind speed is $U = 12.0$ m/s, with standard deviation of $\sigma_u = 2.7$ m/s and the peak tower base fore-aft moment is 236000 kNm. For the constrained simulation, $U = 14.9$ m/s and $\sigma_u = 3.5$ m/s. The peak tower base fore-aft moment is 228000 kNm. The peak tower base fore-aft moments are of similar magnitude in the simulations, and in both cases this occurs when the pitch angle is zero degrees—right before the wind turbine blades begin to pitch. Also, at the time when the wind speed at hub height reaches rated wind speed, the wind speed at 179 m is above rated wind speed, leading to higher loading on the upper half of the rotor. From the turbulence simulations, the most noticeable difference in the wind turbine response is that in the constrained turbulence simulation the time of the peak tower base fore-aft moment is very distinguishable at 390 s. While for the stationary turbulence the peak response occurs around 150 s, but numerous times it reaches above 200000 kNm during the simulation. Note that the axes in the top panels are the same, as are the axes in the bottom panels. It is seen that although the standard deviation of the wind speed is lower in the stationary turbulence

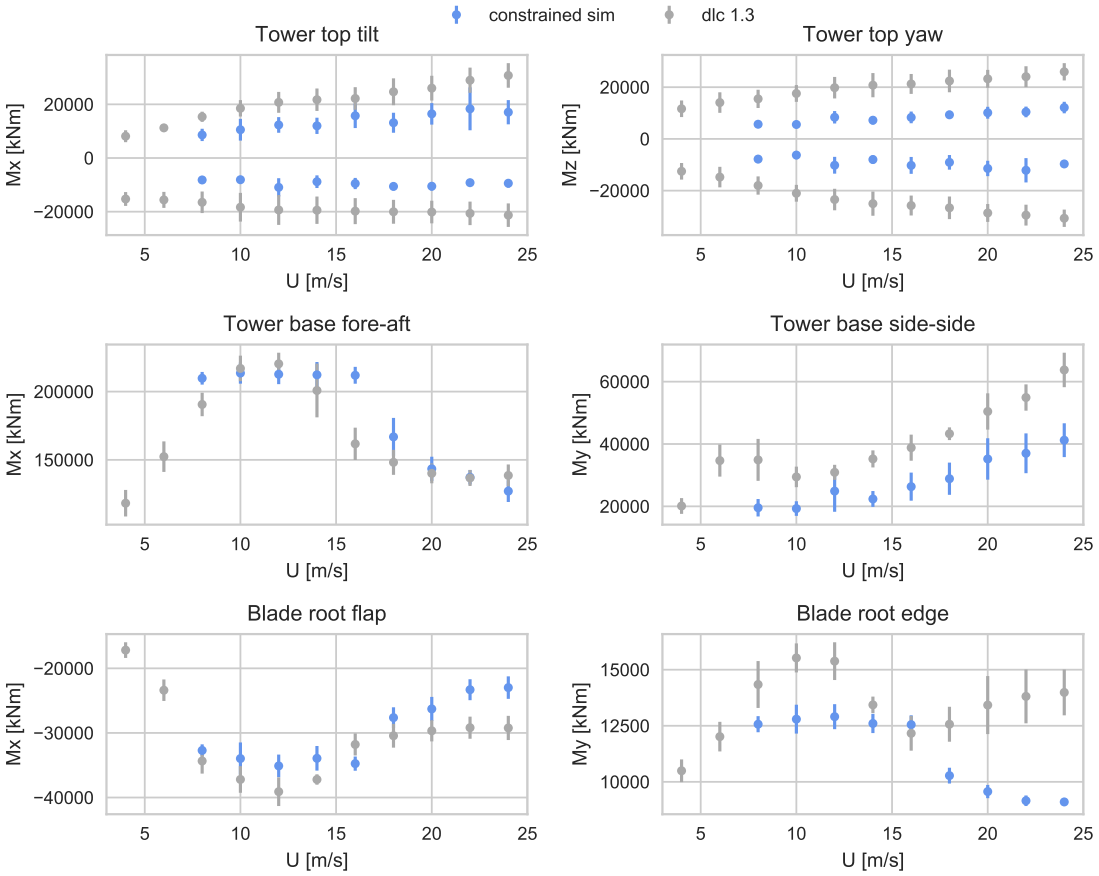

Figure 9. The mean extreme moments from IEC DLC 1.3 (grey dots). The mean extreme loads from the constrained simulations (blue dots).

Mean extreme moment	DLC 1.3 [kNm]	Constrained sim [kNm]	Ratio (Const./DLC)
Tower top tilt	$3.08 \cdot 10^4$	$1.83 \cdot 10^4$	0.60
Tower top yaw	$-3.07 \cdot 10^4$	$-1.21 \cdot 10^4$	0.40
Tower base fore-aft	$2.20 \cdot 10^5$	$2.14 \cdot 10^5$	0.97
Tower base side-side	$6.38 \cdot 10^4$	$4.12 \cdot 10^4$	0.65
Blade root flap	$-3.91 \cdot 10^4$	$-3.51 \cdot 10^4$	0.90
Blade root edge	$1.55 \cdot 10^4$	$1.29 \cdot 10^4$	0.83

Table 3. The highest mean extreme moments for different load components

simulation, the wind speed extremes are greater, with instantaneous wind speed reaching below 2 m/s and above 22 m/s.

In Figure 11 we compare some of the most extreme tower top moments from the two simulation sets. The stationary turbulence simulation in Figure 11, has $U = 22\,\text{m/s}$, $\sigma_u = 3.4\,\text{m/s}$, with a peak tower top tilt moment of 36601 kNm and a peak tower top yaw moment of $-28900\,\text{kNm}$; in contrast the constrained turbulence simulation has $U = 21.3\,\text{m/s}$, $\sigma_u = 6.6\,\text{m/s}$, with a peak tower top tilt moment of 30800 kNm and a peak tower top yaw moment of $-18600\,\text{kNm}$. As in the previous example, the time of peak loads is very clearly identified in the constrained turbulence simulation, and the peak value is significantly higher than the response for the remainder of the simulation. For the stationary turbulence simulation, the tower top yaw- and tilt moments often reach high values throughout the simulation. Extreme tower-top moments tend to be observed when there is high shear across the rotor. In stationary turbulent flow the variation in wind speed across the rotor arises as turbulent eddies sweep by, hitting only part of the rotor, leading to high wind shear. The extreme tower top loads from the constrained simulations are in connection with high vertical wind shear arising during the wind speed increase (ramp event).

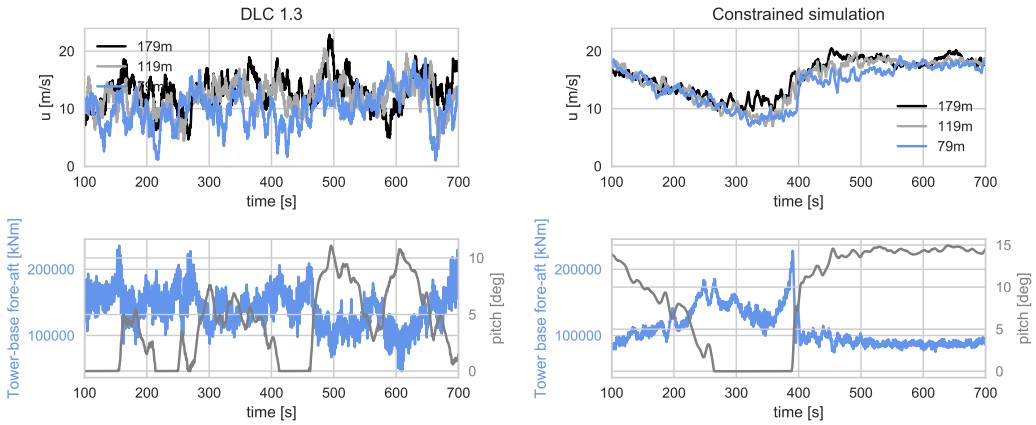

Figure 10. Comparison of a DLC 1.3 time series and a constrained simulation time series of an extreme variance event. *Top panels*: u-component wind speed. *Bottom panels*: Tower-base fore-aft moment (blue) and pitch angle (grey).

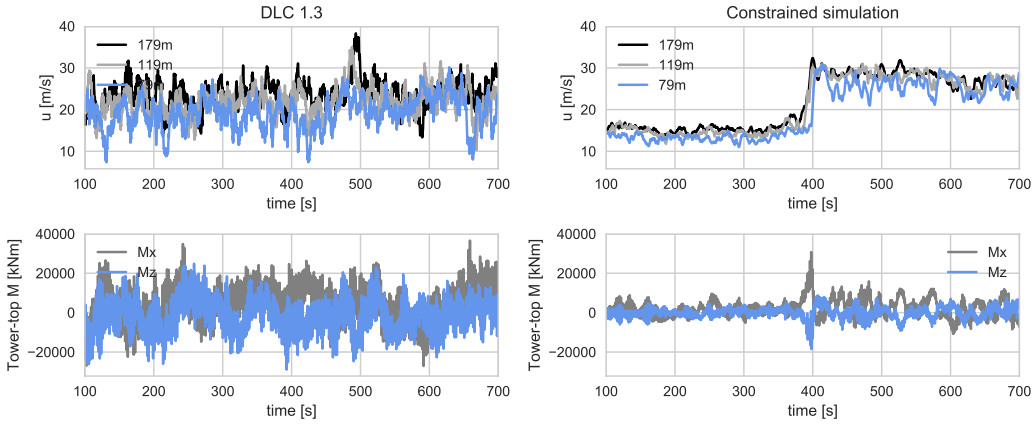

Figure 11. Comparison of a DLC 1.3 time series and a constrained simulation time series of an extreme variance event. *Top panels*: u-component wind speed. *Bottom panels*: Tower-top tilt (grey) and yaw (blue) moments.

6 Discussion

In the load time series comparison, the general differences in the wind turbine response of the two simulation sets are visualized; for the constrained simulations the peak loads are distinguishable and occur because of the velocity increase associated with the ramp-like event. The discrepancies between the two simulation sets for the extreme tower top loads indicate that the short-term wind field variability across the rotor is generally higher in the stationary turbulence simulation than for the constrained simulations. As shown in the time series comparison of Figure 11, the short-term vertical wind shear can be high in connection with the extreme events, yet the tower top tilt moment does not exceed that prescribed via DLC 1.3. When non-uniformity in the stationary turbulence fields occurs around rated wind speed, it can also lead to high extreme tower base fore-aft moments that are connected to high thrust on the rotor. The extreme tower base fore-aft moments from the constrained simulations are highest for mean wind speed bins between 8 m/s and 16 m/s. In this wind speed range, the wind speed is typically below rated wind speed at the beginning of the simulation and later increases beyond rated wind speed. When the wind speed starts to rise, it does so coherently across the rotor plane, resulting in high thrust and tower base fore-aft moments, before the wind turbine controller starts to pitch the blades. The tower base fore-aft moments for the extreme turbulence case (IEC DLC 1.3) were expected to be lower than those of the extreme variance events; however, this was generally true only (on average) for certain wind speed bins. The overall characteristic tower base fore-aft moment of DLC 1.3 is 3% higher than for the extreme events.

The load simulation results show that the extreme turbulence case DLC1.3 indeed covers the load envelope caused by extreme variance events. However, the differences seen in the time series and in the load behavior indicates that extreme

variance observations as events are entirely different from situations with stationary, homogeneous turbulence. This questions the basis for the definition of the IEC Extreme Turbulence Model (ETM) which is defined in terms of the statistics of the 10-minute standard deviation of wind speed. As most observations of the selected extreme variance events include a short term ramp event, it would perhaps be more relevant to compare these events with other extreme design load cases in the IEC standard, e.g. the extreme coherent gust with direction change, extreme wind shear or the extreme operating gust. Since these are the absolute highest variance events observed at Høvsøre during a ten year period, they would also appear in the site-specific definition of the ETM model. Therefore, it may be necessary to exclude or re-assign such events to the relevant load case type. The design and cost of a wind turbine may depend on how this consideration is done.

It was seen in the IFORM analysis in section 3.1 that the estimated 50-year return period contour of the linearly detrended data exceeded the 50-year return period contour of normal turbulence (corresponding to the ETM class C). This is consistent with the findings of Dimitrov et al. (2017), who performed similar analysis of linearly detrended measurements from Høvsøre, though from the easterly (homogeneous farmland) sector. For the high-pass filtered measurements, the turbulence level was reduced significantly as well as the estimated 50-year return period of turbulence. This is seen as the high-pass filtering effectively removes variance of low frequency fluctuations with time scales larges than 300 s, as the chosen cut-off frequency was 1/300 Hz. This finding suggests that for typical hub heights as considered ($z \approx 100$ m) at a coastal site like Høvsøre, extreme variance events are not representative of homogeneous, stationary turbulence and can be filtered out by high-pass filtering. It should be kept in mind though, that these events may be considered for extreme design load case purposes other than turbulence. In that case it is important not to use detrending of any kind on the measurements, as these extreme fluctuations will then not be identified and characterized correctly.

7 Conclusions

The main objective of this study is to investigate how extreme variance events influence wind turbine response and how it compares with DLC 1.3 of the IEC 61400-1 standard. The selected extreme events are measurements of the 10-minute standard deviation of horizontal wind speed that exceed the values prescribed by the ETM model and include a sudden velocity jump (ramp event, transients in the turbulent flow), which is the main cause of the high observed variance. The events were simulated with constrained turbulence simulations, where the measured time series were incorporated in turbulence boxes for load simulations in order to make a realistic representation of the events, including the short term ramps and the coherent flow in the lateral direction as was seen in the comparison of measurements between the two masts in Figure 2. The constraints force the turbulent flow of the simulations to be non-stationary and non-homogeneous.

Load calculations of the simulated extreme events were made in HAWC2 and compared to load calculations with stationary homogeneous turbulence according to DLC 1.3. To summarize, we have found that:

- The extreme variance events are large coherent structures, observed simultaneously at two different masts with a 400 m (lateral) separation.
- Most extreme variance events include a sharp wind speed increase (short-time ramp) which is the main source of the large observed variance.
- High-pass filtering with a cut-off frequency of 1/300 Hz removes most of the variance corresponding to these ramp-like events, to the extent that the estimated 50-year return period of (remaining) turbulence level is lower than that of IEC ETM class C; linear de-trending may remove some of the variance but is not necessarily adequate.
- Compared with the DLC 1.3 of the IEC standard, the extreme loads are on average lower for the extreme variance events in the coastal/offshore climate and heights considered.
- For 10-minute mean wind speeds of 8–16 m/s, the events typically begin below rated wind speed and increase beyond, leading to high thrust on the rotor; such events lead to high extreme tower-base fore-aft loads which can exceed the DLC 1.3 prescription of the IEC standard.

Future related work includes further analysis and characterization of extreme variance events. In particular, ongoing work involves extreme short-term shear associated with such events, and directional change. Load simulations of the events may be compared with other extreme DLC's from the IEC standard.

Appendix A

The Figure in this appendix is equivalent to Figure 4, but shows the processed measurements.

Comparing the raw data in Figure 4, to the linearly detrended data and high-pass filtered data in Figure A1 it is seen that the detrending, and high pass filtering slightly lowers the values of μ_{σ_u}, while the reduction of σ_{σ_u} is much greater, especially for the high-pass filtered measurements.

Appendix B

Figure B1 shows extreme moments as function of the u-component of the mean hub-height wind speed. Each dot shows the maximum/minimum load value of each 10-minute HAWC2 simulation for the tower top (top panels), the tower base (middle panels) and blade root (bottom panels). The simulations based on a particular extreme variance event may be identified as a cluster of six dots, as they have been simulated with six different turbulence seeds. For DLC 1.3 a cluster of six dots may be seen, as the simulations are performed with six turbulence seeds per mean wind speed step. Figure 9 shows the values from Figure B1, binned and averaged.

Author contributions. ÁH performed the data analysis and simulations. ÁH made all figures. MK provided guidance and comments. ND developed the code that is used to perform constrained turbulence simulations. ÁH prepared the manuscript with contributions from the co-authors. This work is part of ÁH's PhD under supervision of MK.

Competing interests. The authors declare that no competing interests are present in this work.

Acknowledgements. The authors would like to thank Anand Natarajan and Jakob Mann for constructive comments and discussion. ÁH would also like to acknowledge Jenni Rinker and David Verelst for HAWC2 assistance.

References

Bak, C., Zahle, F., Bitsche, R., Kim, T., Yde, A., Henriksen, L. C., Natarajan, A., and Hansen, M.: Description of the DTU 10 MW Reference Wind Turbine, Tech. rep., DTU Wind Energy, 2013.

Berg, J., Natarajan, A., Mann, J., and G. Patton, E.: Gaussian vs non-Gaussian turbulence: Impact on wind turbine loads, Wind Energy, 19, 1975–1989, 2016.

Butterworth, S.: On the Theory of Filter Amplifiers, Experimental Wireless and the Wireless Engineer, 7, 536–541, 1930.

Chougule, A., Mann, J., Segalini, A., and Dellwik, E.: Spectral tensor parameters for wind turbine load modeling from forested and agricultural landscapes, Wind Energy, 18, 469–481, doi:10.1002/we.1709, 2015.

Chougule, A. S., Mann, J., Kelly, M., and Larsen, G. C.: Modeling Atmospheric Turbulence via Rapid Distortion Theory: Spectral Tensor of Velocity and Buoyancy, Journal of the Atmospheric Sciences, 74, 949–974, doi:10.1175/JAS-D-16-0215.1, 2017.

de Mare, M. T. and Mann, J.: On the Space-Time Structure of Sheared Turbulence, Boundary-layer Meteorology, 160, 453–474, doi:10.1007/s10546-016-0143-z, 2016.

Dimitrov, N. and Natarajan, A.: Application of simulated lidar scanning patterns to constrained Gaussian turbulence fields, Wind Energy, 20, 79–95, doi:10.1002/we.1992, 2017.

Dimitrov, N., Natarajan, A., and Mann, J.: Effects of normal and extreme turbulence spectral parameters on wind turbine loads, Renewable Energy, 101, 1180–1193, doi:10.1016/j.renene.2016.10.001, 2017.

Fesquet, C., Drobinski, P., Barthlott, C., and Dubos, T.: Impact of terrain heterogeneity on near-surface turbulence structure, Atmospheric Research, 94, 254 – 269, doi:https://doi.org/10.1016/j.atmosres.2009.06.003, http://www.sciencedirect.com/science/article/pii/S0169809509001665, 2009.

Fitzwater, L., Cornell, A., and Veers, P.: Using Environmental Contours to Predict Extreme Events on Wind Turbines, in: ASME proceedings, ASME 2003 Wind Energy Symposium, p. 244–258, 2003.

Foster, R. C.: Why Rolls are Prevalent in the Hurricane Boundary Layer, Journal of the Atmospheric Sciences, 62, 2647–2661, doi:10.1175/JAS3475.1, https://doi.org/10.1175/JAS3475.1, 2005.

Foster, R. C., Vianey, F., Drobinski, P., and Carlotti, P.: Near-Surface Coherent Structures and The Vertical Momentum Flux in a Large-Eddy Simulation of the Neutrally-Stratified Boundary Layer, Boundary-Layer Meteorology, 120, 229–255, doi:10.1007/s10546-006-9054-8, https://doi.org/10.1007/s10546-006-9054-8, 2006.

Hansen, M. H. and Henriksen, L. C.: Basic DTU Wind Energy controller, Tech. rep., DTU Wind Energy, Denmark, contract Number: EUDP project Light Rotor; Project Number 46-43028-Xwp3 The report number is DTU- Wind-Energy-Report-E-0028 and not DTU-Wind-Energy-Report-E-0018 as stated inside the report, 2013.

Hansen, M. H., Thomsen, K., Natarajan, A., and Barlas, A.: Design Load Basis for onshore turbines - Revision 00, Tech. rep., DTU Wind Energy, 2015.

Hansen, M. O. L.: Aerodynamics of Wind Turbines, 2nd edition, Routledge, 2013.

Hoffman, Y. and Ribak, E.: Constrained realizations of Gaussian fields - A simple algorithm, Astrophysical Journal, 380, L5–L8, doi:10.1086/186160, 1991.

IEC: IEC 61400-1 Wind turbines - Part 1: Design requirements,3rd edn., Standard, International Electrotechnical Commission, Geneva, Switserland, 2005.

Kelly, M.: From standard wind measurements to spectral characterization: turbulence length scale and distribution, Wind Energy Science, pp. xxx–yyy, 2018.

Kristensen, L. and Frandsen, S. T.: Model for Power Spectra of the Blade of a Wind Turbine Measured from the Moving Frame of Reference, Journal of Wind Engineering & Industrial Aerodynamics, 10, 249–262, doi:10.1016/0167-6105(82)90067-8, 1982.

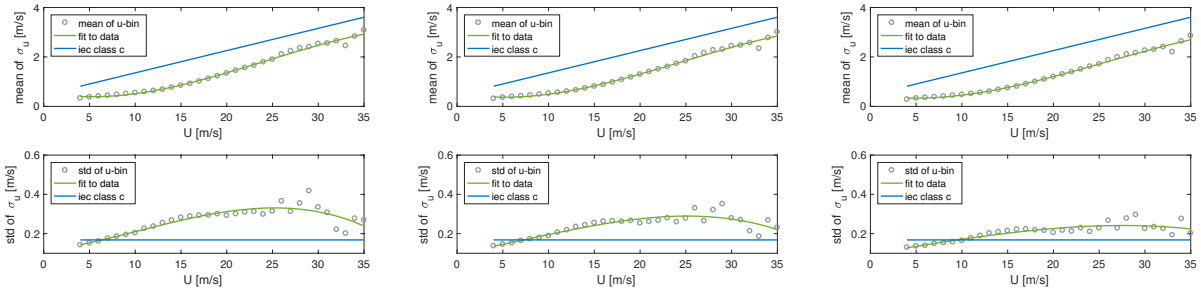

Figure A1. Notation same as Figure 4 but for a) linearly detrended data, b) high-pass filtered data with cut-off frequency of 1/600 Hz and c) high-pass filtered data with cut-off frequency of 1/300 Hz.

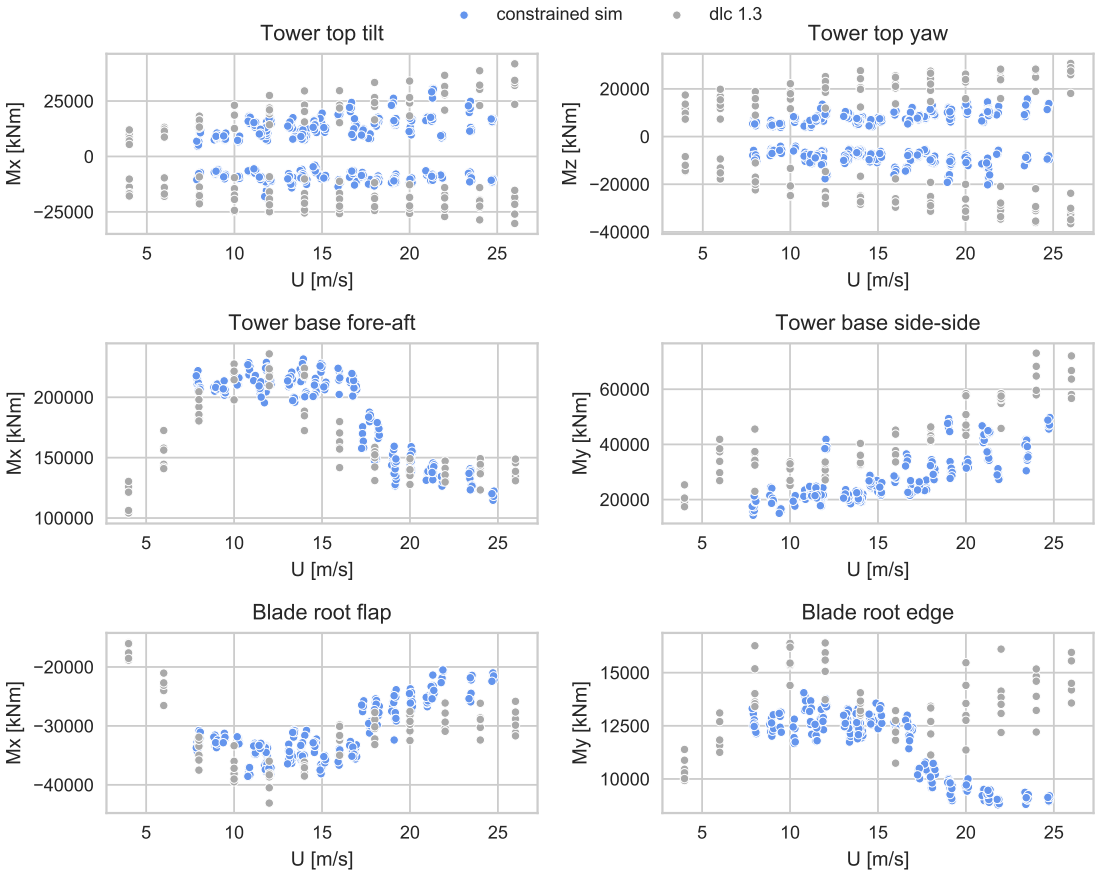

Figure B1. The extreme moments from IEC DLC 1.3 (grey dots). The extreme loads from the constrained simulations (blue dots).

Larsen, T. J. and Hansen, A. M.: How 2 HAWC2, the user's manual, Tech. rep., DTU Wind Energy, 2015.

Mann, J.: The spatial structure of neutral atmospheric surface-layer turbulence, Journal of Fluid Mechanics, 273, 141–168, 1994.

Mann, J.: Wind field simulation, Probabilistic Engineering Mechanics, 13, 269–282, 1998.

Moon, J. S., Sahasakkul, W., Soni, M., and Manuel, L.: On the Use of Site Data to Define Extreme Turbulence Conditions for Wind Turbine Design, Journal of Solar Energy Engineering, 136, 2014.

Nielsen, M., Larsen, G., Mann, J., Ott, S., Hansen, K., and Pedersen, B.: Wind Simulation for Extreme and Fatigue Loads, Tech. rep., Risø National Laboratory, Roskilde, Denmark, 2004.

Peña Diaz, A., Floors, R. R., Sathe, A., Gryning, S.-E., Wagner, R., Courtney, M., Larsén, X. G., Hahmann, A. N., and Hasager,

C. B.: Ten Years of Boundary-Layer and Wind-Power Meteorology at Høvsøre, Denmark, Boundary-layer Meteorology, 158, 1–26, doi:10.1007/s10546-015-0079-8, 2016.

Rosenblatt, M.: Remarks on a Multivariate Transformation, The Annals of Mathematical Statistics, 23, 470–472, doi:10.1214/aoms/1177729394, https://doi.org/10.1214/aoms/1177729394, 1952.

Saranyasoontorn, K. and Manuel, L.: Design Loads for Wind Turbines Using the Environmental Contour Method, Journal of Solar Energy Engineering, 128, 554, 2006.

Sathe, A., Mann, J., Barlas, T. K., Bierbooms, W., and van Bussel, G.: Influence of atmospheric stability on wind turbine loads, Wind Energy, 16, 1013–1032, doi:10.1002/we.1528, 2013.

Vincent, C.: Mesoscale wind fluctuations over Danish waters, Ph.D. thesis, DTU Wind Energy, 2010.

Vincent, C., Hahmann, A., and Kelly, M.: Idealized Mesoscale Model Simulations of Open Cellular Convection Over the Sea, Boundary-Layer Meteorology, 142, 103–121, doi:10.1007/s10546-011-9664-7, 2012.

Winterstein, S. R., Ude, T. C., Cornell, C. A., Bjerager, P., and Haver, S.: Environmental parameters for extreme response: inverse FORM with omission factors, in: Proceedings of the 6th international conference on structural safety and reliability (ICOSSAR'93), p. 551–557, 1993.

CHAPTER 4
Characterization of wind speed ramps

The extreme fluctuations from the previous chapter are investigated further. Three measurement sites and a larger number of events are included in the study where characterizations of amplitude and rise time are made. With the corresponding direction change, the extreme events are compared with the extreme coherent gust with direction change of the IEC standard. The paper in this chapter has been submitted to a journal.

Detection and characterization of extreme wind speed ramps

Ásta Hannesdóttir and Mark Kelly
DTU Wind Energy Dept., Technical University of Denmark, Roskilde, Denmark
Correspondence: astah@dtu.dk

Abstract. The present study introduces a new method to characterize ramp-like wind speed fluctuations, including coherent gusts. This method combines two well-known methods: the continuous wavelet transform and the fitting of an idealized ramp function. The method provides estimation of ramp amplitude and rise time, and is herein used to statistically characterize ramp-like fluctuations at three different measurements sites. Together with corresponding amplitude of wind direction change, the ramp amplitude and rise time variables are compared to the extreme coherent gust with direction change from the IEC wind turbine safety standard. From the comparison we find that the observed amplitudes of the estimated fluctuations do not exceed the one prescribed in the standard, but the rise time is generally much longer, on average around 200 s. The direction change does however exceed the one prescribed in the standard several times, but for those events the rise time is on the order of minutes. We also demonstrate a general pattern in the statistical behavior of the characteristic ramp variables, noting their wind speed dependence, or lack thereof, at the different sites.

1 Introduction

The IEC wind turbine safety standard prescribes various models of extreme wind conditions that a wind turbine must withstand during its operational lifetime (IEC, 2005). One of those prescribed models is an extreme coherent gust with direction change (ECD), used for ultimate load prediction. The ECD model is presented in Stork et al. (1998), but with a rather limited description; the model is not shown compared to measurements, but it is said to represent extreme gusts and direction changes of wind speed measurements 'quite well.' However, the ECD prescription was found later by Hansen and Larsen (2007) to give reasonable estimates compared with measurements.

With the increasing rotor size of modern wind turbines, resent research has focused on how the gust models in the IEC standard are unrealistically represented by a uniform wave (Bierbooms, 2005; Bos et al., 2014). In these studies, gusts are defined as extreme fluctuations of stationary and homogeneous turbulence. The gusts are simulated with stochastic simulations and constrained in space to have a finite length scale. Using such gust models for wind turbine load simulations generally results in lower loads than when using the uniform gust models of the IEC standard. The reason is due to the limited length scale of the gusts, and that during the simulations some gust might even miss the blades as they sweep by the rotor. The authors of these studies suggest that the uniform gust models of the IEC standard should consequently be replaced by stochastic gust models.

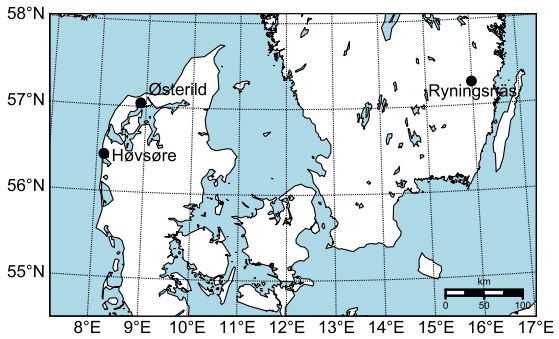

Figure 1. A Map of Denmark and southern Sweden showing the locations of the measurement sites.

There are however many studies in the field of atmospheric science that investigate large coherent structures in turbulent flow (e.g. Mahrt, 1991; Belušić and Mahrt, 2012; Barthlott et al., 2007; Fesquet et al., 2009). These studies take into consideration fluctuations of larger scales than those of stationary, homogeneous turbulence, i.e. the submesoscale or mesoscale. These coherent structures are seen in measurements as ramp-like increases in wind speed, that may readily be compared with the ECD due to similar characteristics. The coherent structures can be driven by a broad range of different meteorological processes. In the stable boundary layer they may be generated by e.g. gravity waves, Kelvin-Helmholtz instabilities, surface heterogeneity or pressure disturbances (Mahrt, 2010). In the convective boundary layer they may be generated by e.g. surface buoyancy fluxes, latent heat release or cloud radiative effects and may be observed in form of convective cells and rolls (Drobinski et al., 1998; Young et al., 2002). In the neutral boundary layer they may be generated by shear and can be observed in the form of streaks (Foster et al., 2006). Some processes are bound to certain terrain, e.g coherent structures may be generated by dynamics between the flow and plant canopy (Finnigan, 2000), or in coastal and offshore regions they may be driven by open cellular convection (e.g. Vincent et al., 2012).

In this study we focus on large-scale, high-amplitude (extreme) fluctuations, which are coherent across the rotor of any multi-megawatt wind turbine. We examine data from three sites with different terrain types and characterize the fluctuations. We investigate if the characteristics of the fluctuation are comparable with the ECD. In order to characterize the amplitude and rise-time of the investigated fluctuations we provide a new combination of two well-known methods: the continuous wavelet transform and the fitting of an idealized ramp function, which is inspired by detection of atmospheric boundary-layer depth (Steyn et al., 1999).

2 Sites and measurements

The measurements used for the characterization of the ramp-like events come from three different sites. The locations of the measurement sites may be seen in Figure 1.

2.1 Høvsøre

The Høvsøre National Test Centre for Wind Turbines is located at the west coast of Jutland, approximately 1.7 km east of the coastline. The site is at a coastal agricultural area where the terrain is nearly flat. Several masts with measurement instruments are located at the site, that has been in operation since 2004. In the current analysis we use measurements from a light mast with cup anemometers and wind vanes installed at 60 m, 100 m and 160 m height. The light mast is located between two of the test wind turbines which are separated by approximately 300 m in the North-South direction. The dominating wind direction is from north-west and the annual average 10-minute wind speed at the light mast is V_{ave} = 9.33 m/s at 100 m and the reference turbulence intensity is $I_{\text{ref}} = 0.065$ [1]. The data used in this study consists of 10 Hz measurements from September 2004 to December 2014. A detailed overview on the site and instrumentation may be found in Peña et al. (2016).

2.2 Østerild

The Østerild National Test Centre for Large Wind Turbines is located in a forested area in Northern Jutland. The distance to the coast is approximately 4 km to the north and 20 km to the west. The site has two 250 m tall light masts equipped with sonic anemometers at 37 m, 103 m, 175 m and 241 m. In this analysis we use measurements from the southern mast, where the terrain around the mast is flat and the surrounding forest has canopy height between 10 and 20 m. To the west of the mast there is a narrow clearing of the forest with a grass field. The clearing is approximately 1 km long in the east-west direction and 200 m wide in the north-south direction. The mast is located approximately 300 m South-west of a row of seven wind turbines aligned in the north-south direction. At the southern light mast, the annual average 10-minute wind speed is V_{ave} = 7.94 m/s at 103 m height and the reference turbulence intensity is I_{ref} = 0.13. The data used in this study consists of 20 Hz measurements from March 2015 to February 2018 at 37 m, 103 m and 175 m heights. More details on the site may be found in Hansen et al. (2014).

2.3 Ryningsnäs

The Ryningsnäs measurement site is located approximately 30 km inland from the south-eastern coast of Sweden. The terrain is forested and generally flat. The forest has a 200 km fetch in the west direction and the tree height around the site is between 20 and 25 m. There is a 138 m tall meteorological mast equipped with sonic anemometers at 40 m, 59 m, 80 m, 98 m, 120 m and 138 m measuring at 20 Hz sampling frequency. In this analysis we use the measurements at 59 m, 98 m and 138 m height from a period between November 2010 and December 2011. There are two wind turbines approximately 200 m from the mast, one in the south direction and the other in the north-east direction. The annual average 10-minute wind speed is V_{ave} = 5.94 m/s at 98 m height and the reference turbulence intensity is I_{ref} = 0.18. More details on the site and measurements may be found in Arnqvist et al. (2015).

[1] I_{ref}: The average 10-minute turbulence intensity evaluated at wind speed of 15 m/s

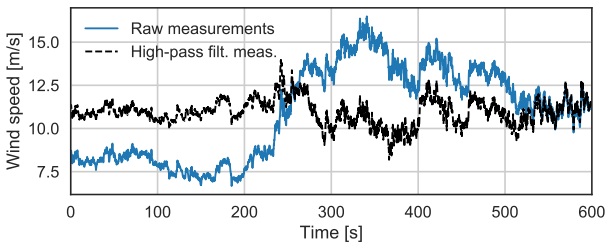

Figure 2. Wind speed measurements from 100 m at Høvsøre, raw measurements (blue line) and high-pass filtered measurements (dashed black line).

3 Selection and characterization of events

In this section we go through the steps of selecting and characterizing the ramp-like coherent structures. There are three steps in the procedure:

1. Identify events of extreme variance, indicating large scale fluctuations, and acquire 30-minute wind speed measurements for each event.
2. Estimate the time scale and position in time (timing) of the dominating fluctuation using wavelet transform.
3. Characterize the amplitude and rise time of the dominating fluctuation by fitting an idealized ramp function to a subset of the wind speed signal, which timing and scale are found by the wavelet transform.

3.1 First step: Selecting high variance events

Here we select the ramp events by comparing two different data sets. One where the 10-minute standard deviation is calculated from the raw measurements, σ_{raw} and the other where the measurements have been high-pass filtered σ_{filt}. A significant reduction in the 10-minute standard deviation by high-pass filtering indicates that the measurements include a ramp-like fluctuation. This fluctuation then gives rise to the high observed standard deviation (Hannesdóttir et al., 2018).

The filtering is performed with a second order Butterworth filter where the cut-off frequency is chosen as:

$$f_c = \frac{U}{L} \tag{1}$$

where U is the ten-minute mean wind speed and L is a length scale, here chosen to be 2000 m. With this choice of cut-off frequency the filtered measurements do not include any trends or fluctuations involved with length scales larger than 2000 m.

In order to identify where the 10-minute standard deviation is reduced the most by filtering, we calculate the ratios of $\sigma_{\text{raw}}/(\sigma_{\text{filt}}+1)$ and identify the highest 0.1% from each data set[2]. We then acquire 30-minute samples of high frequency

[2]Here σ_{filt} is shifted by one to put emphasis on high σ values. Otherwise only ratios where $\sigma_{\text{filt}} << 1$ are selected.

measurements for each event for further analysis and characterization. By using 30-minute samples we ensure that we have enough measurements before and/or after the ramp-like wind speed increase.

An example of an extreme-variance event may be seen in Figure 2, where 10-minute 'raw' wind speed measurements are compared with filtered measurements. This example is taken from the light mast in Høvsøre at 100 m. The 10-minute standard deviation of the raw measurements is 2.66 m/s, but 0.75 m/s for the filtered measurements.

3.2 Second step: Wavelet transform

The continuous wavelet transform (CWT) unfolds a signal in both frequency and time and provides an efficient way to identify and localize abrupt changes or transients in non-stationary time series. The CWT is often used to identify and characterize coherent structures in turbulent flow (e.g. Dunyak et al., 1998; Krusche and de Oliveira, 2004; Fesquet et al., 2009), or wind power ramps (Gallego et al., 2013).

The CWT is formally defined as the inner product of a function $x(t)$ and a mother wavelet $\psi(t)$ that is shifted and dilated

$$W_x(\ell, t') = \frac{1}{\ell} \int_{-\infty}^{\infty} x(t) \psi \left(\frac{t - t'}{\ell} \right) dt \tag{2}$$

where the resulting wavelet coefficients W_x are a function of the scale dilation ℓ and time shift t'. Note that the factor $1/\ell$ is a normalization resulting in wavelet coefficients in the L^1-norm, though this normalization is most commonly seen in the literature as $1/\sqrt{\ell}$ giving a CWT in the L^2-norm (Farge, 1992). However it is important when comparing wavelet coefficients (or wavelet power spectrum) between different scales to do so in the L^1-norm, to prevent giving a bias toward the large scales (Liu et al., 2007).

The choice of analyzing wavelet influences the results of the wavelet transform, since it reflects characteristics of the wavelet. We have therefore chosen a wavelet that includes features similar to those we look for in the signal, i.e. one dominating increase at the center of the wavelet function. The analyzing wavelet chosen here is the first derivative of a Gaussian (DOG1) wavelet[3]

$$\psi(t) = C\, t \mathrm{e}^{-t^2} \tag{3}$$

where C is a normalization constant, here equal to: $2(2/\pi)^{1/4}$. Note that we have switched the sign of the wavelet to get positive wavelet coefficients from the transform where there is an increase in the wind speed signal (Figure 3 (b)).

Figure 3 shows an example of a CWT of one of the detected high-variance events along with the mirrored DOG1 wavelet. The highest wavelet coefficients are shown with red, indicating a high correlation between the signal and the wavelet at that given time. The maximum wavelet coefficient of the CWT identifies the timing (t') and the scale (ℓ) of the coherent structure.

3.3 Third step: Idealized ramp function

The definition of the idealized ramp function is borrowed from Steyn et al. (1999), where they incorporate the error function into an idealized backscatter profile. The profile is fit to backscatter lidar measurements to identify the depth of the atmospheric

[3]The wavelet transform is performed using the Python package PyWavelets (Lee et al., 2006–)

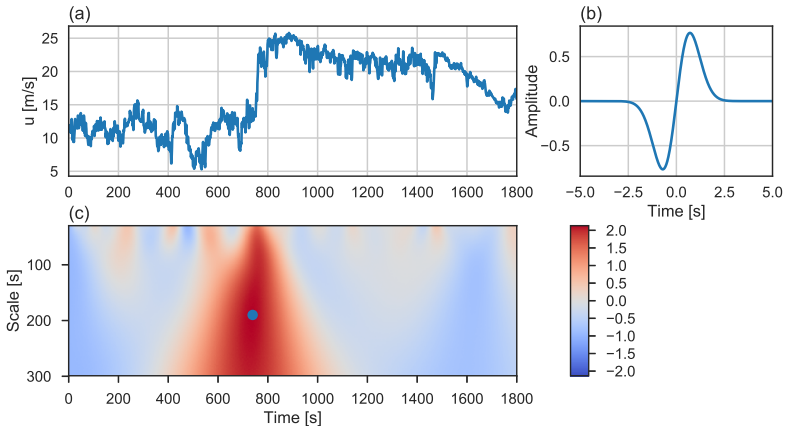

Figure 3. The continuous wavelet transform of a ramp-like coherent structure. (a): 10-minute wind speed signal at 100 m, Høvsøre. (b): The flipped DOG1 wavelet used for the wavelet transform. (c): The wavelet coefficients of the wind speed signal. The maximum coefficient is shown with a blue dot at $\ell = 190\,s$ and $\tau = 739\,s$

boundary (mixed) layer, and the thickness of the entrainment zone. Wind speed measurements where the wind speed rapidly increases may often resemble these ideal backscatter profiles, and therefore we can use this method to characterize ramp-like fluctuations in the same manner. The idealized ramp wind speed function, may be defined as:

$$u(t) = \frac{u_b + u_a}{2} - \frac{u_b - u_a}{2}\mathrm{erf}\left(\frac{t - t'}{\tau}\right) \tag{4}$$

where u_b is the wind speed before the rise, u_a is the wind speed after the rise and τ is a normalization constant. We define the rise time of the ramp from the interval where the wind speed rises from $0.025u_b$ to $0.975u_a$. This value may be estimated by multiplying τ with 3.17, which is found from ordinates of the error function. The parameters of the idealized ramp function are found by minimizing the least square differences between the measurements and the ramp function with an optimization curve fitting procedure[4].

Figure 4 demonstrates the idealized ramp function that is fit to wind speed measurements from the different sites. The limited period that the ramp function is fit to is found by the CWT. The timing is given by t' and the period is three times the scale: $3 \cdot \ell$. The factor of three is used to ensure approximately equal periods of measurements before, during, and after the ramp-like increase for the curve fitting procedure.

3.4 Overview of the selection and characterization

A brief summation of the detection: A subset of extreme variance events is found. The CWT is performed on each event and the timing and scale of the ramp-like wind speed increase is estimated. The scale (3ℓ) is used to find a limited period of the

[4]For the optimization fitting procedure we employed the SciPy curve_fit function

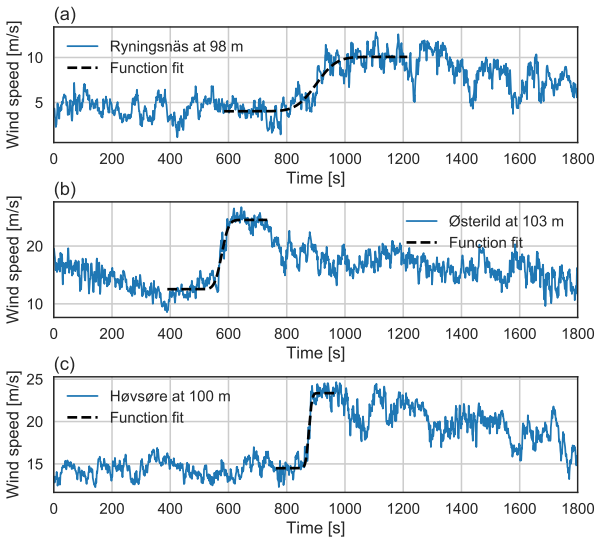

Figure 4. Three examples of the idealized ramp function fit to the wind speed measurements. Measurements from: (a) Ryningsnäs (b) Østerild (c) Høvsøre. The blue lines shows the measurements and the dashed black lines shows the idealized ramp function fit to a subset of the measurement.

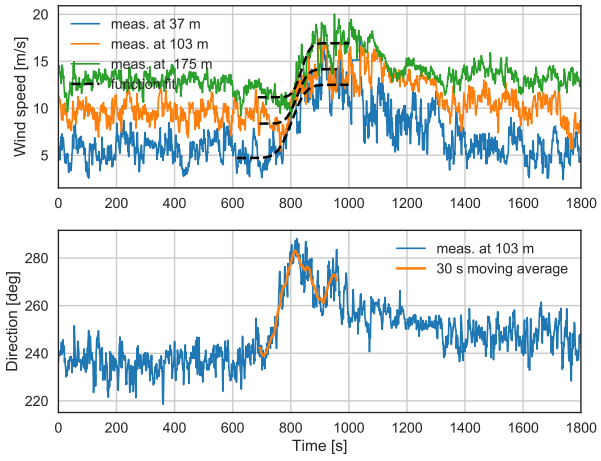

Figure 5. The idealized ramp function fit to Østerild measurements at three different heights and the corresponding direction change.

wind speed signal to which the idealized ramp function is fit. The idealized ramp function parameters are used to estimate the amplitude of the ramp-like fluctuation: $\Delta u = u_a - u_b$, and the rise time: $\Delta t = 3.17\tau$.

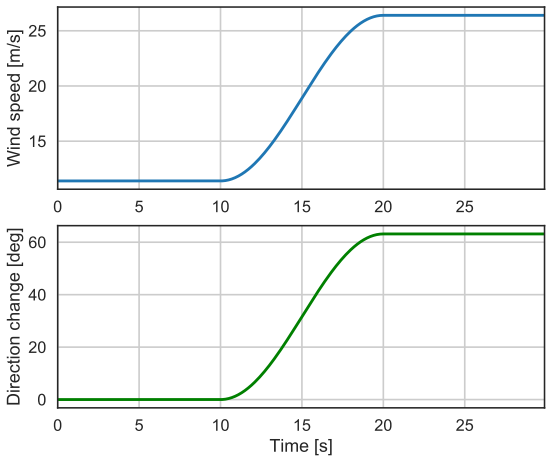

Figure 6. The extreme coherent gust with direction change from the IEC wind turbine safety standard.

As we want to compare the wind speed ramps with the ECD load case of the IEC standard, we investigate the direction change during the ramps. Here we use the directional data at ≈100 m from each site and calculate the moving 30 s average during the time of the ramp function at ≈100 m.

The direction change during the ramp-like wind speed increase is determined as the difference between the maximum value and the minimum value of the moving average.

An example of an ramp event at Østerild is shown in Figure 5 along with the corresponding directional data. The orange line in the lower panel shows the 30 s moving average during the ramp function period at 103 m. The moving average is applied to the directional measurements in order to filter out the small scale fluctuations that we do not want to influence the estimated direction change.

The amplitudes and rise times are characterized for each measurement height. Afterwards the values are averaged over the three different heights to give the characteristic rise time and amplitude for each event.

4 IEC extreme coherent gust with direction change

The extreme coherent gust with direction change (ECD) is modeled with an amplitude of $V_{cg} = 15\,\text{m/s}$ and a direction change

$$\theta_{cg} = \begin{cases} 180^\circ, & \text{if } V_{\text{hub}} \leq 4 \text{ m/s}. \\ 720^\circ\,\text{m/s}/V_{\text{hub}}, & \text{if } 4\,\text{m/s} < V_{\text{hub}} < V_{\text{ref}}, \end{cases} \tag{5}$$

where V_{hub} is the 10-minute mean wind speed at hub height and V_{ref} is the 10-minute mean reference wind speed. Both the direction change and wind speed change are modeled as functions of time,

$$\theta_{\text{cg}}(t) = \begin{cases} 0^\circ, & \text{if } t < 0 \\ \pm 0.5\theta_{\text{cg}}(1 - \cos(\pi t/T)), & \text{if } 0 \leq t \leq T \\ \pm\theta_{\text{cg}}, & \text{if } t > T \end{cases} \tag{6}$$

$$V(z,t) = \begin{cases} V(z), & \text{if } t < 0 \\ V(z) + 0.5V_{\text{cg}}(1 - \cos(\pi t/T)), & \text{if } 0 \leq t \leq T \\ V(z) + V_{\text{cg}}, & \text{if } t > T \end{cases} \tag{7}$$

where $T = 10\,s$ is the rise time. The direction change and wind speed increase are assumed to occur simultaneously. Figure 6 shows the ECD for $V_{\text{hub}} = V_r = 11.4\,m/s$ which is the rated wind speed for e.g. the NREL 5 MW- and the DTU 10 MW reference wind turbines (Jonkman et al., 2009; Bak et al., 2013). According to the IEC standard, the design load case with the ECD should be simulated at $V_r \pm 2$ m/s.

5 Distributions and comparison with the ECD

In this section we look at the amplitudes, rise times and direction change of the detected events and how these variables are distributed. Selecting the 0.1% highest ratios of $\sigma_{\text{raw}}/(\sigma_{\text{filt}} + 1)$ results in 453 events from Høvsøre, 154 from Østerild and 58 from Ryningsnäs. A number of these events are discarded before performing the characterization, for one of three reasons: because the measurements are partly missing; because the measurements are from a wind direction sector where the nearby wind turbines are upstream of the masts (in the wake of the wind turbines); or because the high observed variance is due to a wind speed decrease (negative ramps). The negative ramps are identified when the dominating wavelet coefficients are negative. The discarding narrows the number of analyzed events down to 216 from Høvsøre, 72 from Østerild and 32 from Ryningsnäs.

The estimated Δu, $\Delta\theta$ and Δt variables for each detected event and their distribution may be seen in Figure 7. The variables are shown with different colors for each measurement site, black for Høvsøre, blue for Østerild and green for Ryningsnäs. It may be seen that the highest values of each parameter are found from the Høvsøre data set, that has the longest measurement period.

The sample-means and the corresponding standard deviations of Δu, $\Delta\theta$ and Δt for each site may be found in Table 1. Though the variables are not normally distributed, we choose to show the standard deviation to indicate the spread of the variables. The average Δu and $\sigma_{\Delta u}$ are of similar magnitude for all sites. We see that the average ($\Delta\theta$) and standard deviation of direction change ($\sigma_{\Delta\theta}$) found in Ryningsnäs is nearly twice the value found at Østerild and significantly higher than at Høvsøre.

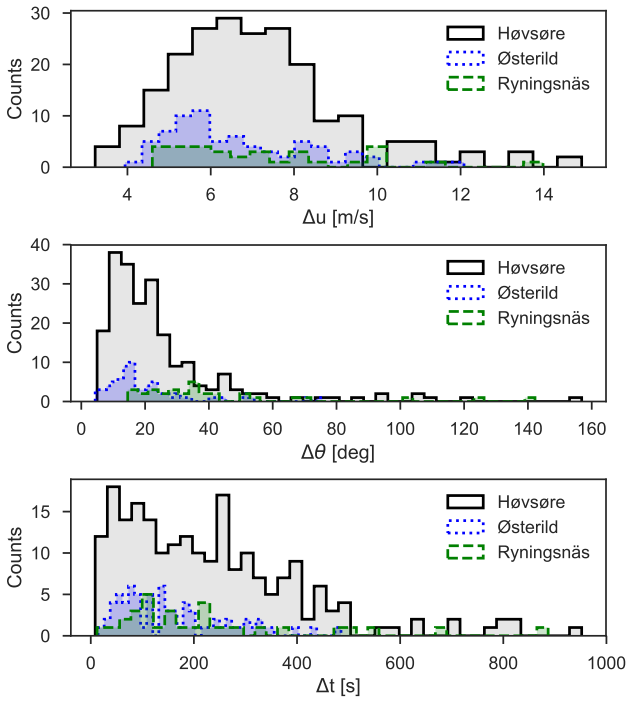

Figure 7. The distributions of detected amplitudes (Δu), direction changes ($\Delta\theta$) and rise times (Δt) of all the detected events at the three different sites: Høvsøre (grey), Østerild (blue) and Ryningsnäs (green).

	Høvsøre	Østerild	Ryningsnäs
Nr. of analyzed events	216	72	32
$\langle\Delta u\rangle \pm \sigma_{\Delta u}$	7.1± 2.1 m/s	6.7± 1.8 m/s	7.3± 2.2 m/s
$\langle\Delta\theta\rangle \pm \sigma_{\Delta\theta}$	25± 21°	21± 14°	42± 30°
$\langle\Delta t\rangle \pm \sigma_{\Delta t}$	232± 177 s	160± 105 s	233± 195 s

Table 1. The number of analyzed events and average estimated variables from each site.

The average Δt and $\sigma_{\Delta t}$ are lowest for the Østerild site, and there are no events detected with rise time above 485 s, while the maximum estimated rise time in Ryningsnäs and Høvsøre are 887 s and 952 s respectively.

Figure 8 shows the detected events as function of mean wind speed compared with the ECD model. The mean wind speed is the average of u_b and u_a, which may be taken as the representative wind speed of the events. A similar figure has been made showing the events as function of u_b, and may be found in Appendix A. The dashed lines show the IEC prescription of Δu, $\Delta\theta$ and Δt for the ECD. The solid lines show the variables averaged over wind speed bins where the bin width is 2 m/s. The shaded colors mark the area between the 10th percentile and the 90th percentile of the variables in each bin. When comparing the estimated Δu to the IEC prescribed amplitude, it is seen that there is not a single event that exceeds 15 m/s. There is a

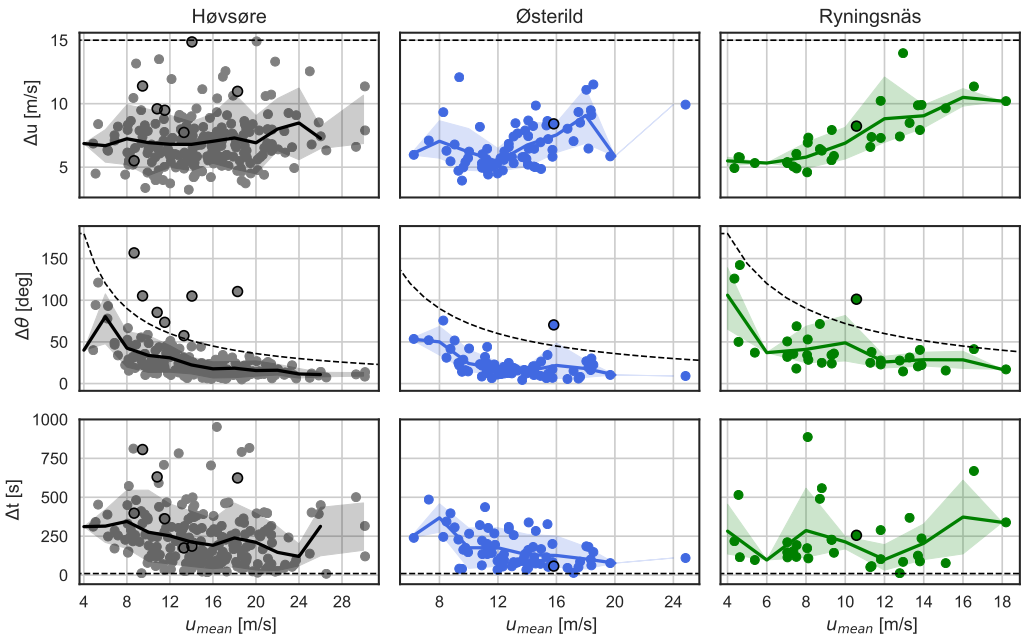

Figure 8. The detected amplitudes (Δu), direction changes ($\Delta\theta$) and rise times (Δt) as function of the mean wind speed at the different sites: Høvsøre (grey), Østerild (blue) and Ryningsnäs (green). The plots share the primary axis (abcissa) per column and they share the secondary axis (ordinate) per row. Shaded area indicates events between 10th percentile and 90th percentile for each wind speed bin, with bin width 2 m/s. The black dashed lines show the ECD values.

number of events that exceed the prescribed direction change of the ECD, one at Ryningsnäs, one at Østerild and seven at Høvsøre. These extreme direction events are indicated with a black circle in the different plots. The amplitude of the extreme direction events in Høvsøre ranges from $\Delta u = [5.5, 14, 9]$ m/s and the rise times range from $\Delta t = [174, 807]$ s. The extreme direction event at Østerild has a direction change of $\Delta\theta = 70°$, an amplitude of $\Delta u = 8.4$ m/s and a rise time of $\Delta t = 58$ s. At Ryningsnäs the extreme direction event has $\Delta\theta = 101°$, $\Delta u = 8.2$ m/s and $\Delta t = 256$ s.

6 Discussion

6.1 Discussion on the detection and characterization method

The CWT is ideal to find abrupt changes in a wind speed signal and can provide useful information on different scales of the flow. Here we use the wavelet transform to provide an objective estimate of the time scale of the ramp-like wind speed increase as well as the precise timing in the signal. To obtain characteristics of the amplitude and rise-time of these fluctuations we need an additional step, which is inspired by mixed layer height detection performed by fitting an idealized profile to backscatter measurements.

The main difference between backscatter profiles and wind speed time series, is that the wind speed continuously fluctuates through time and the period of the coherent structure we investigate is finite. This difference is why the wavelet analysis is important prior to the fitting of the idealized function, where the limited period of the ramp and the timing is identified. We found the optimal period for the fitting to be three times the scale dilation ($3 \cdot \ell$) of the DOG1 wavelet as defined in section 3.2. If this limited period is not long enough, the numerical curve fitting procedure might not always find an optimal solution to the fitting parameters. Having enough measurement points for a curve fitting procedure is what makes the method robust as pointed out by Steyn et al. (1999). However, for the purpose of characterizing wind speed fluctuations it is important that the chosen fitting period is not longer than necessary. We see e.g. for the wind speed fluctuations in Figure 4, that the wind speed decreases shortly after the ramp; if this decrease is included in the curve fitting, the amplitude of the estimated ramp would be underestimated. The choice of $3 \cdot \ell$, provides the shortest period that makes the combined method robust in the sense that it always results in a successful fit with an estimate of the desired parameters.

The first step in the selection, choosing high variance events, is used for two purposes: First, to ensure that the selected ramp-like fluctuations are associated with scales that are large enough to cover any rotor of a multi-megawatt wind turbine. We have seen in a previous study that these fluctuations occur approximately simultaneously at two different measurement masts in Høvsøre that are separated by 400 m transverse to the mean wind direction (Hannesdóttir et al., 2018). Second, by choosing a subset of events, we avoid performing a CWT on the whole data set of high frequency measurements, which is computationally demanding on a 10-year data set like the one from Høvsøre. If a CWT is performed on the whole data set an extra step would be needed in the analysis to decide whether a structure is coherent or not, e.g. to apply a threshold on the scale averaged wavelet coefficients or wavelet spectrum (e.g. Farge, 1992; Dunyak et al., 1998).

6.2 Discussion of observed distributions

The main difference between the observed fluctuations analyzed in the current study and the classic ECD (investigated in Stork et al., 1998; Hansen and Larsen, 2007), is that in the current study we only characterize large scale coherent structures, whereas the ECD is based on measurements where all extreme peaks of small-scale turbulence are considered. By extracting ramp events from the measurements, we exclude the small-scale fluctuations from the characterization of the amplitude and rise time (see Figures 4 and 5). Even though Hansen and Larsen (2007) only consider 10 s rise times from a data set with a two year period, they find gust amplitudes in a similar range as in the current study. This is because small-scale turbulent fluctuations can have very high peak values. However, such fluctuations are not coherent across rotor diameters of multi-megawatt wind turbines, and have much less impact than coherent ramps on loads for such turbines.

We observe that the average amplitudes of ramp-like fluctuations ($\langle \Delta u \rangle$) is of similar magnitude at all the sites considered. As shown in Fig. 8, Δu has negligible wind speed dependence at Høvsøre and Østerild, but at Ryningsnäs the ramp amplitudes increase with mean wind speed. The direction change generally decreases with wind speed at all the sites, but significantly larger mean change $\langle \Delta \theta \rangle$ is observed over ramps at Ryningsnäs. These observations are consistent with the (low-order, dominant) physics of the sites: Ryningsnäs has appreciably taller trees than Østerild, with the Ryningsnäs observations taken at roughly 2–5 times tree height; the measurements used from Østerild correspond to 5-15 times the respective tree heights there.

Thus the measurements at Ryningsnäs are more affected by the tree-induced turbulent stresses (e.g. Raupach et al., 1996; Sogachev and Kelly, 2016). In particular, a wind-speed (Reynolds-number) dependence arises in the turbulent degradation of the coherent structures, and there is more turning of the wind due to the relatively larger drag.

Are the ramps comparable to the ECD?

The rise time of the ramp-like fluctuations is generally much higher than that of the ECD. But the range is large, e.g. at Høvsøre the rise time ranges over two orders of magnitude (from 9–952 s). The rise time of the extreme direction events is on the order of a minute or more. Although these extreme direction events generally have a longer rise time than the defined ECD, they could readily be considered for load simulation purposes. The reason is that a wind turbine reacts much slower to changes in wind direction than to changes in wind speed. The yaw speed of a wind turbine is typically less than $0.5^\circ/\mathrm{s}$, which means that yawing 90° takes more than 3 minutes. Hence, during one of the extreme direction events, a wind turbine is continuously exposed to yaw misalignment, while the wind speed keeps increasing.

We observe ramp events that either have an amplitude, or rise time, or direction change on the same order of magnitude as the ECD. However, no single event is comparable to the ECD on all three variables at once. In order to predict an extreme event considering all three variables simultaneously, one would need a multivariate distribution model including the parameter distributions. That way it would be possible to model the probability of different positions in the three-parameter space and extrapolate to desired return periods.

7 Conclusions

The combination of the wavelet transform and the fitting of an idealized ramp function is a new and efficient way to characterize extreme wind speed ramps. The characterization provides variables that are relevant for wind energy, particularly for wind turbine load simulations, probabilistic design, and wind turbine safety standards.

We use measurements from three measurement sites in different terrain to calculate statistics of the amplitudes, direction change and rise time of extreme ramp-like fluctuations, and also compare the estimated variables with the ECD load case of the IEC standard. Here we find:

- The amplitudes of these coherent structures do not exceed the amplitude of the ECD (using ten, three, and one year of data, respectively).
- The amplitudes show no clear wind seed dependence at Høvsøre and Østerild, but at Ryningsnäs the amplitudes increase with increasing wind speed.
- The direction change may exceed that of the ECD, but for those events the rise time is a minute or more.

Future related work includes further analysis of ramp events. In particular, using a multivariate distribution model based on the marginal distributions of the ramp variables to estimate ramp events with a 50-year return period.

Data availability. The data is in an SQL database at DTU that is not publicly accessible.

Appendix A

The Figure in this appendix is equivalent to Figure 8, but shows the estimated variables as function of the speed u_b preceding the ramp.

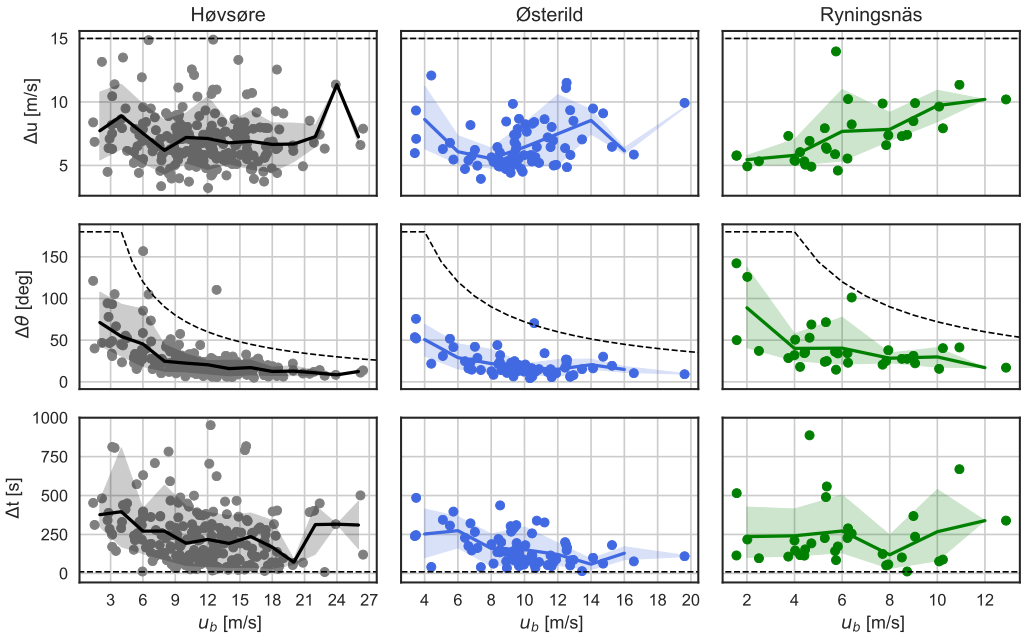

Figure A1. The detected amplitudes (Δu), direction changes ($\Delta\theta$) and rise times (Δt) as function of speed preceding the ramp (u_b) at the different sites: Høvsøre (grey), Østerild (blue) and Ryningsnäs (green). The plots share the primary axis (abcissa) per column and they share the secondary axis (ordinate) per row. The black dashed lines show the ECD values.

Note the IEC direction change prescription looks more reasonable when using u_b. This is because u_b is lower than the the average of u_b and u_a and the events get shifted to the left by using u_b when compared with Figure 8. This difference is greatest for the large amplitude events.

Author contributions. ÁH provided the detection method, performed the data analysis, and made the figures. MK provided guidance and comments. ÁH prepared the manuscript with contributions from MK.

Competing interests. The authors declares that they have no conflict of interest.

Acknowledgements. This work is part of ÁH's PhD under supervision of MK funded by DTU Wind Energy.

References

Arnqvist, J., Segalini, A., Dellwik, E., and Bergström, H.: Wind Statistics from a Forested Landscape, Boundary-Layer Meteorology, 156, 53–71, https://doi.org/10.1007/s10546-015-0016-x, 2015.

Bak, C., Zahle, F., Bitsche, R., Kim, T., Yde, A., Henriksen, L. C., Natarajan, A., and Hansen, M.: Description of the DTU 10 MW Reference Wind Turbine, Tech. rep., DTU Wind Energy, 2013.

Barthlott, C., Drobinski, P., Fesquet, C., Dubos, T., and Pietras, C.: Long-term study of coherent structures in the atmospheric surface layer, Boundary-Layer Meteorology, 125, 1–24, https://doi.org/10.1007/s10546-007-9190-9, 2007.

Belušić, D. and Mahrt, L.: Is geometry more universal than physics in atmospheric boundary layer flow?, Journal of Geophysical Research Atmospheres, 117, 1–10, https://doi.org/10.1029/2011JD016987, 2012.

Bierbooms, W.: Investigation of spatial gusts with extreme rise time on the extreme loads of pitch-regulated wind turbines, Wind Energy, 8, 17–34, https://doi.org/10.1002/we.139, http://doi.wiley.com/10.1002/we.139, 2005.

Bos, R., Bierbooms, W., and van Bussel, G.: Towards spatially constrained gust models, Journal of Physics: Conference Series, 524, 012 107, https://doi.org/10.1088/1742-6596/524/1/012107, http://stacks.iop.org/1742-6596/524/i=1/a=012107?key=crossref.1857b48508b1b08fee6bd9abe7dd0501, 2014.

Drobinski, P., Brown, R. A., Flamant, P. H., and Pelon, J.: Evidence of organized large eddies by ground-based Doppler lidar, sonic anemometer and sodar, Boundary-Layer Meteorology, 88, 343–361, https://doi.org/10.1023/A:1001167212584, 1998.

Dunyak, J., Gilliam, X., Peterson, R., and Smith, D.: Coherent gust detection by wavelet transform, Journal of Wind Engineering and Industrial Aerodynamics, 77-78, 467–478, https://doi.org/10.1016/S0167-6105(98)00165-2, 1998.

Farge, M.: Wavelet Transforms And Their Applications To Turbulence, Annual Review of Fluid Mechanics, 24, 395–457, https://doi.org/10.1146/annurev.fluid.24.1.395, http://fluid.annualreviews.org/cgi/doi/10.1146/annurev.fluid.24.1.395, 1992.

Fesquet, C., Drobinski, P., Barthlott, C., and Dubos, T.: Impact of terrain heterogeneity on near-surface turbulence structure, Atmospheric Research, 94, 254–269, https://doi.org/10.1016/j.atmosres.2009.06.003, http://dx.doi.org/10.1016/j.atmosres.2009.06.003, 2009.

Finnigan, J.: Turbulence in Plant Canopies, Annual Review of Fluid Mechanics, 32, 519–571, https://doi.org/10.1146/annurev.fluid.32.1.519, http://www.annualreviews.org/doi/10.1146/annurev.fluid.32.1.519, 2000.

Foster, R. C., Vianey, F., Drobinski, P., and Carlotti, P.: Near-surface coherent structures and the vertical momentum flux in a large-eddy simulation of the neutrally-stratified boundary layer, Boundary-Layer Meteorology, 120, 229–255, https://doi.org/10.1007/s10546-006-9054-8, 2006.

Gallego, C., Costa, A., Cuerva, Á., Landberg, L., Greaves, B., and Collins, J.: A wavelet-based approach for large wind power ramp characterisation, Wind Energy, 16, 257–278, https://doi.org/10.1002/we.550, 2013.

Hannesdóttir, Á., Kelly, M., and Dimitrov, N.: Extreme wind fluctuations: joint statistics, extreme turbulence, and impact on wind turbine loads, Wind Energy Science Discussions, 2018, 1–21, https://doi.org/10.5194/wes-2018-12, https://www.wind-energ-sci-discuss.net/wes-2018-12/, 2018.

Hansen, B. O., Courtney, M., Mortensen, N. G., Hansen, A. B. O., Courtney, M., and Mortensen, N. G.: Wind Resource Assessment – Østerild National Test Centre for Large Wind Turbines Wind Energy E Report 2014, Tech. Rep. August, DTU Wind Energy, Roskilde, Denmark, 2014.

Hansen, K. S. and Larsen, G. C.: Full scale experimental analysis of extreme coherent gust with wind direction changes (EOD), Journal of Physics: Conference Series, 75, https://doi.org/10.1088/1742-6596/75/1/012055, 2007.

IEC: IEC 61400-1 Ed3: Wind turbines - Part 1: Design requirements, standard, International Electrotechnical Commission, Geneva, Switzerland, 2005.

Jonkman, J., Butterfield, S., Musial, W., and Scott, G.: Definition of a 5-MW Reference Wind Turbine for Offshore System Development, Tech. Rep. February, National Renewable Energy Laboratory, Golden, Colorado, https://doi.org/10.2172/947422, http://www.osti.gov/servlets/purl/947422-nhrlni/, 2009.

Krusche, N. and de Oliveira, A.: Characterization of coherent structures in the atmospheric surface layer, Boundary Layer Meteorology, 110, 191–211, 2004.

Lee, G., Gommers, R., Wasilewski, F., Wohlfahrt, K., O'Leary, A., Nahrstaedt, H., and Contributors: PyWavelets - Wavelet Transforms in Python, https://github.com/PyWavelets/pywt, 2006–.

Liu, Y., Liang, X. S., and Weisberg, R. H.: Rectification of the bias in the wavelet power spectrum, Journal of Atmospheric and Oceanic Technology, 24, 2093–2102, https://doi.org/10.1175/2007JTECHO511.1, 2007.

Mahrt, L.: Eddy Asymmetry in the Sheared Heated Boundary Layer, Journal of the Atmospheric Sciences, 48, 472–492, https://doi.org/10.1175/1520-0469(1991)048<0472:EAITSH>2.0.CO;2, 1991.

Mahrt, L.: Common microfronts and other solitary events in the nocturnal boundary layer, Quarterly Journal of the Royal Meteorological Society, 136, 1712–1722, https://doi.org/10.1002/qj.694, 2010.

Peña, A., Floors, R., Sathe, A., Gryning, S. E., Wagner, R., Courtney, M. S., Larsén, X. G., Hahmann, A. N., and Hasager, C. B.: Ten Years of Boundary-Layer and Wind-Power Meteorology at Høvsøre, Denmark, Boundary-Layer Meteorology, 158, 1–26, https://doi.org/10.1007/s10546-015-0079-8, 2016.

Raupach, M., Finnigan, J., and Brunet, Y.: Coherent eddies and turbulence in vegetation canopies: the mixing-layer analogy., 78, 351–382, 1996.

Sogachev, A. and Kelly, M.: On Displacement Height, from Classical to Practical Formulation: Stress, Turbulent Transport and Vorticity Considerations, Boundary-Layer Meteorology, 158, 361–381, https://doi.org/10.1007/s10546-015-0093-x, 2016.

Steyn, D. G., Baldi, M., and Hoff, R. M.: The detection of mixed layer depth and entrainment zone thickness from lidar backscatter profiles, Journal of Atmospheric and Oceanic Technology, 16, 953–959, https://doi.org/10.1175/1520-0426(1999)016<0953:TDOMLD>2.0.CO;2, 1999.

Stork, C. H., Butterfield, C. P., Holley, W., Madsen, P. H., and Jensen, P. H.: Wind conditions for wind turbine design proposals for revision of the IEC 1400-1 standard, Journal of Wind Engineering and Industrial Aerodynamics, 74-76, 443–454, https://doi.org/10.1016/S0167-6105(98)00040-3, 1998.

Vincent, C. L., Hahmann, A. N., and Kelly, M.: Idealized Mesoscale Model Simulations of Open Cellular Convection Over the Sea, Boundary-Layer Meteorology, 142, 103–121, https://doi.org/10.1007/s10546-011-9664-7, 2012.

Young, G. S., Kristovich, D. A. R., Hjelmfelt, M. R., and Foster, R. C.: Rolls, Streets, Waves, and More: A Review of Quasi-Two-Dimensional Structures in the Atmospheric Boundary Layer, Bulletin of the American Meteorological Society, 83, 997–1001, https://doi.org/10.1175/1520-0477(2002)083<0997:RSWAMA>2.3.CO;2, 2002.

CHAPTER 5
Extreme coherent gusts with direction change

To investigate the impact of the extreme wind speed ramps on wind turbine loads, a subset of the events from chapter 4 is chosen. This subset is from the measurement site Høvsøre including only events that are close to rated wind speed. These events are used to construct a coherent gust model providing a joint description of gust variables with a 50-year return period.

This paper is written in collaboration with Albert Urbán who developed a yaw controller for HAWC2 and David Verelst who performed HAWC2 simulations.

The paper is a draft and has not yet been submitted.

Extreme coherent gusts with direction change - observations, yaw control and wind turbine loads

Ásta Hannesdóttir, Albert M. Urbán, and David R. Verelst
DTU Wind Energy Dept., Technical University of Denmark, Roskilde, Denmark
Correspondence: astah@dtu.dk

Abstract. Observations of large coherent fluctuations from a decade of measurements are used to define a coherent gust model with direction change. The gust model provides the joint description of the gust rise time, amplitude and directional changes with a 50-year return period. In conjunction with the elaborate gust model, a yaw controller is presented in this study to investigate the load implications of the joint gust variables. These loads are compared with the design load case of the extreme coherent gust with direction change (ECD) from the IEC 61400-1 Ed.3 wind turbine safety standard. Within the framework of the gust model we find the return period of the ECD to be approximately 15,000 years. From the simulations we find that for gusts with a relatively long rise time the blade root flapwise bending moment, for example, can be reduced by the considered yaw controller. From the extreme load comparison of the IEC ECD and the modeled gusts we see that the load values are within 11% of each other. The only exception is for the tower top yawing moment, where maximum load for the modeled gusts is 22% lower than the IEC gust.

The tower loading is evaluated in terms of the resultant bending moment at the tower base, and for which a nearly linear relationship is observed as function of gust acceleration.

1 Introduction

In the process of designing a wind turbine, designers have to consider a balance between cost and structural safety. Wind turbine safety standards like the IEC 61400-1 Ed.3 (IEC, 2005) exist to aid designers ensuring quality, reliability and safety of the wind turbine. The IEC standard prescribes extreme external wind conditions which the wind turbine must be able to withstand during the design lifetime, which is typically of 20 years. The extreme conditions are prescribed in a set of models used for specific design load cases (DLC's).

The present study addresses the extreme coherent gust with direction change (ECD) which is used for DLC 1.4 for ultimate load analysis. For certain turbines this load case could drive the ultimate loading of, for example, the blade root flapwise bending moment (Beardsell et al., 2016). The ECD model is originally presented in Stork et al. (1998) and was later validated against measurements and found to give reasonable results in Hansen and Larsen (2007). As pointed out by the authors of Hansen and Larsen (2007), these experiments are based on turbulent fluctuations, where the peak values in the measurements are due to gusts with a limited spatial extent (Larsen et al., 2003). Such gusts are not coherent across the rotor diameter of multi-megawatt wind turbines, like e.g. the DTU 10 MW wind turbine (Bak et al., 2013) that we consider in this study.

In a previous study (Hannesdóttir and Kelly, 2018), observations of coherent ramp-like wind speed fluctuations are detected and characterized. The coherent fluctuations are characterized with rise time, amplitude and direction change. The observed coherent gust are further compared with the ECD due to similarities, but show a considerable variability in the characterized variables. Generally, the rise time of the observed coherent gusts is much higher than that of the ECD, on average around 200 s. However, the rise time distribution has a large range. The observed direction change may exceed the one of the ECD, but then the corresponding rise time is considerably longer.

The aim of this paper is to investigate how these observed coherent gusts impact wind turbine loads and how they compare to the DLC 1.4 load case of the IEC standard. This will be achieved through tree steps:

1. Extrapolate the observed gust variables to a 50-year return period. As the gust variables form a three dimensional space, the extrapolation is done through the first order reliability method (IFORM) with the Nataf distribution model.
2. Develop a yaw controller to incorporate in the load simulations, as the observed gust may have a relatively long rise time, and a real wind turbine could start to yaw under such wind conditions.
3. We choose potentially critical points on the 3D gust variable surface for load simulations. The load simulations are performed using the aeroelastic software HAWC2 (Larsen and Hansen, 2015).

Yaw controllers have been investigated before in connection with energy capture optimization (Bossanyi et al., 2013), but to the author's knowledge not for investigating extreme loads in conjunction with an aeroelastic code.

2 The IEC extreme coherent gust with direction change

The amplitude of the extreme coherent gust with direction change (ECD) is $V_{\mathrm{cg}} = 15\,\mathrm{m/s}$ and is independent of the 10-minute mean hub height wind speed V_{hub}. The direction change of the ECD is a function of V_{hub} and given by

$$\theta_{cg} = \begin{cases} 180^\circ, & \text{if } V_{\mathrm{hub}} \leq 4\,\mathrm{m/s}, \\ 720^\circ\,\mathrm{m/s}/V_{\mathrm{hub}}, & \text{if } 4\,\mathrm{m/s} < V_{\mathrm{hub}} < V_{\mathrm{ref}}, \end{cases} \tag{1}$$

where V_{ref} is the 10-minute mean reference wind speed. The wind speed increase and direction change are assumed to occur simultaneously and are modeled as functions of time,

$$V(z,t) = \begin{cases} V(z), & \text{if } t < 0 \\ V(z) + 0.5V_{\mathrm{cg}}(1-\cos(\pi t/T)), & \text{if } 0 \leq t \leq T \\ V(z) + V_{\mathrm{cg}}, & \text{if } t > T \end{cases} \tag{2}$$

$$\theta_{\mathrm{cg}}(t) = \begin{cases} 0^\circ, & \text{if } t < 0 \\ \pm 0.5\theta_{\mathrm{cg}}(1-\cos(\pi t/T)), & \text{if } 0 \leq t \leq T \\ \pm\theta_{\mathrm{cg}}, & \text{if } t > T \end{cases} \tag{3}$$

where $T = 10\,s$ is the rise time. The ECD design load case is simulated at three different wind speeds, V_{ref} and $V_{\text{ref}} \pm 2$ m/s according to the IEC standard. In this study we only simulate the ECD at 10 m/s.

3 Observations of coherent gusts

In the present study we consider wind speed fluctuations that may be assumed to be coherent across the rotor of any multi-megawatt wind turbine. Such large coherent fluctuations are detected and characterized in a previous study (Hannesdóttir and Kelly, 2018), where a detailed description of the detection and characterization method may be found. The coherent gusts are detected from a 10.25 year measurement period in Høvsøre, located in Jutland, Denmark. It is argued that these gusts may originate from a broad variety of phenomena, but share the trait of ramp-like increase in wind speed that gives rise to extreme 10-minute variance.

The events are characterized by rise time (Δt), direction change ($\Delta\theta$) and amplitude ($\Delta u = u_a - u_b$), where u_b is the wind speed before the rise, and u_a is the wind speed after the rise. The events are observed at wind speeds ranging from $u_b = 1.4$ m/s to $u_b = 26.4$ m/s. In order to model the gusts, we choose a subset of events with the following selection criteria: $u_b < V_{\text{rated}}$ and $u_a > V_{\text{rated}}$. In other words, the wind speed is below rated wind speed before the gust and reaches above rated wind speed after the gust. This choice of subset is made as high loads are expected to be observed around rated wind speed (Hannesdóttir et al., 2018). A total of 90 events fulfill the selection criteria, and are used in the present study.

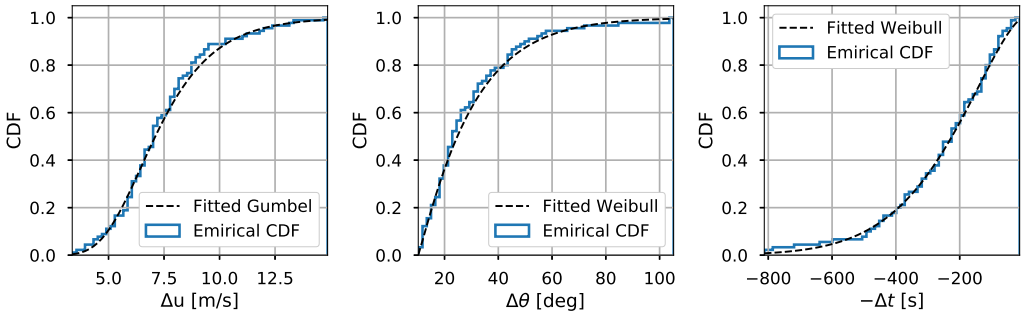

Figure 1. The marginal fitted and empirical cumulative distributions of: gust amplitude (left), gust direction change (middle) and negative gust rise time (right).

Figure 1 shows the cumulative distribution (CDF) of each coherent gust variable Δu, $\Delta\theta$ and Δt with fitted distributions. The distribution parameters are all found with maximum likelihood estimation. The gust amplitude Δu is assumed to follow a Gumbel distribution, where the estimated location and scale parameters are $\alpha = 6.45$ m/s and $\beta = 1.79$ m/s. The direction change $\Delta\theta$ is assumed to follow a three-parameter Weibull distribution with estimated parameters: $k = 1.09$ (shape parameter), $\gamma = 10.19°$ (location parameter) and $A = 20.42°$ (scale parameter). The rise time is assumed to follow the reversed two-parameter Weibull distribution, were the estimated parameter are: $k = 1.51$ and $A = 285.76$ s. Note that we change the sign

of the rise time when fitting the reversed Weibull distribution. This is done to ensure that the short rise times are defined as extreme values.

4 IFORM with the Nataf distribution model

The inverse first order reliability method (IFORM) was first developed by Winterstein et al. (1993) to predict extreme environmental conditions for offshore engineering. From the joint description of environmental variables, the method provides environmental contours corresponding to desired return periods. In wind engineering, IFORM is commonly used to predict the 50-year return period of the joint description of 10-minute mean wind speed and turbulence levels (e.g. Fitzwater et al., 2003; Sang Moon et al., 2014; Dimitrov et al., 2017).

In the current study, we use IFORM to predict the 50-year return period surface of the joint description of the gust variables, Δu, $\Delta\theta$ and Δt. Here the joint probability distribution of the variables is given by the Nataf distribution model, which is defined by Liu and Der Kiureghian (1986). Under Nataf transformation (Nataf, 1962), the considered variables are mapped from original space into correlated standard normal space, where the joint description of the variables is defined by a Gaussian copula. Unlike the Rosenblatt transformation (Rosenblatt, 1952), which is exact, the Nataf transformation is an approximate. In order to perform the Rosenblatt transformation, the complete joint cumulative distribution of the variables is needed, which is not available for the current analysis. However, to perform the Nataf transformation it is enough to know the marginal distributions and the correlation matrix of the variables.

The Nataf transformation of a random vector $\mathbf{X} = X_1, ..., X_n$ to standard normal space is performed by

$$Z_i = \Phi^{-1}(F_{x_i}(X_i)), \qquad i = 1, ..., n \tag{4}$$

where Φ^{-1} is the inverse standard CDF and $F_{x_i}(x_i)$ is the marginal CDF of X_i. The standard normal vector $\mathbf{Z} = Z_1, ..., Z_n$ has a correlation matrix $\boldsymbol{\rho}_0$.

4.1 Constructing the environmental surface

The first step in constructing the environmental surface of coherent gust variables is to calculate the probability level associated with the 50-year return period, T_{50}. The 50-year probability level has to be adjusted with the probability of observing a coherent gust P_{cg} during a 10-minute period in the measurement period. There are 90 selected coherent gusts found from 10-minute samples spanning a 10.25 year period, therefore the 50-year probability level becomes

$$P_{50} = \frac{1}{T_{50} \cdot P_{cg}} = \frac{1}{50 \cdot 365 \cdot 24 \cdot 6 \cdot 90/(10.25 \cdot 365 \cdot 24 \cdot 6)} = \frac{1}{50 \cdot 90/10.25} = 0.0023 \tag{5}$$

The next step is to find the associated 'reliability index', which has its name from the traditional first order reliability method (Ditlevsen and Madsen, 1996),

$$\beta = \Phi^{-1}(1 - P_{50}) = 2.84, \tag{6}$$

ij=	ρ_{ij}	$E(\rho_{ij})$	ρ_{0ij}
$\Delta u\ \Delta\theta$	0.494	1.074	0.530
$\Delta u\ \Delta t$	-0.281	1.106	-0.310
$\Delta\theta\ \Delta t$	-0.274	1.067	-0.292

Table 1. The estimated correlation coefficients and the evaluated empirical expressions for E.

which defines the radius of a sphere in standard normal space

$$\beta = \sqrt{u_1^2 + u_1^2 + u_3^2} \tag{7}$$

where u_1, u_2 and u_3 are spherical coordinates of the vector $|\mathbf{U}| = \beta$. The spherical coordinates may be generated by

$$u_1 = \beta \cos(\theta)\sin(\phi) \tag{8}$$

$$u_2 = \beta \sin(\theta)\sin(\phi) \tag{9}$$

$$u_3 = \beta \cos(\phi) \tag{10}$$

where $\theta = [0, 2\pi]$ and $\phi = [0, \pi]$.

Before performing the Nataf transformation, the correlation coefficients of $\boldsymbol{\rho}_0$ have to be determined. As shown in Liu and Der Kiureghian (1986), the correlation coefficients in standard normal space can be estimated from the correlation coefficients ρ_{ij} in real space (Δu, $\Delta\theta$ and Δt), through the following expression:

$$\rho_{0ij} = E\,\rho_{ij} \tag{11}$$

where $E \geq 1$, and is a function of the correlation coefficient ρ_{ij} and the corresponding marginal distributions. Empirical expression for E are provided in Liu and Der Kiureghian (1986) for 10 different distribution functions, where the Weibull distribution and the Gumbel distribution are both among them. We can therefore use these empirical expressions to estimate E (see Table 1). The correlation matrix $\boldsymbol{\rho}$ is calculated for the variables Δu, $\Delta\theta$ and Δt, and equation 11 is used to estimate the correlation coefficients of $\boldsymbol{\rho}_0$ (see Table 1).

We can now determine $\boldsymbol{\rho}_0$ as a lower-triangular matrix $\mathbf{L}_0$ by applying Cholesky decomposition. The last step in constructing the environmental surface of coherent gust variables, is to apply the inverse Nataf transformation. This is done in two steps. First to transform $\mathbf{U}$ to the correlated standard normal space,

$$\mathbf{Z} = \mathbf{L}_0 \cdot \mathbf{U} \tag{12}$$

and finally the variables of the surface are found by

$$\Delta u = F_{\Delta u}^{-1}(\Phi(Z_1)) \tag{13}$$

$$\Delta\theta = F_{\Delta\theta}^{-1}(\Phi(Z_2)) \tag{14}$$

$$\Delta t = F_{\Delta t}^{-1}(\Phi(Z_3)). \tag{15}$$

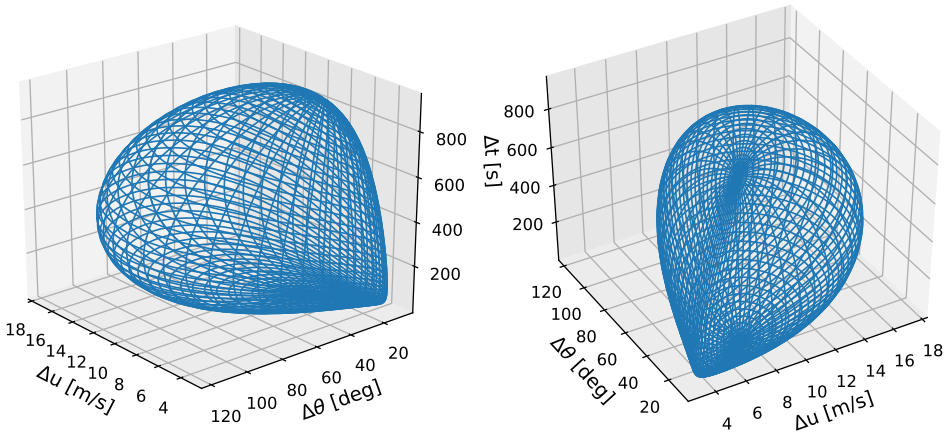

Figure 2. The 50-year return period surface of Δu, $\Delta\theta$ and Δt, seen from two different angles.

Figure 2 shows the surface of coherent gust variables with a 50-year return period. The maximum direction change ($\Delta\theta = 117.5°$) and maximum amplitude ($\Delta u = 17.3\,\text{m/s}$) are found on the surface at rise time of approximately 400 s. The surface is shown as Δu - $\Delta\theta$ contours for specific rise times in Figure 3. It may be seen that extreme direction change and amplitude decrease with decreasing rise time. The pink curve shows the Δu - $\Delta\theta$ contour where the rise time matches the rise time of the ECD $\Delta t = 10\,\text{s}$. However, on that curve we find that the maximum $\Delta u = 8.3\,\text{m/s}$ and the maximum $\Delta\theta = 35.3°$. The grey stars show the maximum Δu, the maximum $\Delta\theta$, and a point centered between the maxima on each rise time curve. These points are chosen for wind turbine load simulations.

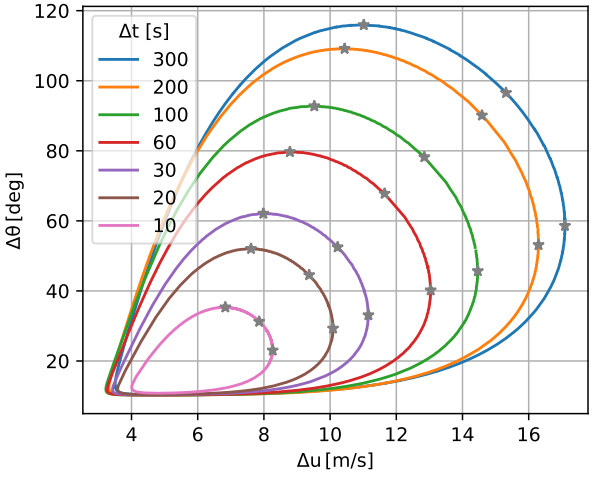

Figure 3. The 50-year return period surface, sliced at different rise times. The grey stars show the points chosen for load simulations.

4.2 The return period of the ECD

We see that the gust variables on the 10 s rise time contour in Figure 3 have a significantly lower amplitude and direction change than the ECD, which has $\Delta u = 15$ m/s and $\Delta\theta = 72^\circ$ (when simulated at 10 m/s). One could then ask: What is the required return period of the ECD gust parameters when considered within this framework? Or in other words, what return period do we have to use in order to make a point on the surface match the ECD values? The answer to that question may be found by doing the reversed operation of constructing the environmental surface:

$$\mathbf{Z}_{\text{ECD}} = \begin{cases} \Phi^{-1}(F_{\Delta u}(15)) \\ \Phi^{-1}(F_{\Delta\theta}(72)) \\ \Phi^{-1}(F_{\Delta t}(-10)) \end{cases} \tag{16}$$

Followed by the step

$$\mathbf{U}_{\text{ECD}} = \mathbf{L}_0^{-1} \cdot \mathbf{Z}_{\text{ECD}}, \tag{17}$$

The reliability index may be found by $\beta_{\text{ECD}} = |\mathbf{U}_{\text{ECD}}|$ and the associated probability by $P_{\text{ECD}} = 1 - \Phi(\beta_{\text{ECD}})$. Finally the return period is found

$$T_{\text{ECD}} = \frac{1}{P_{\text{ECD}} \cdot 90/10.25\,\text{years}} = 15208\,\text{years} \tag{18}$$

A return period of 15208 years is two orders of magnitude larger than the usual 50-year return period used in wind turbine design. The reason for this large return period is that according to our distributions and correlations between the coherent gust variables, there is a very low probability that a coherent gust with a rise time of 10 seconds has such a large amplitude and direction change as the ECD. Another reason for this large return period is that the ECD is originally based on point measurements of turbulent fluctuations, as mentioned in the introduction. These fluctuations generally have short time scales and high peak values, but are not necessarily coherent.

5 HAWC2

For this study HAWC2 (Larsen and Hansen, 2015) version 12.6 is used to calculate the aero-servo-elastic response of the DTU10MW (Bak et al., 2013). The DTU10MW is used together with the open source Basic DTU Wind Energy Controller (Hansen and Henriksen, 2013) (Hansen and Tibaldi, 2018). As reference load case the IEC DLC 1.4 ECD is used at 10 m/s. From a blade element momentum (BEM) modelling point of view, the considered load cases here are affected in particular by the dynamic inflow model (gust rise time and amplitude), and the induction correction due to skewed inflow (yaw misalignment). Both corrections, and other HAWC2 BEM modelling specifics, are discussed in appendix E.3 of the MexNext Phase 3 report (Boorsma et al., 2018). The modeled gusts described in section 4.1 are simulated at the specific points in the gust variable

space, shown in Figure 3. The simulations of the observed gusts are performed in the same way as the ECD, i.e. starting at 10 m/s with corresponding time varying functions as described in section 2. The rise time, amplitude and direction change is given the value of the chosen points on the curves.

6 Yaw controller

A yaw controller ensures that the wind turbine is aligned with the mean wind speed direction which is important for two reasons, (1) below rated the power extraction is higher if the wind turbine is aligned as shown in Kragh and Hansen (2015) and (2) the extreme loading is higher when it is operating with yaw errors.

The yaw controller needs information about the wind direction to determine if the turbine is operating in yaw misalignment. Conventional wind turbines uses a wind vane mounted in the nacelle to calculate the yaw error. The positioning of the measurement presents uncertainty on the wind direction since the equipment is installed behind the rotor where the flow is disturbed. Different sensors has been investigated to improved the wind direction estimation as spinner-mounted, continuous-wave light and ranging lidars in Kragh et al. (2010).

Once the error is measured, different strategies are used to determine whether the wind turbine yaws for a given misalignment. The yaw controller presented in Kragh et al. (2013) uses a periodic correction of the yaw angle where the misalignment error is low pass filtered and integrated. Once the integrated error exceeds the defined threshold, the wind turbine starts yawing. The basic yaw controller designed for this study is based on two moving averages with a different averaging window. The first moving average is used to determine the initialization of the yawing sequence while the second one commands it to stop. The yaw controller is used together with the Basic DTU Wind Energy Controller Hansen and Henriksen (2013) for witch the source code can be found at Hansen and Tibaldi (2018).

The basic yaw controller uses as inputs: (1) hub wind speed, (2) time average window for yaw start, (3) time average window for yaw stop, (4) yaw error threshold and (5) current time. The instantaneous yaw error is given by the angle composed by the longitudinal and perpendicular direction of the wind speed at hub position, input 1. Then, the instantaneous yaw error is included in the start time average window with a specified window length, input 2. If the yaw error average is higher than the defined threshold, input 4, the yaw controller sends an order to the yaw servo model to start yawing at highest yaw rate. The yaw servo will yaw until the stop moving average yaw error defined in input 3 is below half of the initial yaw error threshold. An example of the two time moving averages is shown in figure 4.

In figure 4 the nacelle is initially offset 30 degrees with respect to the mean wind direction. The stop moving average (red line), with a time windows of 10 seconds, responds much faster to a change in yawing error compared to the start moving average (blue line) with a window length of 120 seconds. The threshold is set to 5 degrees and it can be observed that the wind turbine starts yawing once the error, in the starting moving average, exceeds the threshold, 4 right blue marker. Finally, the wind turbine stops once the short window time moving average is below half of the initial threshold,4 right red marker, where the yaw error is 0.2 degrees.

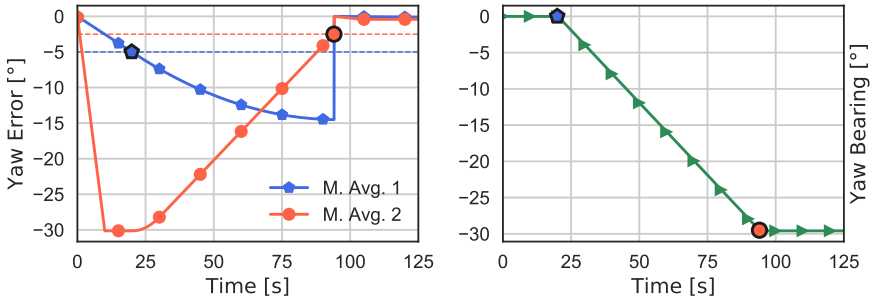

Figure 4. *Left*: Yaw error as function of time for; start moving average 1 (blue), and stop moving average 2 (red). The blue dashed line shows the start threshold and the red dashed line shows the stop threshold. *Right*: Yaw bearing angle as function of time.

Although a more elaborate study regarding yaw control should be considered, the simple long/short time averaging approach is chosen here in order not to trigger a yaw action to early (hence 120 second averaging window for the start trigger), while avoiding to overshoot after a zero yaw error has been reached (using the 10 second averaging window for the stop trigger).

The yaw mechanism is modelled as a second order dynamical system with a frequency of 5 Hz and a damping ratio of 0.7. There is no limit on the maximum and minimum yaw angle allowing a full rotation of the system. It is possible to constrain the response of the second order model in velocity and acceleration. A typical yaw sweep sequence, yawing 360 degrees, last around 15 minutes which leads to a yaw rate approximately of 0.4 degrees / second.

The proposed basic yaw controller can be replaced with a classic Proportional Integral Derivative (PID) where the objective signal is the yaw angle and not the rate of change or velocity of the yaw mechanism.

7 Simulation results and discussion

This section presents time-series of the ECD and a modeled gust with a relatively long rise time. We discuss the implication of using a yaw controller and give an overview of all the simulated gusts with different rise times, amplitudes, and direction changes.

7.1 Time series with the ECD

The time-series of the IEC gust is shown in Figure 5. The simulation represented with a black color does not include yaw controller while the blue one does. The absolute maxima of the simulation is represented by a marker of the same color in Figure 5.

From the loads side, the time-series shows the blade root flap-wise moment (BR_{flap}), shaft torsion ($S_{torsion}$), tower top yaw moment (TT_{yaw}) and tower bottom resultant bending moment defined as $TB_{res} = \sqrt{TB_{FA}^2 + TB_{SS}^2}$, where TB_{FA} is

the tower base fore-aft moment and TB_{SS} is the tower base side-side moment. Presenting the resultant load provides a clear comparison of the total magnitude of the tower bottom loading between the yawing and non-yawing cases. The wind speed magnitude and its direction and the nacelle yaw angle is also presented.

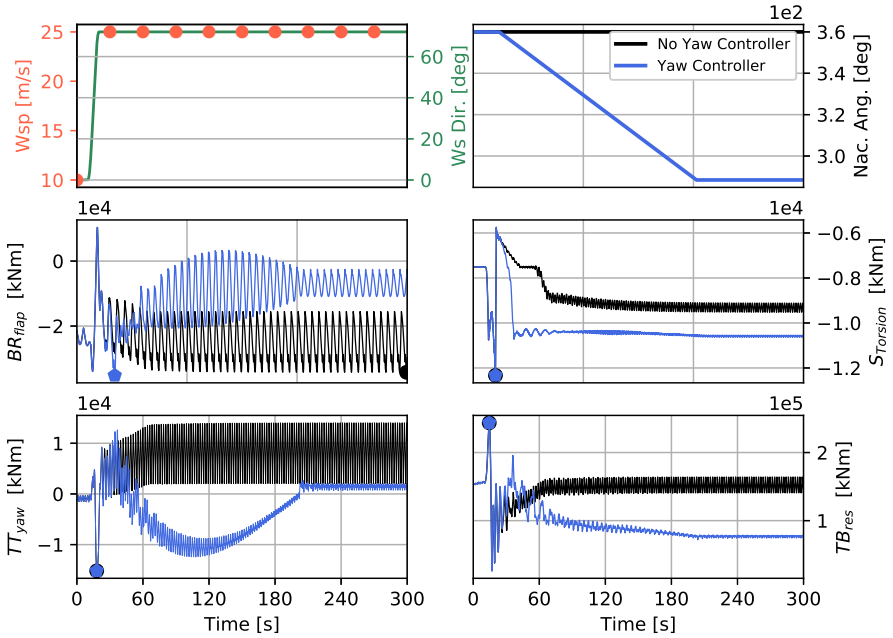

Figure 5. IEC gust with (blue) and without (black) controller. From left to right and top to bottom the plots show : (1) wind speed and wind direction time-series and comparison of (2) nacelle yaw angle, (3) blade root flapwise moment, (4) shaft torsion, (5) tower top yawing moment and (5) tower bottom resultant moment

The effect of the yaw controller is noticed in the upper right panel of Figure 5 where the nacelle angle is shown. We can observe that the absolute maxima of the shaft torsion, tower top yaw moment and tower resultant load channels are found at the same instant regardless the yaw controller. The peak loads are found during the fast rise time of the gust and before the yaw controller acts. However, a slight difference is found in the blade flap-wise moment where the use of yaw controller decrease the maximum compared to the standard case.

7.2 Modeled gust with a long rise time

An example of a modeled coherent gust, simulated with a rise time of 200 s, an amplitude of 14.6 m/s and a absolute direction change of 90° is shown in Figure 6.

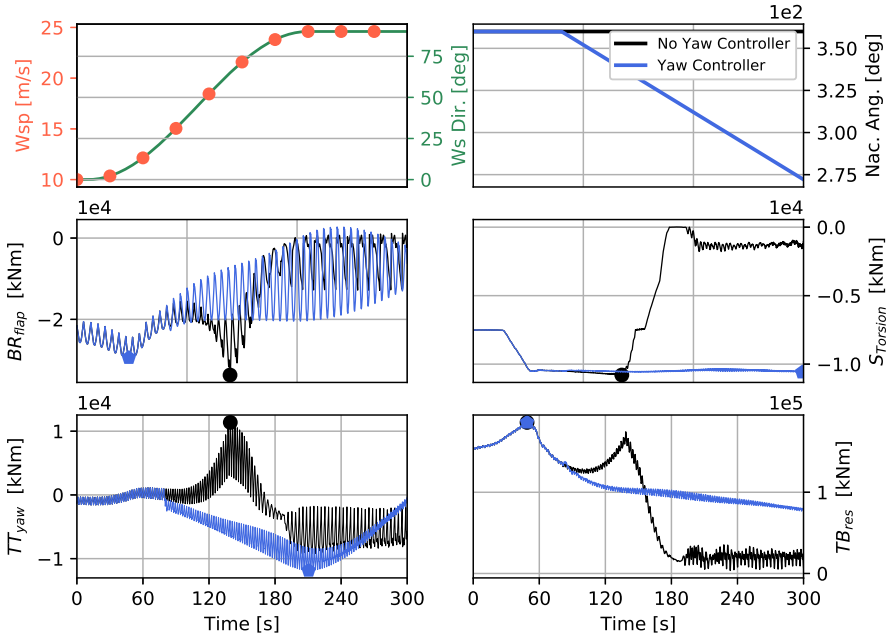

Figure 6. Gust of 14.6 m/s amplitude, 200s rise time and 90 ° direction change with (blue) and without (black) controller. From left to right and top to bottom the plots show: (1) wind speed and wind direction, (2) nacelle yaw angle, (3) blade root flap-wise moment, (4) shaft torsion, (5) tower top yawing moment and (5) tower bottom resultant moment

The effect of the yaw controller is noticeable in the blade root flap-wise and in the tower top yaw moment in Figure 6. When using the yaw controller, the shaft torsion and yaw moment remain, in absolute value, the same and the blade flap-wise moment is reduced by 14%. The tower bottom resultant moment peak is found before the yaw controller acts, thus, having the same values for both cases. It can also be seen from the torque signal that the shaft load is higher, thus, producing more power due to the significantly reduced yaw error.

7.3 Simulation overview

For the 22 considered ECD gusts at $10m/s$ (21 ECD gusts defined with the current model and 1 from the IEC standard) the absolute maximum of the tower bottom resultant (TB_{res}) and the blade root flap-wise moment are presented in Figures 7 and 8 respectively. The left figure presents the absolute maximum on the secondary axis (ordinate), and the gust acceleration on the primary axis (abscissa) . The gust acceleration is defined as the ratio between the gust amplitude and rise time $(\Delta u/\Delta t)$.

Note that in Figure 7, on the left panel, a nearly linear increase may be found between the TB_{res} and the gust acceleration. Further, both with and without yaw control results in the same absolute maximum of TB_{res}. This can also be observed in Figures 5 and 6. Since the TB_{res} consistently occurs during the initial phase of the gust before the yaw controller reacts, and therefore becomes independent of the current implementation and tuning of the yaw controller. The IEC ECD case may be noticed with a gust acceleration of $1.5\,\mathrm{m/s^2}$ and a directional change of 72° in the left panel.

The right panel in Figure 7 indicates the yaw error at which the absolute maximum of TB_{res} occurs. It is included here to place the results in the context of the accuracy of the BEM based aerodynamic model in HAWC2. At large yaw errors ($> 20 - 30$ °) BEM's accuracy needs to be considered carefully. A detailed comparison between wind tunnel measurements and various aerodynamic and aeroelastic codes at different inflow conditions is presented in the Mexnext phase 3 report (regarding skewed inflow specifically in chapter 10 and appendix B) (Boorsma et al., 2018). Within the scope of this investigation it is dully noted that for large yaw errors there is a higher uncertainty on aerodynamic loading of the wind turbine model.

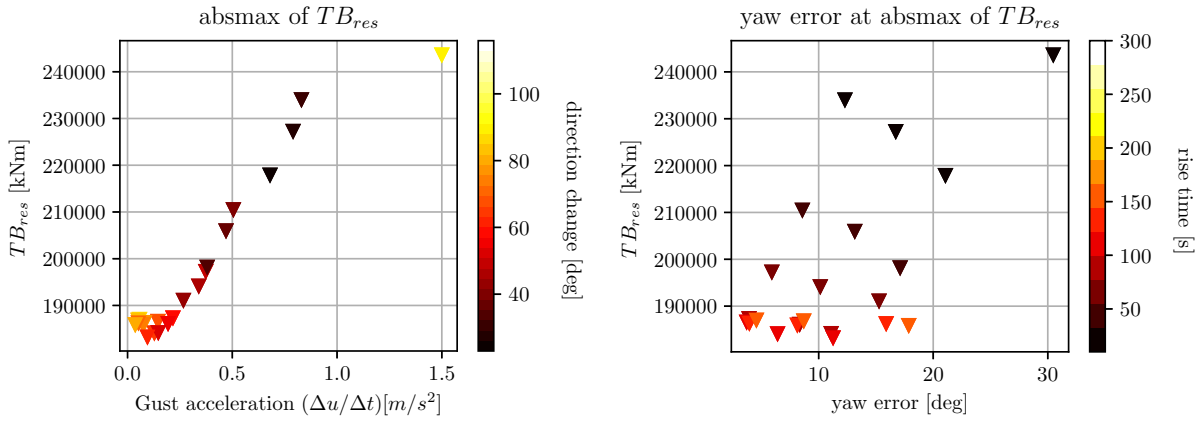

Figure 7. Simulations without yaw control (empty triangles), and with yaw control (fully coloured triangles). *Left panel*: Tower base resultant moment as function of gust acceleration. The colors of the markers refer to the gust directional change, in degrees. *Right panel*: Tower base resultant moment as function of yaw error. The marker colors refer to the gust rise time in seconds. The IEC ECD case may be noticed furthest to the right in both panels.

In Figure 8 the absolute maximum of the blade root flapwise bending moment BR_{flap} is considered in the left panel. For this load channel there is a clear dependency on the presence of a yaw controller. Gusts with a long rise time endure higher loads without yaw control. When looking at the yaw error at the time at which the absolute maximum of BR_{flap} occurs, it is noted that for cases without yaw control the yaw error is, not surprisingly, much larger compared to with yaw control. Yaw errors in excess of 60° are observed. Consequently, a higher degree of uncertainty has to be considered when looking at loads presented under these operating conditions.

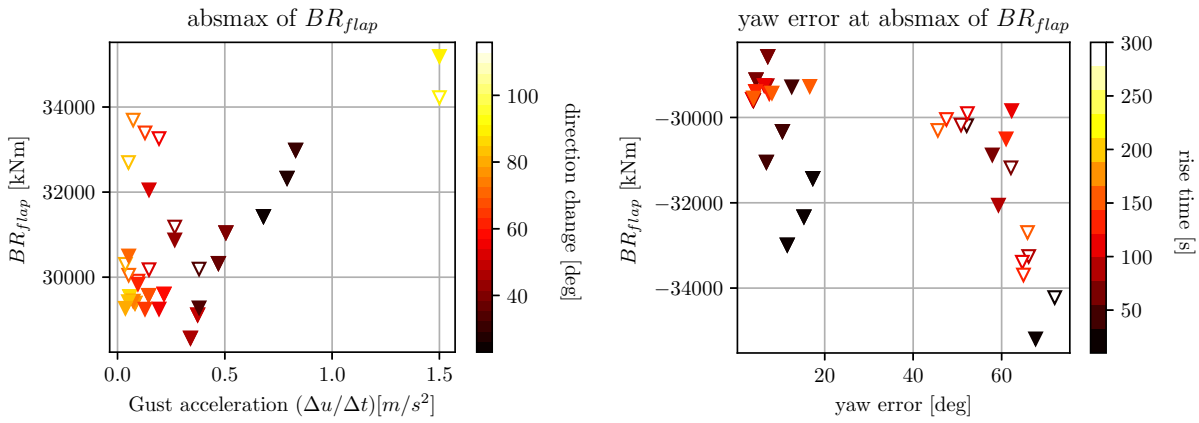

Figure 8. Simulations without yaw control (empty triangles), and with yaw control (fully coloured triangles). *Left panel*: Blade root flap-wise loads as function of gust acceleration. The colors of the markers refer to the gust directional change, in degrees. *Right panel*: Blade root flap-wise moments as function of yaw error. The marker colors refer to the gust rise time in seconds. The IEC ECD case may be noticed furthest to the right in both panels.

In Figure 9 it is indicated where in the gust variable space the absolute maximum of a selection of load channels occurs, both with and without yaw control. Note they are indicated on the 50-year return period gust curves, similar to Figure 3. The ECD gust from the IEC standard is not included here. The corresponding values of these maximum loads are given in Table 2 and Table 3, without and with yaw control respectively. Here the reference values of the IEC gust case are included. Based on this it is noted that the IEC gust case is a conservative load case compared to the alternative ECD gusts definitions. For all included load channels, except for the blade root edge-wise bending moment BR_{edge}, the IEC gust case results in higher loads though not significantly. The highest difference is observed for the tower top yawing moment, where the IEC gust case is approximately 22% higher compared to the other gusts.

Amplitude [m/s]	Rise time [s]	Direction change [°]	channel	absmax	IEC absmax	% diff wrt IEC
8.3	10	23.0	TB_{res} [kNm]	234034.6	243629.6	-3.9%
11.6	60	67.8	TT_{yaw} [kNm]	11798.0	15188.3	-22.3%
14.6	200	90.1	BR_{flap} [kNm]	33692.8	34222.2	-1.5%
17.1	300	58.6	BR_{edge} [kNm]	11503.0	10904.2	5.5%
8.3	10	23.0	$BR_{torsion}$ [kNm]	289.1	331.2	-12.7%
8.0	30	62.1	$S_{torsion}$ [kNm]	10967.4	12331.9	-11.1%
8.3	10	23.0	TT_{acc} [m/s^2]	0.364557	0.374818	-2.7%

Table 2. Absolute maxima of a selection of load channels without yaw control for gusts starting at 10 m/s. The IEC absmax column refers to the IEC DLC1.4 gust case with a rise time of 10 seconds, amplitude of 15 m/s and a directional change of 72°.

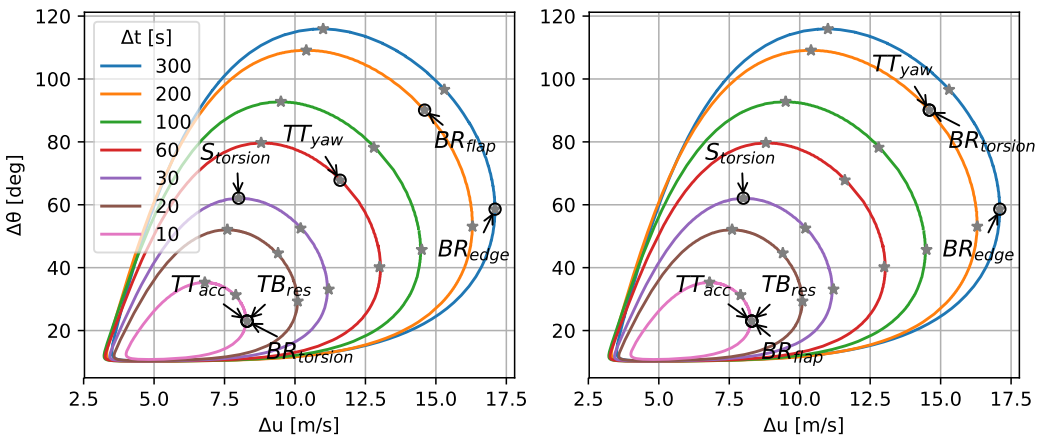

Figure 9. The 50-year return period gust curves with locations of selected maximum loads indicated with black circles. *Left panel*: Without yaw control. *Right panel*: With yaw control.

Amplitude [m/s]	Rise time [s]	Direction change [°]	channel	absmax	IEC absmax	% diff wrt IEC
8.3	10	23.0	TB_{res} [kNm]	234044.8	243630.5	-3.9 %
14.6	200	90.1	TT_{yaw} [kNm]	11863.2	15182.5	-21.9 %
8.3	10	23.0	BR_{flap} [kNm]	32988.2	35189.7	-6.3 %
17.1	300	58.6	BR_{edge} [kNm]	11503.1	10904.4	5.5 %
14.6	200	90.1	$BR_{torsion}$ [kNm]	300.7	331.1	-9.2 %
8.0	30	62.1	$S_{torsion}$ [kNm]	10967.4	12331.3	-11.1 %
8.3	10	23.0	TT_{acc} [m/s^2]	0.364941	0.373671	-2.3 %

Table 3. Absolute maxima of a selection of load channels with yaw control for gusts starting at 10 m/s. The IEC absmax column refers to the IEC DLC1.4 gust case with a rise time of 10 seconds, amplitude of 15 m/s and a directional change of 72°.

According the modeled ECD gusts in this study, the IEC definition of the ECD does not seem to be overly conservative in terms of the load response for the DTU10MW. However, with a return period of 15,000 years for the IEC ECD gust, its physical relevance could be challenged. Alternatively, a selection of different gusts with varying rise time and amplitude, representing a physical ECD, might be considered instead. Although not addressed in the current study, the validity of BEM remains a challenge for the ECD as a load case due to the large yaw errors.

8 Conclusions

In this work observations of coherent gusts are used to obtain an environmental surface with a 50-year return period with the Nataf distribution model. The surface is in three dimensional gust variable space of; rise time, amplitude and direction

change. There is a large variability within the modeled gust variables, where the direction change and amplitude may exceed the ECD values, though in these cases with a considerably longer rise time. For modeled gusts with 10 s rise time, the maximum amplitude is 8.3 m/s and the maximum direction change is 35.3°

The modeled gust variable surface can match the values of the IEC ECD gust parameters by using a return period of approximately 15,000 years.

We choose 21 points on the surface to simulate for wind turbine response, where the simulations are performed with-, and without a yaw controller that is specially developed in this study.

The effect of the yaw controller is seen for the modeled gusts with a relatively long rise time where especially the blade root flap-wise bending moment BR_{flap} is significantly reduced when the wind turbine yaws. However, for the short rise time gusts the maximum loads are generally the same with- or without the yaw controller, as the maximum loads are observed before the initiation of the yaw controller.

From the comparison of the modeled gusts and the IEC ECD, we find that even though the modeled gusts are not as severe in terms of gust variables, the difference in observed extreme loads is generally low. From the considered load component channels the largest difference is seen for the tower top yaw moment, which is 22% lower for the modeled gust compared with the IEC gust.

The maximum loads for the TT_{acc}, TB_{res} and BR_{flap} are observed for the modeled gusts with the highest gust acceleration. The difference between these maximum loads and the IEC gust loads is approximately 3%, 4% and 6% respectively.

A nearly linear relation between gust acceleration and the maximum resultant tower base bending moment is observed. This relationship is independent of yaw control since it is driven by the initial response of the turbine to the ECD gust, and which is before the yaw controller can act.

Author contributions. ÁH made the gust analysis and gust model. AU developed the yaw controller. DV performed HAWC2 load simulations. ÁH wrote Sects. 1, 2, 3, 4 and 8. AU wrote Sects. 6, 7.1 and 7.2. DV wrote Sects. 5 and 7.3. All authors commented on the paper.

Competing interests. The authors declares that they have no conflict of interest.

Acknowledgements. ÁH would like to thank Mark Kelly for comments and discussion around the coherent gust distribution model.

References

Bak, C., Zahle, F., Bitsche, R., Kim, T., Yde, A., Henriksen, L. C., Natarajan, A., and Hansen, M.: Description of the DTU 10 MW Reference Wind Turbine, Tech. rep., DTU Wind Energy, 2013.

Beardsell, A., Collier, W., and Han, T.: Effect of linear and non-linear blade modelling techniques on simulated fatigue and extreme loads using Bladed, Journal of Physics: Conference Series, 753, https://doi.org/10.1088/1742-6596/753/4/042002, 2016.

Boorsma, K., Schepers, J., Gomez-Iradi, S., Herraez, I., Lutz, T., Weihing, P., Oggiano, L., Pirrung, G., Madsen, H., Shen, W., Rahimi, H., and Schaffarczyk, P.: Final Report of IEA Wind Task 29 Mexnext (Phase 3), Tech. Rep. ECN-E–18-003, ECN, http://www.ecn.nl/publications/ECN-E--18-003, 2018.

Bossanyi, E., DelouvriÃ©, T., Lindahl, S., and Garrad Hassan, G. L.: Long-term simulations for optimising yaw control and start-stop Strategies, European Wind Energy Conference and Exhibition, Ewec 2013, 2, 1199–1208, 2013.

Dimitrov, N., Natarajan, A., and Mann, J.: Effects of normal and extreme turbulence spectral parameters on wind turbine loads, Renewable Energy, 101, 1180–1193, https://doi.org/10.1016/j.renene.2016.10.001, http://dx.doi.org/10.1016/j.renene.2016.10.001, 2017.

Ditlevsen, O. and Madsen, H.: Structural Reliability Methods, John Wiley & Sons, Inc., 1996.

Fitzwater, L. M., Allin Cornell, C., and Veers, P. S.: Using environmental contours to predict extreme events on wind turbines, Proceedings of the 2003 ASME Wind Energy Symposium, Paper No. 2003-865. Reno, Nevada, USA., pp. 244–258, https://doi.org/10.1115/WIND2003-865, 2003.

Hannesdóttir, Á. and Kelly, M.: Detection and characterization of extreme wind speed ramps, manuscript submitted for publication, 2018.

Hannesdóttir, Á., Kelly, M., and Dimitrov, N.: Extreme wind fluctuations: joint statistics, extreme turbulence, and impact on wind turbine loads, Wind Energy Science Discussions, 2018, 1–21, https://doi.org/10.5194/wes-2018-12, https://www.wind-energ-sci-discuss.net/wes-2018-12/, 2018.

Hansen, K. S. and Larsen, G. C.: Full scale experimental analysis of extreme coherent gust with wind direction changes (EOD), Journal of Physics: Conference Series, 75, https://doi.org/10.1088/1742-6596/75/1/012055, 2007.

Hansen, M. and Tibaldi, C.: Basic DTU Wind Energy Controller source code, https://github.com/DTUWindEnergy/BasicDTUController, original-date: 2015-12-02T08:27:49Z, 2018.

Hansen, M. H. and Henriksen, L. C.: Basic DTU wind energy controller, 2013.

IEC: IEC 61400-1 Ed3: Wind turbines - Part 1: Design requirements, standard, International Electrotechnical Commission, Geneva, Switzerland, 2005.

Kragh, K., Hansen, M., and Mikkelsen, T.: Improving Yaw Alignment Using Spinner Based LIDAR, in: Proceedings of the 49th AIAA Aerospace Sciences Meeting Including the New Horizons Forum and Aerospace Exposition 2011, 2010.

Kragh, K., Fleming, P., and Scholbrock, A.: Increased Power Capture by Rotor Speed–Dependent Yaw Control of Wind Turbines, Journal of Solar Energy Engineering, 135, https://doi.org/10.1115/1.4023971, 2013.

Kragh, K. A. and Hansen, M. H.: Potential of power gain with improved yaw alignment, Wind Energy, 18, 979–989, 2015.

Larsen, G. C., Bierbooms, W., and Hansen, K. S.: Mean Gust Shapes, Risø-R-1133(EN), 1133, 2003.

Larsen, T. J. and Hansen, A. M.: How 2 HAWC2, the user's manual, Tech. rep., DTU Wind Energy, 2015.

Liu, P. L. and Der Kiureghian, A.: Multivariate distribution models with prescribed marginals and covariances, Probabilistic Engineering Mechanics, 1, 105–112, https://doi.org/10.1016/0266-8920(86)90033-0, 1986.

Nataf, A.: Determination des Distributions dont les Marges sont Donnees, Comptes Rendus de l'Academie des Sciences, 225, 42–43, 1962.

Rosenblatt, M.: Remarks on a Multivariate Transformation, The Annals of Mathematical Statistics, 23, 470–472, https://doi.org/10.1214/aoms/1177729394, 1952.

Sang Moon, J., Sahasakkul, W., Soni, M., and Manuel, L.: On the Use of Site Data to Define Extreme Turbulence Conditions for Wind Turbine Design, Journal of Solar Energy Engineering, 136, 044 506, https://doi.org/10.1115/1.4028721, 2014.

Stork, C. H., Butterfield, C. P., Holley, W., Madsen, P. H., and Jensen, P. H.: Wind conditions for wind turbine design proposals for revision of the IEC 1400-1 standard, Journal of Wind Engineering and Industrial Aerodynamics, 74-76, 443–454, https://doi.org/10.1016/S0167-6105(98)00040-3, 1998.

Winterstein, S. R., Ude, T. C., Cornell, C. a., Bjerager, P., and Haver, S.: Environmental Parameters for Extreme Response: Inverse Form with Omission Factors, Icossar-93, pp. 9–13, 1993.

CHAPTER 6

Conclusion

In this thesis wind speed fluctuation of different scales were investigated. Measurements of gusts, turbulence and large coherent fluctuations were characterized and simulated.

Chapter 2:
In this study a rotational shaping filter is defined in a simple way from the spectral model of turbulent fluctuation observed from a rotating frame of reference (Connell, 1982; Kristensen and Frandsen, 1982). The spectral model is based on the von Kármán spectrum, where the turbulence is assumed to be homogeneous, isotropic and stationary. Wind speed measurements from Høvsøre are analyzed to investigate the effect of rotational sampling on gust statistics. The measurements are band-pass filtered with a second-order Butterworth filter to ensure stationarity in the measurements and filter out the smallest scale fluctuations. The rotational shaping filter is applied to the band-passed filtered measurements.

The effect of rotational sampling on gust statistics is quantified. First, the number of detected gusts increases roughly by a factor of two. Second, the duration of the rotationally sampled gusts is significantly reduced. Third, the amplitudes of the short duration gusts are increased by the effect of rotational sampling. However, due to the limited spatial extent of fast fluctuations these short duration gusts are not likely to cause extreme loading on a wind turbine blade, although they might contribute to its fatigue loading.

Chapter 3:
In this paper the main objective is to investigate how extreme variance events influence wind turbine response and how it compares with DLC 1.3 of the IEC 61400-1 standard. We use 10 years of measurements from the measurement site Høvsøre, focusing on the western (off-shore) sectors. The selected extreme events are measurements of the 10-minute standard deviation of horizontal wind speed that exceed the values prescribed by the ETM model and include a sudden velocity jump, which is the main cause of the high observed variance. The events are large coherent structures, observed simultaneously at two different masts with a 400 m separation.

The 50-year return period of turbulence levels is estimated with the inverse first-order reliability method. The turbulence levels are estimated for raw, linearly-detrended and high-pass filtered measurements. The estimated 50-year return period contour of the linearly detrended data exceed the the 50-year return period contour of normal turbulence, corresponding to the ETM class C. By high-pass filtering the measurements with a cut-off frequency of 1/300 Hz, the turbulence level is reduced significantly as is the estimated 50-year return period of turbulence, to the extent that the turbulence level is lower than that of IEC ETM class C.

The events are simulated by constraining synthesized turbulence fields, where the

measured time series are incorporated in turbulence boxes for load simulations. This is done to make a realistic representation of the events, including the short term ramps and the coherent flow in the lateral direction that is observed in the comparison of measurements between the two masts in Høvsøre. The constraints force the turbulent flow of the simulations to be non-stationary and non-homogeneous.

Load calculations of the simulated extreme events are made in HAWC2 for the DTU 10 MW reference wind turbine and compared to load calculations with stationary homogeneous turbulence according to DLC 1.3. Compared with the DLC 1.3 of the IEC standard, the extreme loads are on average lower for the extreme variance events in the coastal/offshore climate and heights considered. For 10-minute mean wind speeds of 8–16 m/s, the events typically begin below rated wind speed and increase beyond, leading to high thrust on the rotor; such events lead to high extreme tower-base fore-aft loads which can exceed the DLC 1.3 prescription of the IEC standard.

Chapter 4:
The main focus of this paper is to detect and characterize coherent wind speed fluctuations. The combination of the wavelet transform and the fitting of an idealized ramp function is a new and efficient way to characterize extreme wind speed ramps. The characterization provides parameters that are relevant for wind energy, particularly for wind turbine load simulations, probabilistic design, and wind turbine safety standards.

We use measurements from three measurement sites (Høvsøre, Østerild and Ryningsnäs)in different terrain to calculate statistics of the amplitudes, direction change and rise time of extreme ramp-like fluctuations. A comparison is made of the estimated variables with the ECD load case of the IEC standard. From the comparison we find that the amplitudes of these coherent structures do not exceed the amplitude of the ECD.

The amplitudes show no clear wind seed dependence at Høvsøre and Østerild, but at Ryningsnäs the amplitudes increase with increasing wind speed. The direction change may exceed that of the ECD, but for those events the rise time is a minute or more.

Chapter 5:

Here the first order reliability method is used with the Nataf distribution model to construct a three-dimensional environmental surface of coherent gust variables, with a 50 year return period. The coherent gusts used are a subset of those described in Chapter 4. They consist of observed wind-speed ramps from Høvsøre where the wind speed goes from below rated wind speed to above, during the ramp.

We choose 21 points on the environmental surface that may potentially give high loads, and simulate these using HAWC2. A yaw controller, specially developed for this study, is implemented for more realistic loads. A comparison with the IEC ECD shows that overall the loads are of the same magnitude as the simulated gusts, except for the tower top yaw moment, which is 22% lower for the modeled gust compared with the IEC gust.

Within the framework of large coherent gust model, it is found that the return period of IEC gusts is approximately 15.000 years.

The effect of the yaw controller is most prominent for gusts with a long rise time. Here loads are significantly reduced when the wind turbine yaws. For the short rise time

gusts the maximum loads are unaffected by the inclusion of the yaw controller, as the maximum loads are observed before the initiation of the yaw controller.

6.1 Future work

Future related work includes investigation and characterization of extreme short-term shear associated with wind speed ramps. Load simulations of the events may then be compared to the extreme wind shear load case of the IEC standard.

The newly developed yaw controller in HAWC2 opens up for interesting possibilities for load analysis. E.g characterization of wind direction change for fatigue load analysis, with focus on time scale of minutes that may be incorporated in turbulence simulations.

Bibliography

Abdallah, I., Natarajan, A., and Sørensen, J. D.: Influence of the control system on wind turbine loads during power production in extreme turbulence: Structural reliability, Renewable Energy, 87, 464–477, doi:10.1016/j.renene.2015.10.044, URL http://dx.doi.org/10.1016/j.renene.2015.10.044, 2016.

Bak, C., Zahle, F., Bitsche, R., Kim, T., Yde, A., Henriksen, L. C., Natarajan, A., and Hansen, M.: Description of the DTU 10 MW Reference Wind Turbine, Tech. rep., DTU Wind Energy, 2013.

Barthlott, C., Drobinski, P., Fesquet, C., Dubos, T., and Pietras, C.: Long-term study of coherent structures in the atmospheric surface layer, Boundary-Layer Meteorology, 125, 1–24, doi:10.1007/s10546-007-9190-9, 2007.

Beljaars, A. C. M.: The Influence of Sampling and Filtering on Measured Wind Gusts, Journal of Atmospheric and Oceanic Technology, 4, 613–626, doi:10.1175/1520-0426(1987)004<0613:TIOSAF>2.0.CO;2, 1987.

Belušić, D. and Mahrt, L.: Is geometry more universal than physics in atmospheric boundary layer flow?, Journal of Geophysical Research Atmospheres, 117, 1–10, doi:10.1029/2011JD016987, 2012.

Berg, J., Natarajan, A., Mann, J., and Patton, E. G.: Gaussian vs non-Gaussian turbulence: impact on wind turbine loads, Wind Energy, 19, 1975–1989, doi:10.1002/we.1963, 2016.

Bergström, H.: A statistical analysis of gust characteristics, Boundary-Layer Meteorology, 39, 153–173, 1987.

Bierbooms, W.: Investigation of spatial gusts with extreme rise time on the extreme loads of pitch-regulated wind turbines, Wind Energy, 8, 17–34, doi:10.1002/we.139, 2005.

Boettcher, F., Renner, C., Waldl, H. P., and Peinke, J.: On the statistics of wind gusts, Boundary-Layer Meteorology, 108, 163–173, doi:10.1023/A:1023009722736, 2003.

Bos, R., Bierbooms, W., and van Bussel, G.: Towards spatially constrained gust models, Journal of Physics: Conference Series, 524, 012 107, doi:10.1088/1742-6596/524/1/012107, URL http://stacks.iop.org/1742-6596/524/i=1/a=012107?key=crossref.1857b48508b1b08fee6bd9abe7dd0501, 2014.

Branlard, E.: Wind energy: On the statistics of gusts and their propagation through a wind farm, Tech. Rep. February, 2009.

Burlibaşa, A. and Ceangă, E.: Rotationally sampled spectrum approach for simulation of wind speed turbulence in large wind turbines, Applied Energy, 111, 624–635, doi:10.1016/j.apenergy.2013.05.002, 2013.

Butterworth, S.: On the Theory of Filter Amplifiers, Experimental Wireless and the Wireless Engineer, 7, 536–541, 1930.

Cartwright, D. E. and Longuet-Higgins, M. S.: The Statistical Distribution of the Maxima of a Random Function, Proceedings of the Royal Society A: Mathematical, Physical and Engineering Sciences, 237, 212–232, doi:10.1098/rspa.1956.0173, URL `http://rspa.royalsocietypublishing.org/cgi/doi/10.1098/rspa.1956.0173`, 1956.

Connell, J.: The spectrum of wind speed fluctuations encountered by a rotating blade of a wind energy conversion system, Solar Energy, 29, 363–375, doi:10.1016/0038-092X(82)90072-X, 1982.

Dimitrov, N., Natarajan, A., and Mann, J.: Effects of normal and extreme turbulence spectral parameters on wind turbine loads, Renewable Energy, 101, 1180–1193, doi:10.1016/j.renene.2016.10.001, 2017.

Doran, J. C. and Powell, D. C.: Gust structure in the neutral surface boundary layer, Journal of applied meteorology, 21, 14–17, doi:10.1175/1520-0450(1982)021<0014:GSITNS>2.0.CO;2, 1982.

Drobinski, P., Brown, R. A., Flamant, P. H., and Pelon, J.: Evidence of organized large eddies by ground-based Doppler lidar, sonic anemometer and sodar, Boundary-Layer Meteorology, 88, 343–361, doi:10.1023/A:1001167212584, 1998.

Fesquet, C., Drobinski, P., Barthlott, C., and Dubos, T.: Impact of terrain heterogeneity on near-surface turbulence structure, Atmospheric Research, 94, 254–269, doi:10.1016/j.atmosres.2009.06.003, URL `http://dx.doi.org/10.1016/j.atmosres.2009.06.003`, 2009.

Fitzwater, L. M., Allin Cornell, C., and Veers, P. S.: Using environmental contours to predict extreme events on wind turbines, Proceedings of the 2003 ASME Wind Energy Symposium, Paper No. 2003-865. Reno, Nevada, USA., pp. 244–258, doi:10.1115/WIND2003-865, 2003.

Foster, R. C., Vianey, F., Drobinski, P., and Carlotti, P.: Near-surface coherent structures and the vertical momentum flux in a large-eddy simulation of the neutrally-stratified boundary layer, Boundary-Layer Meteorology, 120, 229–255, doi:10.1007/s10546-006-9054-8, 2006.

Frandsen, S., Joørgensen, H. E., and Soørensen, J. D.: Relevant Criteria for Testing the Quality of Models for Turbulent Wind Speed Fluctuations, Journal of Solar Energy Engineering, 130, 031 016, doi:10.1115/1.2931511, 2008.

Hannesdóttir, Á. and Kelly, M.: Detection and characterization of extreme wind speed ramps, manuscript submitted for publication, 2018.

Hannesdóttir, Á., Kelly, M., and Dimitrov, N.: Extreme wind fluctuations: joint statistics, extreme turbulence, and impact on wind turbine loads, Wind Energy Science Discussions, 2018, 1–21, doi:10.5194/wes-2018-12, URL `https://www.wind-energ-sci-discuss.net/wes-2018-12/`, 2018.

Hansen, M.: Aerodynamics of Wind Turbines: second edition, Earthscan, 2 edn., 2008.

IEC: IEC 61400-1 Ed3: Wind turbines - Part 1: Design requirements, standard, International Electrotechnical Commission, Geneva, Switzerland, 2005.

IRENA: Renewable Power Generation Costs in 2017, Report, International Renewable Energy Agancy, Abu Dhabi, United Arab Emirates, 2017.

IRENA: Renewable Energy Statistics 2018, Report, International Renewable Energy Agancy, Abu Dhabi, United Arab Emirates, 2018.

Jonkman, J., Butterfield, S., Musial, W., and Scott, G.: Definition of a 5-MW Reference Wind Turbine for Offshore System Development, Tech. Rep. February, National Renewable Energy Laboratory, Golden, Colorado, doi:10.2172/947422, 2009.

Kaimal, J. C., Wyngaard, J. C., Izumi, Y., and Coté, O. R.: Spectral characteristics of surface-layer turbulence, Quarterly Journal of the Royal Meteorological Society, 98, 563–589, doi:10.1002/qj.49709841707, 1972.

Kárḿan, T. V.: Progress in the Statistical Theory of Turbulence, Proceedings of the National Academy of Sciences of the United States of America, 34, 530–539, 1948.

Kristensen, L. and Frandsen, S.: Model for power spectra of the blade of a wind turbine measured from the moving frame of reference, Journal of Wind Engineering and Industrial Aerodynamics, 10, 249–262, doi:10.1016/0167-6105(82)90067-8, 1982.

Kristensen, L., Casanova, M., Courtney, M. S., and Troen, I.: In search of a gust definition, Boundary-Layer Meteorology, 55, 91–107, doi:10.1007/BF00119328, URL `http://link.springer.com/10.1007/BF00119328`, 1991.

Larsen, G. C., Bierbooms, W., and Hansen, K. S.: Mean Gust Shapes, Risø-R-1133(EN), 1133, 2003.

Mahrt, L.: Eddy Asymmetry in the Sheared Heated Boundary Layer, Journal of the Atmospheric Sciences, 48, 472–492, doi:10.1175/1520-0469(1991)048<0472:EAITSH>2.0.CO;2, 1991.

Mahrt, L.: Common microfronts and other solitary events in the nocturnal boundary layer, Quarterly Journal of the Royal Meteorological Society, 136, 1712–1722, doi: 10.1002/qj.694, 2010.

Mann, J.: The Spatial Structure of Neutral Atmospheric Surface-Layer Turbulence, Journal of Fluid Mechanics, 273, 141–168, doi:10.1017/S0022112094001886, 1994.

Manwell, J. F., McGowan, J. G., and Rogers, A. L.: Wind Energy Explained, John Wiley & Sons, Ltd, Chichester, UK, 2 edn., doi:10.1002/9781119994367, 2009.

Peña, A., Floors, R., Sathe, A., Gryning, S. E., Wagner, R., Courtney, M. S., Larsén, X. G., Hahmann, A. N., and Hasager, C. B.: Ten Years of Boundary-Layer and Wind-Power Meteorology at Høvsøre, Denmark, Boundary-Layer Meteorology, 158, 1–26, doi:10.1007/s10546-015-0079-8, 2016.

Rosenbrock, H.: Vibration and stability problems in large wind turbines having hinged blades, Tech. Rep. C/T 113, ERA Technology Ltd., Surrey, England, 1955.

Sang Moon, J., Sahasakkul, W., Soni, M., and Manuel, L.: On the Use of Site Data to Define Extreme Turbulence Conditions for Wind Turbine Design, Journal of Solar Energy Engineering, 136, 044 506, doi:10.1115/1.4028721, 2014.

Saranyasoontorn, K. and Manuel, L.: Design Loads for Wind Turbines Using the Environmental Contour Method, Journal of Solar Energy Engineering, 128, 554, doi: 10.1115/1.2346700, 2006.

Sieros, G., Chaviaropoulos, P., Sørensen, J. D., Bulder, B. H., and Jamieson, P.: Upscaling wind turbines: theoretical and practical aspects and their impact on the cost of energy, Wind Energy, 15, 3–17, doi:10.1002/we.527, URL `http://doi.wiley.com/10.1002/we.527`, 2012.

Suomi, I., Vihma, T., Gryning, S. E., and Fortelius, C.: Wind-gust parametrizations at heights relevant for wind energy: A study based on mast observations, Quarterly Journal of the Royal Meteorological Society, 139, 1298–1310, doi:10.1002/qj.2039, 2013.

Young, G. S., Kristovich, D. A. R., Hjelmfelt, M. R., and Foster, R. C.: Rolls, Streets, Waves, and More: A Review of Quasi-Two-Dimensional Structures in the Atmospheric Boundary Layer, Bulletin of the American Meteorological Society, 83, 997–1001, doi: 10.1175/1520-0477(2002)083<0997:RSWAMA>2.3.CO;2, 2002.

{2.7182818284}ϑωερτυθιοπσδφγηξκλ